Search for primary photons in the energy range from 10^{17} eV to 10^{18} eV at the Pierre Auger Observatory

Masterarbeit

zur Erlangung des akademischen Grades

Master of Science

(M.Sc.)

der Universität Siegen

Department Physik

vorgelegt von

Simon Franz Eickhoff

November 2018

Contents

1 Introduction

The sky and what is beyond is fascinating people since the beginning of mankind. Even with observations just made by the naked eye significant achievements in the field of astronomy were made including the spherical shape of the Earth or the disproof of the geocentrical model of the universe. The understanding of the relative movement of the stars and other sky objects was for example used by sailors to navigate over the ocean. With the invention of the first optical telescopes in the 17th century it was possible to look even deeper into the universe.
Exceeding the regime of visible light with wavelengths in the nm range, scientists in the 19th century invented methods to measure also waves with much lower (Radio) and much higher frequencies (X-ray and γ-rays). The spectral classification of stars made it possible to investigate the matter they are made of and the processes inside. With the discovery of cosmic rays in the early 20th century it was shown that not just photons but also massive charged particles reach the Earth's surface with energies up tp 10^{20} eV. Up to the 1950s it was not possible to accelerate particles to such high energies which made cosmic rays a powerful source to discover new grounds in the field of particle physics.
Even if the universe is studied now for thousands of years a lot of the basic questions could not yet be answered, for example the sources of cosmic rays as well as their acceleration mechanisms. This work will focus on the search for high energetic photons utilizing measurements of the Pierre Auger Observatory and may contribute to answer these questions.

1.1 History of Cosmic Ray Measurements

Over a century ago, in 1912, Victor Franz Hess discovered the existence of ionizing radiation coming from the sky. He performed multiple balloon flights up to an altitude of 5.3 km with equipment to measure the radiation. These balloon flights were motivated by former experiments measuring the natural radiation which was assumed to be originating solely within the first meter of the Earth's surface. Theodor Wulf tried to confirm that theory and measured the radiation on top of the Eiffel tower which should be significantly smaller than on the earths surface [2]. Even

Figure 1.1: A photograph of Victor Franz Hess in the gondola of a balloon in 1912 [1]

though his results confirmed a decrease in radiation with increasing altitude, the radiation was still significantly bigger than expected. In addition to that, Domenico Pacini observed that the radiation on the mediterranean sea is not suppressed which should be the case if the soil is the source of it [3]. Motivated by these observations Hess started his balloon flights in 1911. A photograph of him starting a balloon flight can be seen in Fig. 1.1. Within the first kilometer he measured a decreasing radiation confirming Wulfs observations. By getting to even higher altitudes, Hess discovered a rising occurrence of ionizing radiation. Fig. 1.2 shows the ionization Hess measured at different altitudes. The radiation increased up to two times of the intensity at ground level and he concluded the existence of an extraterrestrial component [4]. For this discovery Hess received the Nobel Prize in 1936 [5]. The observations Hess made were affirmed by measurements of Werner Kohlhörster. He also established the term “cosmic rays” [6].

After two decades of investigating the cosmic radiation, Pierre Auger discovered a phenomenon today known as extensive air showers (EAS) in 1939. These were before predicted by Homi Jehangir Bhabha and Walter Heitler in their theory of electromagnetic showers. They used relativistic quantum mechanics to state that a primary cosmic-ray electron produces a cascade of secondary electrons via pair production [8]. With this background Auger performed coincidence measurements

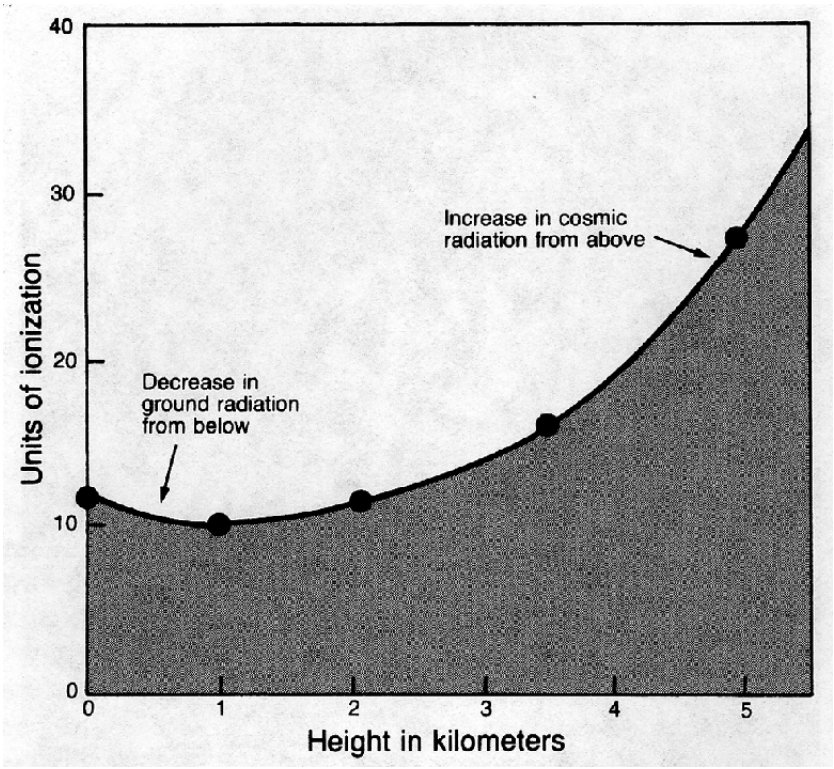

Figure 1.2: Results of Hess' measurements of the radiation at different altitudes. [7]

of cosmic rays. He found that cosmic rays arrive not singular but in large coincident bunches. He proved that the origin of the measured particles is not in outer space, in fact a single extraterrestrial particle induced a shower of secondary particles [9]. This new discovery led to the conclusion that the energy of the initial particles has to be much bigger than previously expected. Since it was not possible to achieve such high energies artificially on Earth, the investigation of cosmic rays led to a lot of major discoveries in particle physics. The positron was discovered in 1933 [10], the muon in 1937 [11] as well as the kaon in 1947 [12]. Today, astronomy and particle physics are closely connected in the field of astroparticle physics. In the 1950s first particle detectors were built to investigate new particles and the core question of astroparticle physics shifted towards the question of their sources, their composition and energy spectrum as well as their acceleration and propagation mechanisms.
Balloon-borne experiments were much improved over the years and were still performed until the early 2000s like Bess-PolarI and Bess-PolarII [13]. With rising technical know-how new ways to measure primary cosmic particles as well as the extensive air showers were established. Satellite mounted experiments like PAMELA [14] or AMS-02 [15] which is attached to the ISS are orbiting the Earth in order to detect the primary cosmic radiation with a focus on anti-matter. The High Energy Stereoscopic System (H.E.S.S.) located in Namibia is built to observe γ-rays with energies up to 100 TeV [16].

This work is based on the measurements of extensive air showers with the Pierre Auger Observatory (more in chapter 2) on the ground with the focus on detecting primary high energetic photons.

1.2 Cosmic Rays

The term "cosmic rays" initially was just used for charged particles, but also neutral particles are arriving from outer space like photons and neutrinos. Taking galactic and extragalactic sources into account the cosmic ray spectrum spans over 11 orders of magnitude. In Figure 1.3 the whole energy spectrum of all cosmic ray particles as measured by different experiments is shown. It is multiplied by a factor of $E^{2.6}$ to emphasize the features of the spectrum. It starts at about $10^{13}\,\mathrm{eV}$ with a flux of about $1000\,\mathrm{GeV}^{1.6}\,\mathrm{m}^{-2}\,\mathrm{sr}^{-2}\,\mathrm{s}^{-2}$ and then follows a broken power-law of the form

$$\frac{\mathrm{d}\Phi}{\mathrm{d}E} \propto E^{-\gamma}\,. \tag{1.1}$$

Before the energy spectrum reaches a cutoff at around 500 GeV the spectral index γ changes three times. At around 3 PeV it changes from 2.7 to 3.0, which is called the "knee". The "second knee" is at around 300 PeV. The spectral index changes from 3.0 to 3.2. The spectrum gets a bit flatter again with a change of γ from 3.2 to 2.7 at around 3 EeV, which is referred to as the "ankle". Air showers with energies up to the GeV range are influenced by the Earth's magnetic field and the sun activity. This leads to a cut off at the lowest energies since charged particles are deflected by the magnetic field and need a certain momentum to reach the Earth's atmosphere [17]. The cause for the features in the energy spectrum is not yet determined. The knee as well as the second knee are both believed to be caused by the incapability of galactic acceleration processes to produce higher energies. A common model to explain these features is referring to the diffusive shock acceleration of Supernova Remnants (SNR) [18]. Another possible model is based on the propagation of the particles through changing magnetic fields produced by rapidly spinning neutron stars in the center of the milky way. A third category of theories rely on physics beyond the Standard Model of Particle Physics. In these theories, new particles originating in for example Supersymmetry or Technicolor [19] produce high energetic cosmic rays when decaying.

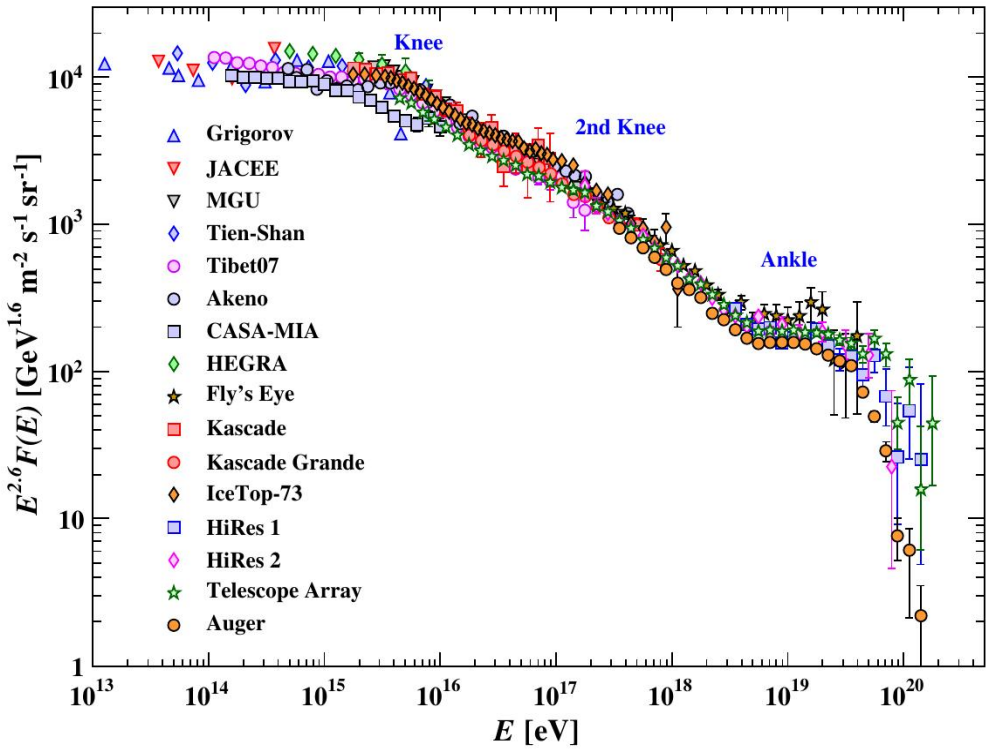

(a)

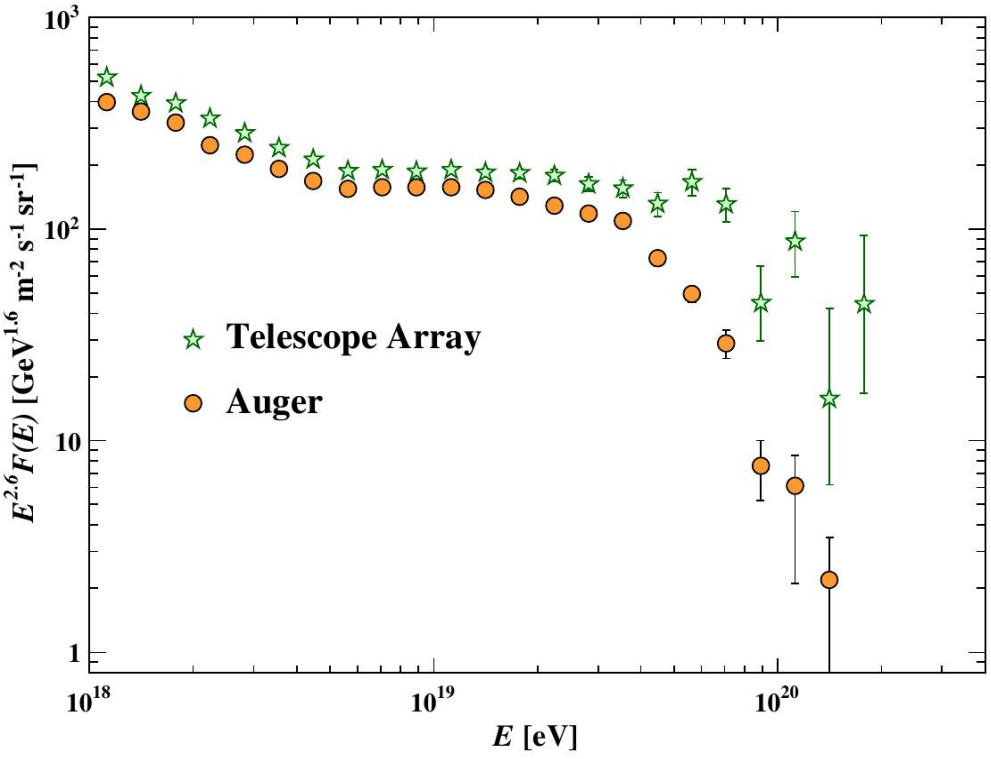

(b)

Figure 1.3: (a) The energy spectrum of all cosmic ray particles as measured by different experiments. It is multiplied by $E^{2.6}$ to emphasize the effects of the 'knee', the 'second knee' and the ankle. (b) The ultra high energy region of the spectrum, showing the cutoff measured by the Pierre Auger Observatory and The Telescope Array. [20]

While the particles with energies up to the 'ankle' are believed to originate in the milky way, the particles with higher energies are assumed to be of extragalactic origin [21]. The definite transition area from galactic to extragalactic cosmic rays although is not yet clear. A variety of different models which are based on different sources and acceleration mechanisms have been developed to explain the origin of ultra high energy cosmic rays (UHECR) above 1 EeV. One recent observation by the LIGO collaboration is the merging process of two black holes which could be a candidate for the source of UHECR [22]. At energies above 50 EeV the energy spectrum drops rapidly. Assuming these cosmic rays are of extragalactic origin this cutoff can be explained by the GZK effect after Greisen, Zatsepin and Kuz'min [23] [24]. In this model UHE cosmic protons with energies above 5×10^{19} eV interact with photons of the cosmic microwave background (CMB) forming a Delta resonance which then decays into one of these channels:

$$\begin{aligned} p + \gamma_{\mathrm{CMB}} &\rightarrow \Delta(1232)^{+} \rightarrow p + \pi^{0} \\ p + \gamma_{\mathrm{CMB}} &\rightarrow \Delta(1232)^{+} \rightarrow n + \pi^{+} \,. \end{aligned} \tag{1.2}$$

The resulting pions then again decay into photons or leptons respectively. This process leads to a significant loss in energy for protons traversing the universe. To measure a particle above 10^{20} eV, the origin has to be within the GZK-horizon of ~ 100 Mpc [25]. For nuclei the GZK threshold is higher than for protons, but other effects like the photo-disintegration with the CMB and the extragalactic background light has to be taken into account which again leads to flux suppression at highest energies.

1.3 Extensive Air Showers

When UHE particles reach the Earth's atmosphere they are most likely to interact with its components like N_2, O_2 and Ar, producing secondary particles. These particles again interact subsequently and a cascade of particles is released which can reach diameters of several kilometers. It is important to measure these extensive air showers since it is almost impossible to measure initial cosmic rays in the UHE range directly due to the drastically reduced flux. For example at the 'ankle' region the flux is already down to just one particle per square kilometer per year (see figure 1.3) and satellite-borne detectors are at best a few m^2 in measurement area [27]. An extensive air shower can be divided into different components as shown in figure 1.5. The hadronic component is developing directly after the first interaction of the primary particle with the atmospheric molecules and consists mainly of pions since they are the lightest hadrons and most frequently to be produced. In addition

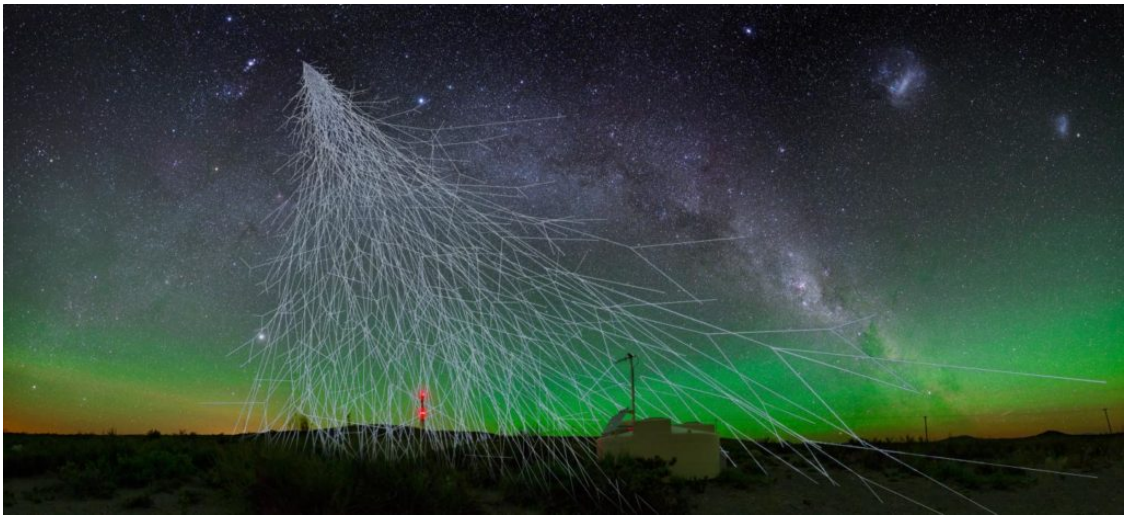

Figure 1.4: Artistic illustration of an extensive air shower over a detector of the Pierre Auger Observatory [26].

also kaons as well as protons and neutrons are part of the hadronic component. The hadrons interact further with the atmosphere and establish a hadronic cascade. The other two shower components are subsequently formed by the pions and kaons of the hadronic component. Neutral pions decay into two photons which form the electromagnetic part together with electrons resulting from muon decays, Compton scattering and pair production. The decay of charged hadrons into muons and neutrinos on the other hand feeds into the muonic component.

As the air shower develops in the atmosphere the individual particles lose energy with every interaction until they are more likely to be absorbed by the atmosphere than to interact again. The air shower starts to thin out. A Gaisser-Hillas function [29] of the form

$$N(X) = N_{\max} \left(\frac{X - X_0}{X_{\max} - \lambda} \right)^{\frac{X_{\max} - \lambda}{\lambda}} \exp\left(-\frac{X - X_0}{\lambda} \right) \tag{1.3}$$

is used to describe the average longitudinal development of an extensive air shower. The function depends on the atmospheric depth X which is commonly used instead of the altitude h and corresponds to the matter density traversed by the particle. It can be calculated as an integral over the atmospheric density $\rho(h)$:

$$X = \int_0^\infty \rho(h') \mathrm{d}h' \,. \tag{1.4}$$

Furthermore $N_{\max}$ denotes the number of particles at the shower maximum with the slant depth $X_{\max}$. X_0 is the slant depth of the first interaction point of the shower in the atmosphere and λ stands for the mean free path of each particle in the air shower. In Fig. 1.6a the longitudinal profile of an electromagnetic cascade

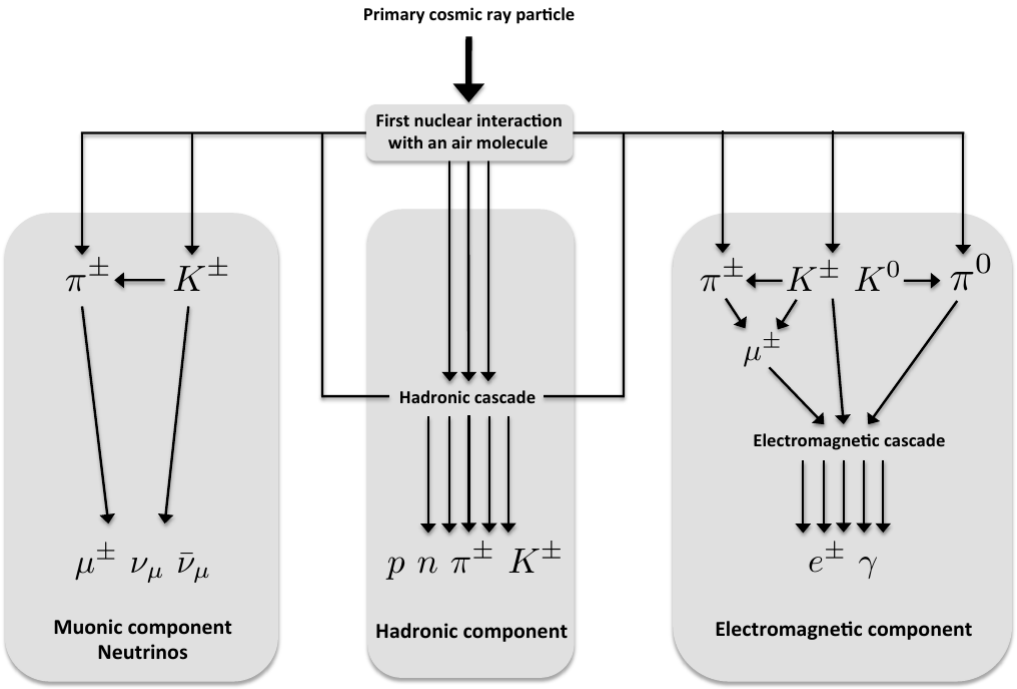

Figure 1.5: Schematic depiction of the particles and interactions taking part in an extensive air shower [28].

with different energies of the primary particle is shown. The value of $X_{\max}$ rises with increasing energy. The longitudinal development for the different components of an extensive air shower with a primary energy of $E_0 = 10^{15}\,\mathrm{eV}$ is shown in Fig. 1.6b. The muon component is relatively flat in contrast to the hadronic and electromagnetic component. The electromagnetic component has a much larger number of particles than the others.

A cosmic ray air shower can extend over a large area, the main energy contribution is contained around the shower axis. With the assumption of a symmetrical distribution of particles around the shower axis, the electron density ρ_e can be written as a function of the perpendicular distance r to the shower core:

$$\rho_e(r) = \frac{N_e}{2\pi r_M^2} \frac{\Gamma(4.5-s)}{\Gamma(s)\Gamma(4.5-2s)} \left(\frac{r}{r_M}\right)^{s-2} \left(1+\frac{r}{r_M}\right)^{s-4.5} . \tag{1.5}$$

This function was developed by Nishimura, Kamata and Greisen (NKG) [30] [31] and includes the Gamma function $\Gamma(x)$, the total number of electrons N_e, the Molière radius r_M which refers to the characteristic spread of electrons in a certain material (more in [32]) and the shower age s. The latter depends on the atmospheric depth X through the relation $s = \frac{3X}{X+2X_{\max}}$.

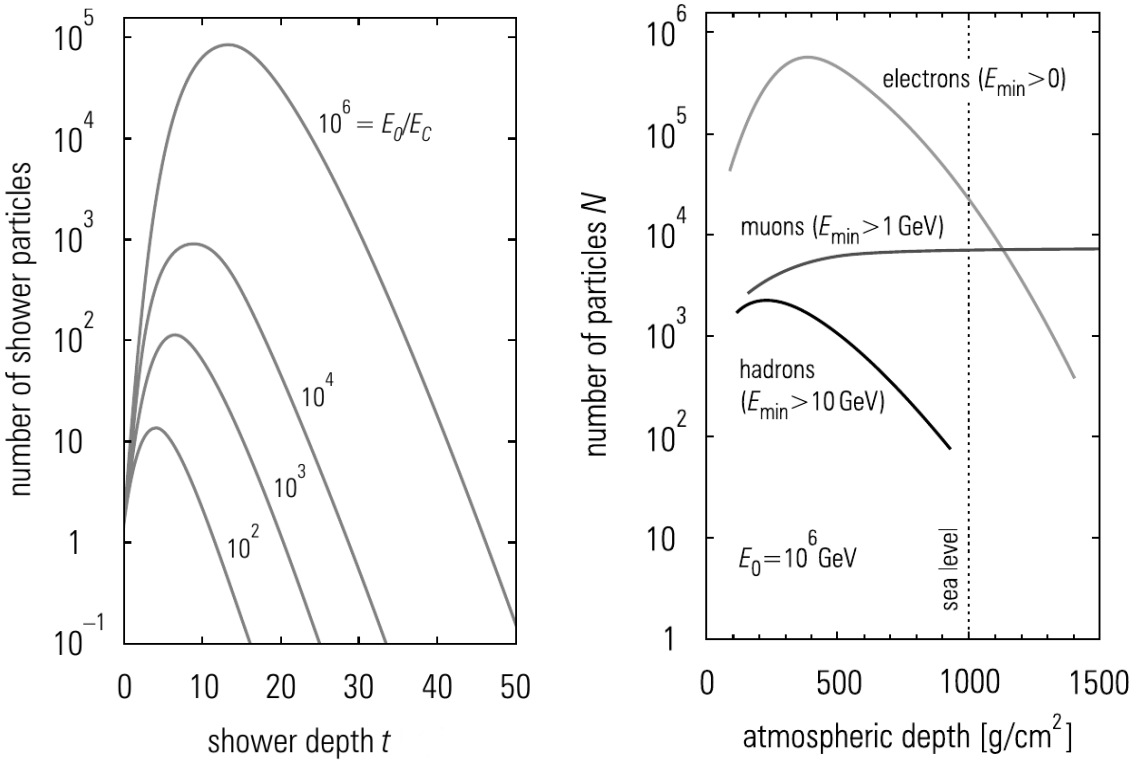

(a) (b)

Figure 1.6: (a) The longitudinal profile of an electromagnetic cascade for different energies of the primary particle. The shower depth is the slant depth in units of the radiation length. (b) Development of the longitudinal profile divided into the different components of an electromagnetic air shower for a primary energy of $E_0 = 10^{15}$ eV [27].

1.4 Photons as Primary Particles

The most obvious cosmic photon exposure on Earth is the visual light emitted by stars such as the sun. In fact these photons with wavelengths in the nanometer range are just a small part of the overall spectrum of extraterrestrial photons. The photon flux reaches from radio waves with energies of a fraction of an eV up to MHz X-rays and even further into the γ-ray regime as shown in Fig. 1.7. It is possible to measure the photons up to 100 TeV. Above these energies in the EeV range the overall cosmic ray flux decreases to only a few particles per square kilometer per year (see 1.3) and it is only possible to make statistical statements on the cosmic ray composition. Until now no significant photon flux was measured. The current upper limits on the flux are shown in Fig. 1.8. Values for the upper limits of the integral UHE photon flux up to $10^{17.2}$ eV are given by KASCADE-Grande [34] and EAS-MSU [35]. For energies above 10^{18} eV the Pierre Auger Observatory [36] [37] and Telescope Array [38] have published upper limits on the photon flux. In addi-

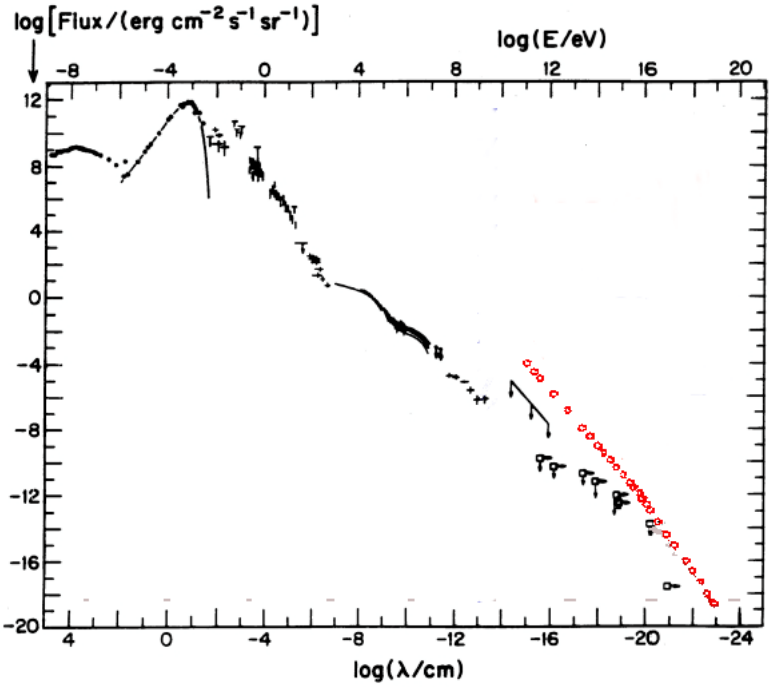

Figure 1.7: The spectrum of cosmic ray photons measured on Earth as a function if the wavelength (black markers). For wavelengths below 10^{-15} cm only flux limits are given (black circles) in comparison to the overall cosmic ray flux (red circles) [33].

tion to that two theoretical GZK photon flux bands (see GZK-effect in section 1.2) are shown for initial iron nuclei and protons calculated by Kampert [39] and linearly extrapolated into lower energy regions. This work will focus on the energy range between 10^{17} and 10^{18} eV. With a simulation study referring to the Pierre Auger Observatory (see chapter 2) possible upper limits of the integral photon flux will be derived (see chapter 3).

A detection of a photon flux may help discovering new physics since photons are neutral particles and would point right back to their source or point of creation. As long as there is no photon flux measured at the highest energies, there is a lot of room for theories predicting a photon flux below the already derived flux limits. These models are mainly following two different approaches. The first category of theories are the "bottom-up" models which are based on the acceleration of protons or heavier nuclei which then lose energy through the GZK effect to produce UHE photons by pion decay (see equation 1.2). The "top-down" models assume UHE photons to be produced directly through the decay or the annihilation of not yet discovered particles. These particles could be caused by topoligical defects or

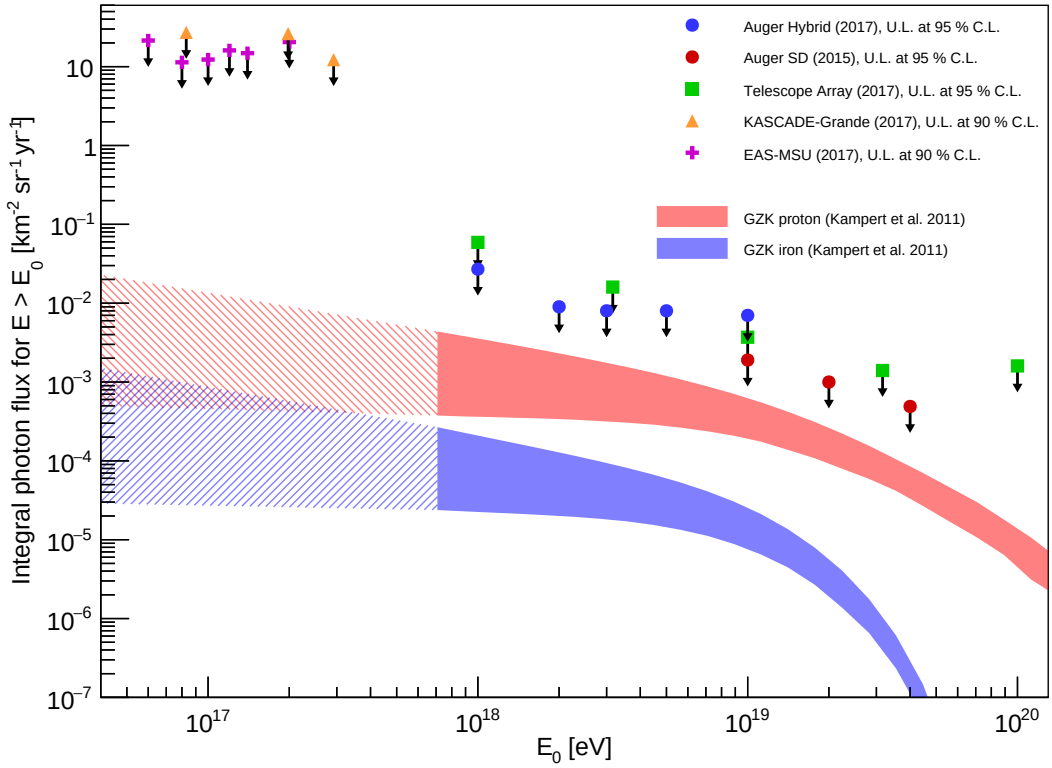

Figure 1.8: Current integral UHE cosmic ray photon flux limits as measured by the Pierre Auger Observatory [36] [37], Telescope Array [38], Kascade-Grande [34] and EAS-MSU [35], as well as theoretical bands for GZK photons initiated by iron nuclei and protons calculated by Kampert [39]. The shaded areas are a linear extrapolation of the theoretical GZK bands.

remnants of the early universe. The photon fraction in the UHE cosmic ray flux would be much higher in these models than in the bottom-up approaches due to a significant occurance of neutral pions [40]. Nowadays the photon flux limits are brought down to a point where the top-down models are getting more unlikely than the acceleration-based bottom-up approaches. Read a more detailed review on the two theory categories in [41].

The detection of cosmic rays in the high energy spectrum is not possible by direct measurements due to the low cosmic ray flux above the knee. The extensive air showers induced by the primary cosmic rays can be detected instead. Some features of the EAS can be used to distinguish which shower was induced by a photon or by other cosmic ray particles like protons or heavier nuclei, since different primary particles lead to different development of the shower components mentioned in section 1.3.

One characteristic observable of extensive air showers that depends on the mass of the primary particle is the slant depth at the shower maximum $X_{\max}$. The predic-

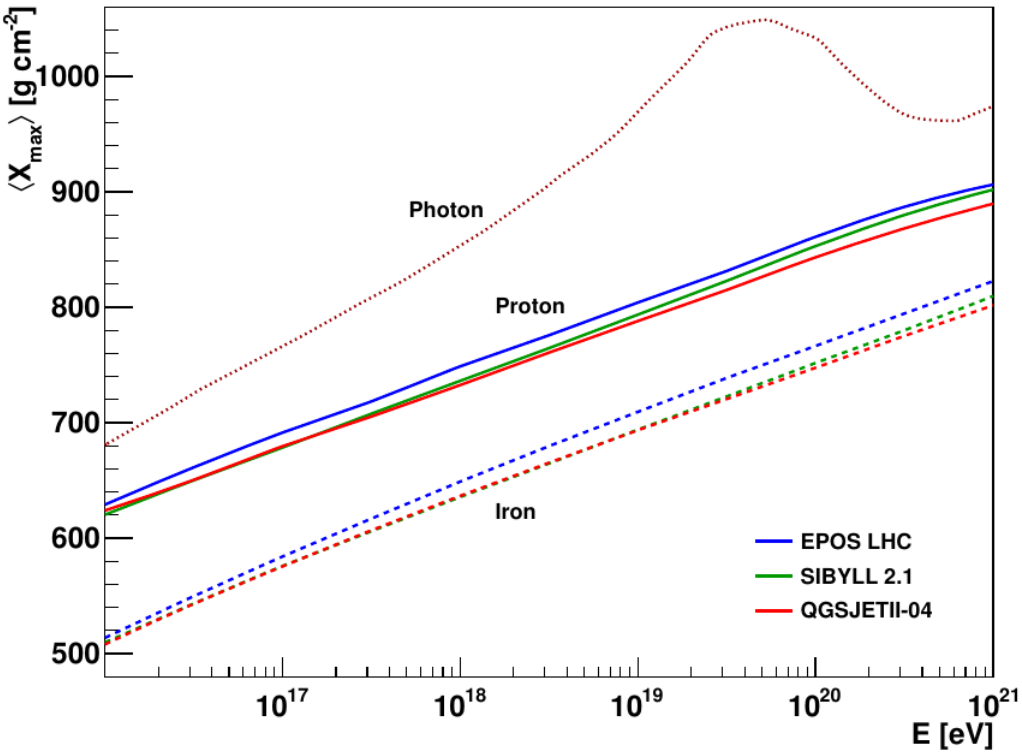

Figure 1.9: The average $X_{\max}$ for extensive air showers induced by photons, protons and iron for energies between 10^{16} eV up to 10^{21} eV on a logarithmic scale. The simulations have been done for EPOS LHC, SIBYLL 2.1 and QGSJETII-04 as hadronic interaction models. The different interaction models have basically no impact on the $X_{\max}$ of air showers initiated by photons since those induce almost pure electromagnetic showers. [42]

tion for the average $X_{\max}$ for different energies of the primary particle for photons, protons and iron simulated with different hadronic interaction models can be seen in Fig. 1.9. Regardless of the hadronic interaction models the $X_{\max}$ for protons is on average always higher than the one for iron. This can be explained by the asymptotic freedom of high energetic nuclei which behave almost like individual particles in the center of mass frame of the collision. An air shower induced by a nucleus with the mass number A and the energy E could be represented by A proton showers with a total energy adding up to E. This leads to a more dominant hadronic component and to a lower $X_{\max}$. The average $X_{\max}$ for photons is even larger than the one for protons, since a photon induces an almost purely electromagnetic shower and those develop a little delayed compared to hadronic showers.

For all particles the average $X_{\max}$ rises with energy, but in photon induced showers additional processes play a role which cause a maximum at about $10^{19.5}$ eV. Above some 10^{18} eV the Landau-Pomeranchuk-Migdal (LPM) effect causes an increase of the average $X_{\max}$. The cross sections of the crucial processes for electromagnetic

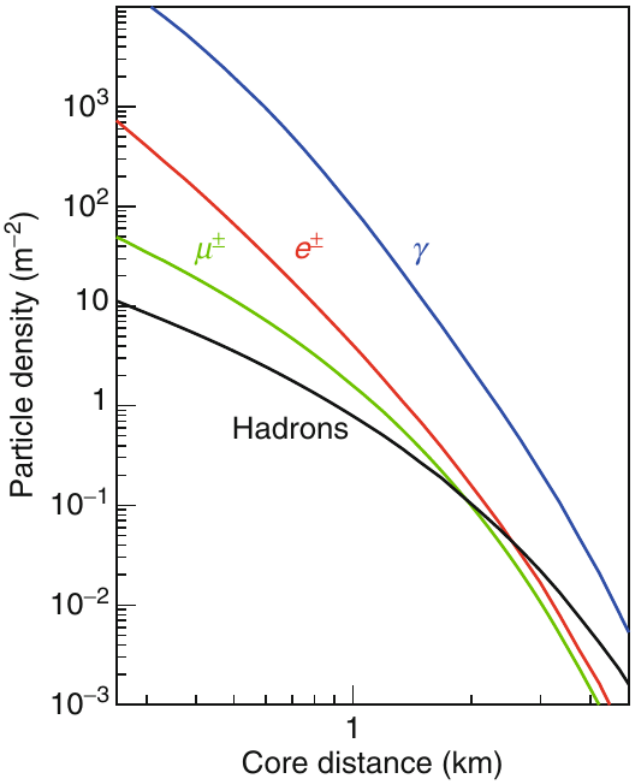

(b)

Figure 1.10: The particle density as a function of the core distance on ground for each component of an extensive air shower. The distributions are calculated from MonteCarlo simulations of extensive air showers for an atmospheric depth of 870 g cm^{-2} with vertical protons with an energy of 10^{19} eV as initial particles [47].

showers, pair production and bremsstrahlung, are getting smaller with higher energies due to destructive interferences between neighboring scattering centers [43] [44]. Getting to energies higher than $10^{19.5}$ eV the preshower effects counteract the LPM effect and lead to a decrease of the average $X_{\max}$ again. The process of preshowering describes the interaction of high energetic photons with the Earth's magnetic field. Before an UHE photon can reach the atmosphere it may convert into an electron-positron pair which then emits synchrotron radiation leading to an electromagnetic shower. When those particles finally reach the atmosphere they are inducing multiple air showers but with a lower initial energy. These showers therefore have a smaller $X_{\max}$ [45] [46].

The lateral distribution is also sensitive on the primary particle. Fig. 1.10 shows the lateral distributions for each component of an extensive air shower on the ground. While the hadronic component produces the flattest lateral profile, the electromagnetic components have a significantly steeper distribution. Since proton induced air showers have a smaller hadronic component than heavier nuclei, their lateral particle

distribution is steeper. The lateral profile of photon induced air showers is expected to be even steeper since they are mainly electromagnetic. The expected signal on the ground $S(r)$ in a distance r from the shower core can be obtained using

$$S(r) = S_{1000} \times f_{\mathrm{LDF}} \tag{1.6}$$

with S_{1000} the average expected signal at a distance of 1000 m and a lateral distribution function f_{LDF} which is a modified version of the aforementioned NKG function (see equation 1.5):

$$f_{\mathrm{LDF}}(r) = \left(\frac{r}{1000\,\mathrm{m}}\right)^{\beta} \left(\frac{r + 700\,\mathrm{m}}{1700\,\mathrm{m}}\right)^{\gamma} . \tag{1.7}$$

Here β and γ are shape parameters which define the steepness of the LDF.
The here mentioned characteristics of cosmic ray air showers regarding the longitudinal as well as the lateral profile are always averaged and statistical statements, which means that on a shower-to-shower basis these may vary heavily due to their dependency on the density and momentum distributions of the first interactions in the atmosphere. Nevertheless these air shower characteristics can be used to distinguish between photon induced extensive air showers from those originating in other primary particles on a statistical basis in order to improve the existing photon flux limits or even find UHE photons.

2 The Pierre Auger Observatory

The Pierre Auger Observatory aims to detect cosmic ray particles with energies above 10^{17} eV [48]. In the first proposal in 1996 [49], an observatory with two locations was planned, one in the northern and one in the southern hemisphere. Due to financial issues just the southern site was built in the Argentinian Pampa near Malargüe, Mendoza. The Pierre Auger Observatory is measuring cosmic rays using a hybrid method combining two well-established detector types. First there are 1600 water-Cherenkov tanks serving as a surface detector array (SD) to measure the particles of an extensive air shower reaching the ground. They are arranged in a hexagonal pattern with a distance of 1500 m between the stations and cover an area of 3000 km^2. The SD is overlooked by the second part of the Pierre Auger Observatory: The fluorescence detector (FD). It consists of four sites with six fluorescence telescopes each and measures the fluorescence light produced by a particle shower in the atmosphere.
In 2010 two low-energy enhancements were installed in addition to the existing detectors. With the AMIGA upgrade, the SD has been expanded in the western area with detector stations in between the existing ones with a distance of 750 m between the stations, again in a hexagonal pattern. In addition to that Muon counters have been installed underneath them [50]. This is necessary to compensate the smaller amount of shower particles arriving at ground level when an initial particle with energies down to 10^{17} eV hits the Earth's atmosphere (see section 1.3). The other extension are the three High Elevation Auger Telescopes (HEAT) [51] installed near the FD site in Coihueco. Low-energy cosmic-ray showers develop higher up in the atmosphere which HEAT is taking account of by expanding the field of view of the already existing telescopes to higher zenith angles. A schematic depiction of the whole Pierre Auger Observatory can be seen in Fig. 2.1. In the following sections, the detector components will be described in greater detail.

2.1 The Surface Detector

The SD consists of 1600 cylindrical polyethylene tanks arranged on a hexagonal grid with a spacing of 1500 m. The energy threshold for the full trigger efficiency

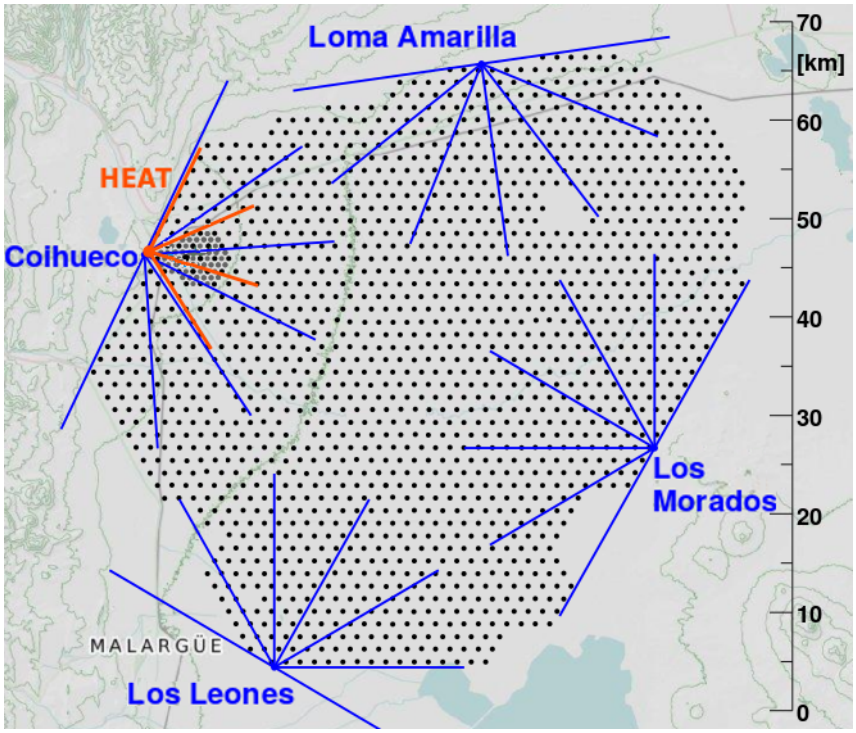

Figure 2.1: Schematic layout of the Pierre Auger Observatory [52].

is $10^{18.5}$ eV for zenith angles below 60°. Every tank holds 12,000 litres of purified water in which the shower particles emit Cherenkov radiation. The Cherenkov light is picked up by three photo-multipliers tubes (PMTs) mounted at the top of the tank. To increase the light yield the inner surface of the tanks is lined with a reflective material. Before the signals are transmitted to the central data acquisition system (CDAS) via a radio link it has to be amplified. This is done with two amplification channels, the Low Gain (LG) and the High Gain (HG) channel with a nominal relative amplification of 32 [53]. Both channels are transmitted to be processed, but in the first place the HG signal is used. The LG signal is a backup signal for the case of saturation of the HG. The analog signals are constantly digitized by an analog-to-digital-converter (ADC) with read-out frequency of 40 MHz which automatically divides the signal up into time bins corresponding to 25 ns each. The first two trigger levels are performed directly at each station. The T1 trigger demands a signal intensity of all three PMTs over a certain threshold in one time bin or a lower threshold over 13 time bins called a time-over-threshold trigger (ToT). The preselected signal then has to pass the T2 trigger system which is basically the same with stricter limits on the intensity. When a signal passes the T1 and T2 triggers a time and shape information is sent to the CDAS which then checks SD stations nearby the triggered station on coincident signals. If the time and shape stamps of the single stations fit to an EAS the data is requested from each station and

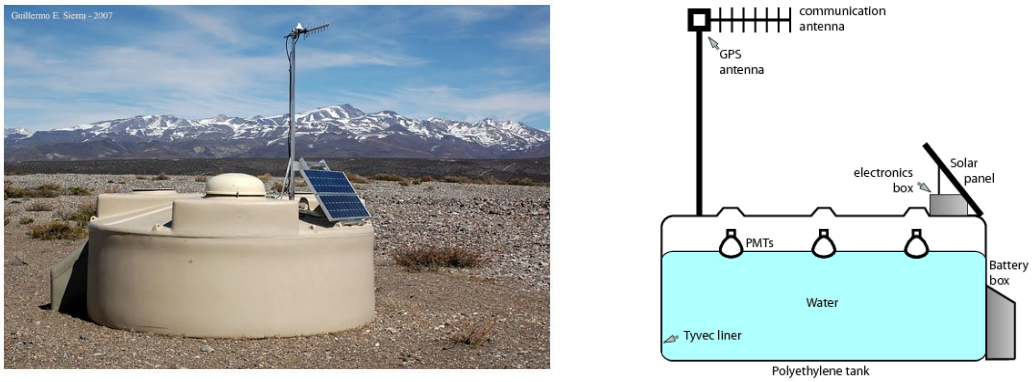

(a) (b)

Figure 2.2: (a) A photograph of a SD station in the Argentinian Pampa (Credit: Guillermo E. Sierra - 2007). (b) An illustration of an SD tank [55].

permanently stored in the CDAS (see [54] for more information). The SD signal is expressed in units of the average signal of a muon traversing a SD station vertically (VEM).
Mounted on top of each station is a solar panel which provides enough energy for the electronics, making each station fully autarkic. The duty cycle of data-taking with the SD is close to 100 %.

2.2 The Fluorescence Detector

The Fluorescence Detector (FD) consists of 27 air-fluorescence telescopes at 4 sites at the border of the SD array to observe the atmosphere above it. Six telescopes each are placed at the sites Los Leones, Loma Amarilla, Los Morados and Coihueco [56], while three additional telescopes called the High Elevation Auger Telescopes (HEAT, detailed information in section 2.3.2) are located close to Coihueco. The concept of the FD is based on the fact that EAS interact with the atmospheric nitrogen molecules and excite them. When falling back to the ground state, they emit fluorescence light in the range of 300 to 430 nm [57], where the amount of the fluorescent light is proportional to the energy deposited in the atmosphere. The longitudinal air shower profile $\frac{\mathrm{d}E}{\mathrm{d}X}$ can be derived by looking at the fluorescence light as a function of the atmospheric slant depth. The integral of that shower profile corresponds to the energy of the primary particle with a little correction taking account of the particles which do not produce any fluorescence light like neutrinos or muons. For protons and nuclei this "invisible light" correction is about 10 % and for photons of the order of 1 % [56].
A schematic picture of a FD telescope is displayed in Fig. 2.3a. The data taking can only take place during clear, moonless nights, which is about 13 % of the total time.

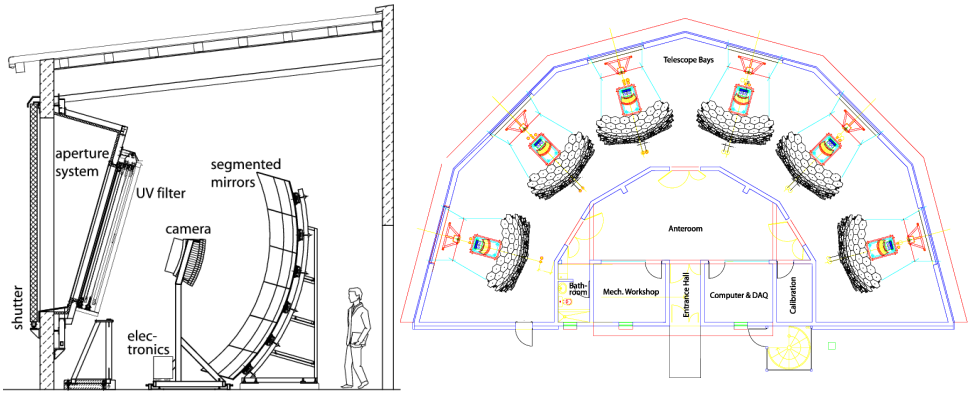

(a) (b)

Figure 2.3: (a) A schematic image of one fluorescence telescope. (b) The Layout of an FD site consisting of six fluorescence telescopes [56].

The shutter doors are always closed if that is not the case. If data can be taken, the fluorescence light passes an UV filter and a Schmidt correction plate [58] to take account of the spherical aberration of the mirror. This mirror focuses the light onto a camera system consisting of 440 PMTs (pixels), which are read out every 100 ns by the electronics.

At each FD site, six telescopes are combined as seen in Fig. 2.3b. One telescope has a solid angle coverage of $30° \times 30°$, which adds up to a total coverage of 180° in azimuth for each FD site. Picture 2.1 shows that the atmosphere over the whole SD array can be covered with this construction. The threshold for full trigger efficiency for the FD is 10^{18} eV.

The properties of an EAS can be derived using data measured by the FD. First the calorimetric energy as mentioned before. The energy E deposited in the atmosphere can be measured as a function of the slant depth X of the shower giving the longitudinal air-shower profile. This can be fitted with a Gaisser-Hillas function and then integrated to obtain the whole energy deposit. Also a direct measurement of $X_{\max}$ is possible. The attenuation in the atmosphere is an important factor in this equation too since it has to be known how much fluorescent light was actually emitted by the EAS. To take account of this, the aerosol content in the atmosphere is measured constantly by the Central Laser Facility (CLF) and the eXtreme Laser Facility (XLF), which fire pulses of 355 nm-lasers into the air [59]. These pulses are then deflected by the aerosols and measured by the FD telescopes. Also the air pressure, temperature and weather situation is continuously monitored.

Another property obtained by the FD is the arrival direction of the EAS. Under usage of the before mentioned time resolution of 100 ns a time ordering of the triggered pixels of the camera is possible. An example trace of triggered pixels as detected by the FD can be seen in Fig. 2.4. The shower detector plane (SDP) contains the

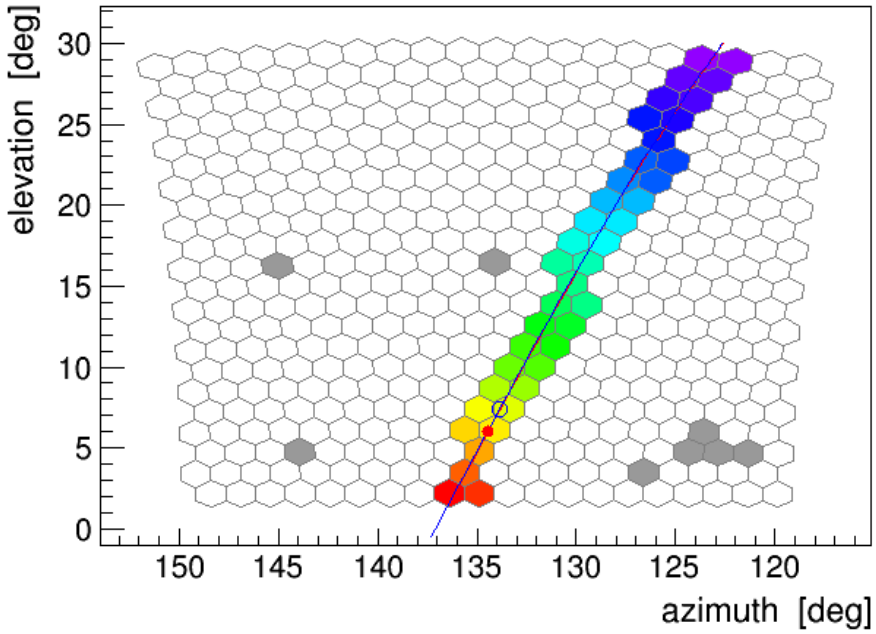

Figure 2.4: Trace of triggered pixels on a FD telescope. The color refers to the arrival time.[56]

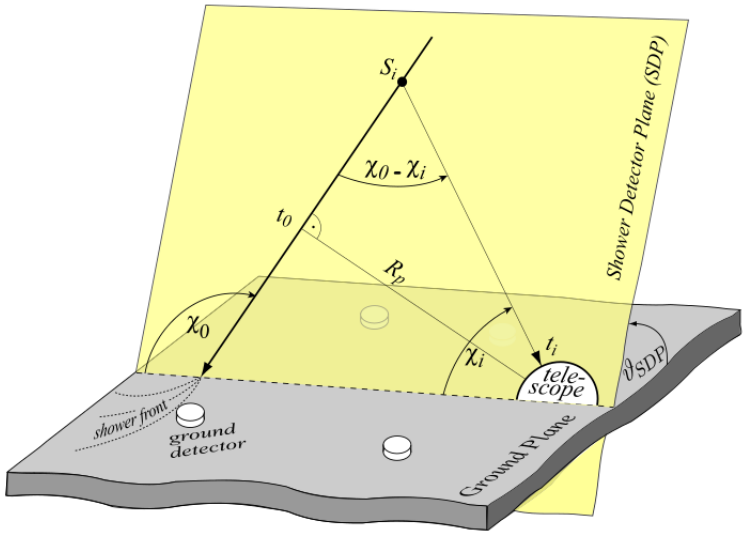

Figure 2.5: Illustration of the derivation of the shower detector plane and its parameters to reconstruct the track of an insicident air shower. [56]

information about the FD site and the air shower through the triggered pixels of the camera. In combination with the time dependency of the triggered pixels the shower axis can be obtained. Figure 2.5 shows the geometry of the reconstruction of the shower axis using the arrival time of the fluorescence light at the detector. The variable t_0 denotes the time when the shower axis has the closest distance R_p to the telescope and χ_0 is the angle of incidence of the shower with respect to the ground

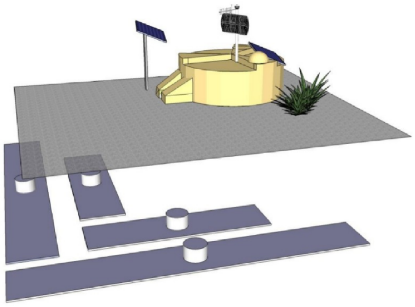

(a)

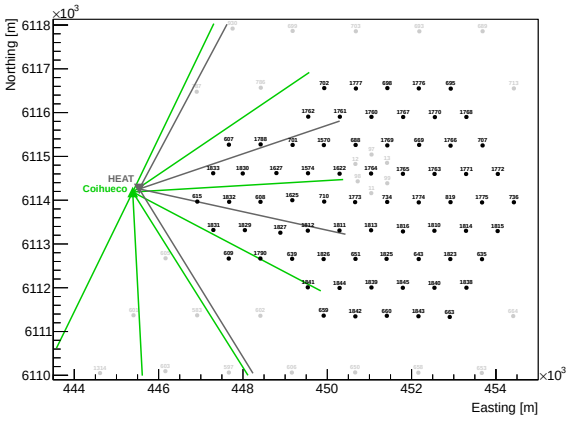

(b)

Figure 2.6: (a) Layout of four muon detectors underneath a SD station. (b) Layout of the 750 m-array located in between the regular SD stations near Coihueco [60].

plane. The arrival time of the fluorescent light t_i is correlated to the viewing angle χ_i of each pixel through

$$t_i = t_0 + \frac{R_p}{c} \tan\left(\frac{\chi_0 - \chi_i}{2}\right) \tag{2.1}$$

with the speed of light in vacuum c.
If an event gets detected by more than one FD site, the reconstruction of its properties is even more precise. For these so-called stereo, triple or quadruple-events the information of all sites can be used and evaluated.

2.3 Low Energy Enhancements

The Pierre Auger Observatory was originally built to measure extensive air showers with energies of the primary particle above 10^{18} eV. Cosmic rays in this energy range are expected to be of extragalactic origin (see section 1.2). The energy range below that is taken as a transition region from the galactic to the extragalactic component of the cosmic rays. To also cover these energies down to 10^{17} eV two enhancements of the regular detectors have been installed: AMIGA and HEAT.

2.3.1 Auger Muons and Infill for the Ground Array (AMIGA)

The AMIGA enhancement is located in the western region of the SD array near Coihueco. It consists of two components: Muon detectors underneath the surface and a denser grid of SD stations with a spacing of 750 m. The muon detectors are placed 2.3 m under the surface alongside the SD stations of the infilled 750 m ar-

ray. At this depth, the electromagnetic component of an air shower is almost fully absorbed, leaving just the muons to trigger the plastic scintillators strips of the detectors. The number of muons is highly correlated to the mass of the initial particle. The positioning of the muon detectors is shown in figure 2.6a. First results of the measurements of the AMIGA engineering array can be found in [60].
The other component of the AMIGA enhancement is the 750 m array (also called infill array). In total 71 additional water-Cherenkov detectors have been installed in between the SD stations of the 1500 m array. They are equipped like the regular SD stations but with a more powerful wireless connection to maintain the bandwidth needed for the transmission of the measurements of the station itself, but also for the muon counters placed below them. The trigger system has also been adopted from the 1500 m array. With the additional SD stations the threshold for full trigger efficiency is $10^{17.5}$ eV for zenith angles below 55°.

2.3.2 High Elevation Auger Telescopes (HEAT)

Figure 2.7: The HEAT telescopes near Coihueco in the regular upwards pointing mode. [61]

The HEAT enhancement is installed close to the existing FD site Coihueco. The aim is to detect fluorescence light of air showers with primary energies below 10^{18} eV. These lower energetic EAS develop higher in the atmosphere. Especially the value of $X_{\max}$ can not be reconstructed by the regular FD sites at Coihueco. To take account of that the three additional HEAT telescopes are aligned to extend the field of view from 30° in elevation to 60°. Figure 2.7 shows a photograph of the tilted HEAT telescopes. While the telescope itself is built in the same way as the regular FD telescopes, they are lifted to higher angles by a hydraulic system. The electronics

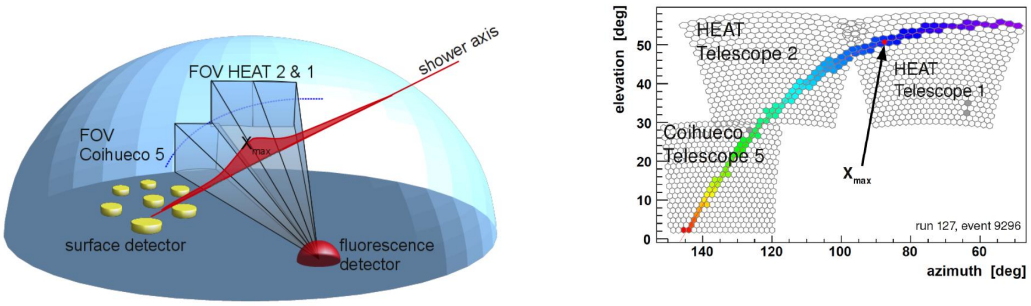

(a) (b)

Figure 2.8: A shower reconstructed by a combination of the Coihueco FD site (telescope 5) and the HEAT telescopes (telescopes 1 and 2). (a) A schematic of the fields of view of the telescopes observing an air shower combined with the SD measurement. (b) The same shower as an event displayed by the telescopes. It starts in the upper right corner going to the lower left corner. The position of $X_{\max}$ is observed by HEAT telescope 1. [61]

are also adopted by the regular FD with a few adjustments. The data aquisition system (DAS) has a 20 MHz instead of a 10 MHz sampling rate to be able to detect the showers which are especially close to the telescope and have to be processed faster [61].

The combination of the Coihueco FD site and HEAT can be seen in Fig. 2.8. The shower maximum of this example shower would be outside of the field of view of the regular FD telescopes at Coihueco. With the HEAT enhancement, this area is also covered and a reconstruction is possible. The combined shower reconstruction of both telescope sites is referred to as HECO (HEAT + Coihueco).

Since June 2010, the HEAT enhancement is providing data which can be used for the reconstruction [62].

3 Simulation Study

To estimate the performance of the analysis described in this chapter, a set of simulations was produced. In the following the production of such simulations is explained as well as the analysis procedure.

3.1 Production of Simulations

The process is divided into air-shower simulations and the simulation of the corresponding detector output. After that a series of selection criteria is applied to take only showers with well reconstructed geometry and profile into account.

3.1.1 Air Shower Simulations with CORSIKA

The production of the simulations of particle air-showers is made with CORSIKA 7.5700 [63]. The EPOS LHC option is used as the hadronic interaction model for high energies [64], while the low energetic part is simulated using the FLUKA (version 2011.2c-4) model [65]. The incident cosmic particles are chosen to be photons and protons, since the latter are the most photon-like particles and would give the most conservative estimate on the separation power of the experiment (see section 1.4). Photon induced air showers are in this thesis often referred to as signal events, while background events are represented by the ones induced by protons. The particles are produced in 6 energy bins from $10^{16.5}$ to $10^{19.5}$ eV in steps of 0.5 in $\log_{10}(E\,[\mathrm{eV}])$. The zenith angle is randomly chosen between 0° and 65°, such that the particle flux is equal in all solid angle elements [66]. In order to decrease the needed computing time and disk space a process called "Thinning" is taking place, when the secondary particles have reached a fraction of 10^{-6} of the energy of the primary particle E_0. Reaching this energy one particle is representatively simulated for a certain amount of particles of the same type, which then are discontinued. A detailed description of the thinning process can be read in [66].
The Atmosphere is set to be the U.S. standard atmosphere, the magnetic field as it is in Malargüe (horizontal component in northern direction: $20.1\,\mu\mathrm{T}$; vertical component downwards: $-14.2\,\mu\mathrm{T}$) and the altitude to 1452 m above sea level which is the average value for the Pierre Auger observatory.

3.1.2 Detector Simulations with Offline

In order to simulate the detector response of these air showers the Auger $\overline{\text{Off}}\underline{\text{line}}$ Framework v3r3p4 gcc4.9 [67] is used. With time dependent Monte Carlo simulations the concrete detector status at a given time is taken into account. The detector status is read out of a SQLITE-database and the impact time is chosen randomly out of the time hybrid detection was possible in the period from 01.06.2010 to 31.12.2015. The core position is likewise distributed randomly over the whole 750 m array, which is overlooked by the HECO telescopes. In addition to that the first row of stations around that area is also considered since some showers coming in there are reconstructed within the 750 m array and vise versa. To increase the statistics, every CORSIKA air shower is processed five times with different impact points and time. Table 3.1 shows the overall produced CORSIKA and $\overline{\text{Off}}\underline{\text{line}}$ simulations. The computation of a small amount of simulations got canceled which is the reason for a slightly decreased number of $\overline{\text{Off}}\underline{\text{line}}$ events. The cancellations are due to hardware or network issues in the computing setup or the duration of the computing exceeded the time limit. The fraction of aborted simulations is not significantly big and can be neglected.

Energy bin in $\log_{10}(E\,[\text{eV}])$	16.5 - 17.0	17.0 - 17.5	17.5 - 18.0	18.0 - 18.5	18.5 - 19.0	19.0 - 19.5
Number of CORSIKA showers	5000	2000	2000	1000	1000	1000
Number of $\overline{\text{Off}}\underline{\text{line}}$ events for photons	25000	9995	9700	5000	5000	5000
Number of $\overline{\text{Off}}\underline{\text{line}}$ events for protons	24990	9985	9690	4990	4990	4990

Table 3.1: Produced Simulations for six energy bins. The number of CORSIKA air-shower simulations is produced for each photons and protons. Every shower is used five times in the detector simulations. Due to some canceled computations, the number of Offline events is slightly decreased.

3.1.3 Event Selection

It is necessary to make sure that the used simulations have a well reconstructed geometry and profile. To achieve that, a set of selection criteria is applied on the data set. The cuts used in this work are basically the cuts used in the photon analysis for energies above 1 EeV [36] with some additional X_{max} criteria of the ICRC 2017 contribution [68]. In the following the cuts will be described and linked to table 3.2 with the numbers in brackets.

The first set of cuts is related to the FD reconstruction. The number events *nTOT* in table 3.2 before the FD cuts are applied refers to the number of FD events which

can be up to three since every shower can trigger multiple FD telescopes (Coihueco, HEAT and HECO). At first it is checked, whether the measured event is induced by a cosmic particle or by one of the two laser facilities (Central Laser Facility (CLF) and eXtreme Laser Facility (XLF) [59]), which where built to test the aerosol content in the air (1,2). Since the data used in this work is simulated, these cuts are always leaving 100 % of the showers unaffected. The following cut asks if the event triggered the HECO telescope, all other telescopes are not taken into account (3). For this analysis no events were produced when the FD telescopes were not up and running(4, 5) or had bad pixels (7), which lets the cut asking for that also leaving the data set unaffected. Further the events which leave the telescopes pixels saturated are excluded (6), as well as data with a bad reconstruction (8).
The following cuts are applied to check if the geometry of the shower is well reconstructed. At first it is checked whether the event has a hybrid reconstruction (9). Also it is required that the shower core is not further away from a SD stations than 1500 m (10) and the minimum viewing angle between the shower axis and the telescopes should not be smaller than 20° (11) to reject events pointing directly towards the FD. The electromagnetic component of air showers is absorbed in the atmosphere which reduces the trigger efficiency of very inclined showers. To prevent a bias caused by this effect, a zenith angle below 60° is requested (12).
One of the most important characteristic observables in this analysis is $X_{\max}$. Thus it is important that the shower maximum is well measured and lies in the field of view of the HECO telescopes (13) and the uncertainty on that value should not be bigger than the value itself (14). To make sure the profile of the shower is well reconstructed, the holes in the profile should not exceed 30 % (15). For a good profile reconstruction a constraint on the χ^2 of the Gaisser-Hillas fit is required (16). Another cut on the events is a minimum photon energy (17). The uncertainty on the reconstructed photon energy should furthermore not be larger than 20 % (18).
With the last two cuts the atmosphere databases are checked. Periods without knowledge on the aerosol and molecular content are excluded, as well as events that happened when the vertical aerosol optical depth (VAOD), measured from the ground to an altitude of 3 km, exceeded 0.1 (19, 20).
The last two cuts refer to the SD measurements. Here *nTot* stands for the number of air shower simulations since one shower could create just one SD event. At first a minimum number of four active stations on the first hexagon around the station with the strongest signal is requested (21). This is often not passed by showers which have their shower core outside of the 750 m array or in the near of stations that were not working at that time. Also it is often hard to trigger four stations if the primary particle has a low energy down to $10^{16.5}$ eV, because these showers

develop higher in the atmosphere and have a smaller lateral footprint. The second SD criterion demands the shower to have the possibility to calculate S_4 (equation 3.4) (22). Since it was previously made sure the shower has four active stations on the first hexagon, most of the remaining showers are passing that second test.
Table 3.2 shows which cut left how much of the simulated photon air showers unaffected. The total number of FD events is 73818 for photons and 75543 for protons. In the FD part all triggered telescopes are counted, which is up to three for Coihueco, HEAT and HECO. The biggest loss of events happens when the HECO reconstruction is demanded, which excludes around 61 % of the events for photons and 63 % for protons respectively. The following cuts are not reducing the data set as significantly as the ones mentioned before with one exception. The fact, that $X_{\max}$ has to always lie in the field of view of the telescopes is rejecting up to 38 % of the photon events and around 27 % of the proton events respectively. The big difference for each particle is due to the fact, that photons showers with high energies are more likely to have an $X_{\max}$ below the field of view. The cut selection for the SD events has one major constraint, which is the requirement on 4 active stations around the station with the biggest signal (21), this cuts off around 38 % of the data for photons and around 33 % for protons.

		Events left unaffected			
		Photons		Protons	
Cut No.	FD-Cuts	#	[%]	#	[%]
	nTot	73818	–	75543	–
1	!isCLF	73818	100	75543	100
2	!isXLF	73818	100	75543	100
3	eyeCut (100000)	28652	38.81	27864	36.88
4	heatOrientationUp	28652	100	27864	100
5	HeCoHasUpTime	28652	100	27864	100
6	skipSaturated	26399	92.14	25388	91.11
7	noBadPixelsInPulse	26399	100	25388	100
8	good10MHzCorrection	26399	100	25388	100
9	hybridTankTrigger (2)	25097	95.07	24389	96.07
10	maxCoreTankDist (1500)	25096	100	24382	99.97
11	minViewAngle(20)	20505	81.71	18202	74.65
12	maxZenithFD(60)	20076	97.91	17665	97.05
13	xMaxInFOV (0)	12516	62.34	12924	73.16
14	XmaxErrorLessThenXmax	12512	99.97	12919	99.96
15	maxDepthHole (30)	12133	96.97	12247	94.8
16	profileChi2Sigma (5. -1.42)	11959	98.57	12026	98.2
17	minLgPhotonEnergyFD (0)	11959	100	12026	100
18	photonEnergyError (0.2)	11938	99.82	12011	99.88
19	hasMieDatabase	10042	84.12	10011	83.35
20	maxVAOD (0.1)	9468	94.28	9365	93.55
	SD-Cuts				
	nTot	59695	–	59635	–
21	minTankOnCrownInfill (4)	36998	61.98	39826	66.78
22	hasSbInfill	36794	99.45	39747	99.8

Table 3.2: Cut statistics of the event selection of the simulated photon data set with energies between $10^{16.5}$ and $10^{19.5}$ eV. Every cut is explained in section 3.1.3. For the SD cuts, the number of events is the number of remaining showers after the cut was applied. The FD cuts refer to the number of all triggered telescopes. The percentage column shows which amount of events passes the respective cut.

3.2 Observables

For the simulation study the observables $X_{\max}$, S_4 and N_{stations} are utilized. These observables are the same as used in the previous photon search for energies above 10^{18} eV [36] and showed to be a potent combination. In the following the separation power of the variables will be investigated.

3.2.1 $X_{\max}$

At first the focus will lie on the observable $X_{\max}$, the atmospheric depth at the shower maximum. The distribution for the whole simulated data set from $10^{16.5}$ and $10^{19.5}$ eV is shown in figure 3.1, as well as the plot for the signal efficiency ε versus background rejection ρ. The signal efficiency ε is the fraction of $N_\gamma(x \geq x_{\text{cut}})$, the number of events with a larger value than a certain cut value x_{cut}, and the whole number of signal events $N_{\gamma,\text{tot}}$.

$$\varepsilon = \frac{N_\gamma(x \geq x_{\text{cut}})}{N_{\gamma,\text{tot}}}\,. \tag{3.1}$$

The background rejection ρ is respectively the fraction $N_p(x < x_{\text{cut}})$ of the number of background events with a value smaller than a certain cut value and the whole number of background events:

$$\rho = \frac{N_p(x < x_{\text{cut}})}{N_{p,\text{tot}}}\,. \tag{3.2}$$

To use these values as an indicator for the separation power of the observable, the function for the background rejection depending on the signal efficiency $\rho(\varepsilon)$ is obtained. At first the value for x_{cut} is obtained for a certain signal efficiency between 0 and 1. The corresponding background rejection is then calculated with formula 3.2. This process is done for an arbitrary (big) number of times to get $\rho(\varepsilon)$. The value which serves as a benchmark is the background rejection at 50 % signal efficiency. For values close to 100 % the distributions of the observable have a large separation.
In addition to that the merit factor is taken into account. It is calculated with

$$\eta = \frac{|\mu_\gamma - \mu_p|}{\sqrt{\sigma_\gamma^2 + \sigma_p^2}}\,, \tag{3.3}$$

where μ_γ and μ_p are the mean values of the photon and proton distribution with their respective standard deviation σ_γ and σ_p. The merit factor is a measure of overlap of two distributions. A small merit factor towards 0 would indicate two distributions with either a similar mean value or a large width and with that a small

separation. For large separations it is the other way around and the merit factor is also larger. Distributions with a merit factor exceeding 1 are considered to be "good". This value is however not taking the shape of the distributions into account, just the mean value and the standard deviation. Thus the merit factor should just be considered in combination with the value of the background rejection at 50 % signal efficiency.

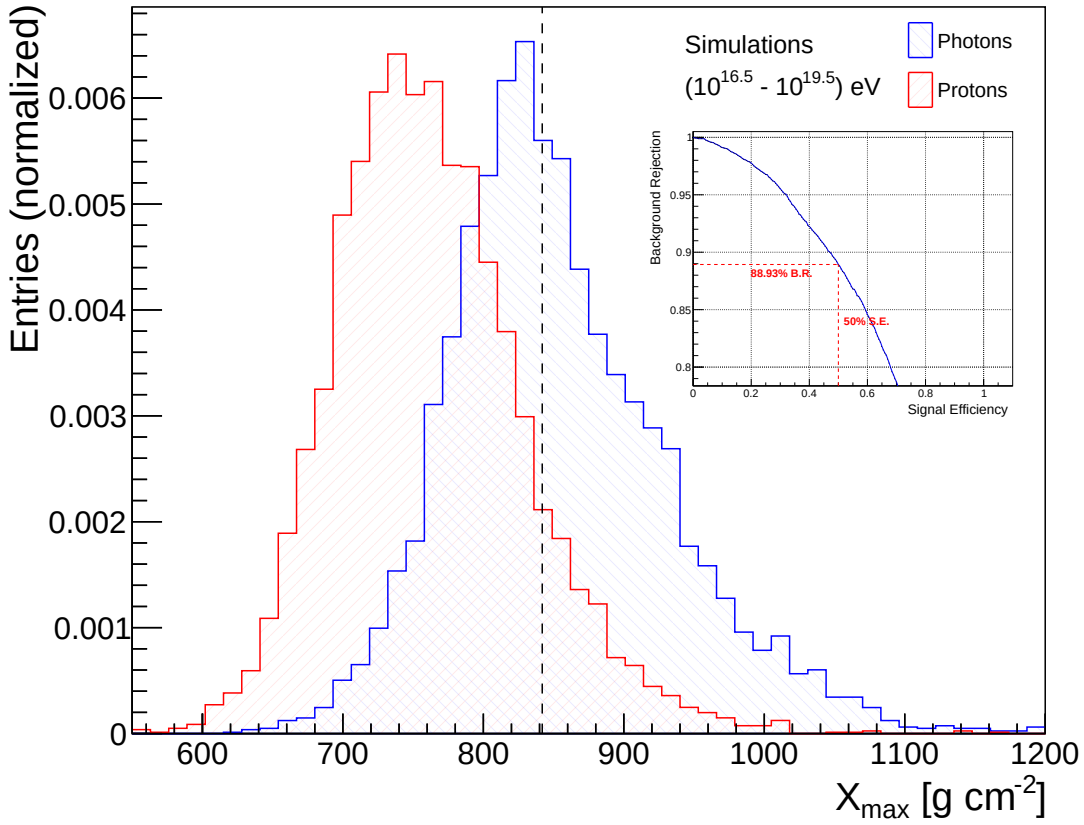

Figure 3.1: Distributions of the $X_{\max}$ value for simulations of extensive air showers induced by photons (blue) and protons (red) with energies between $10^{16.5}$ and $10^{19.5}$ eV and the corresponding plot for the signal efficiency against the background rejection.

The $X_{\max}$ distributions in figure 3.1 are showing a gaussian-like shape, with the photon sample reaching higher values in average going from around 610 g cm^{-2} up to above 1200 g cm^{-2} with a median of 841 g cm^{-2}. The $X_{\max}$ distribution for protons has a median at 756 g cm^{-2} and reaches values between 550 and 1150 g cm^{-2}. This is the expected case since photon-induced air-showers develop deeper in the atmosphere and thus have larger $X_{\max}$ values. In appendix A.2 and A.3 the $X_{\max}$ distributions for all energy bins are displayed. The lowest values for $X_{\max}$ for each photons and protons are originating on average in the lowest energy bin and go up with higher energies. This can also be seen looking at the mean values of the $X_{\max}$

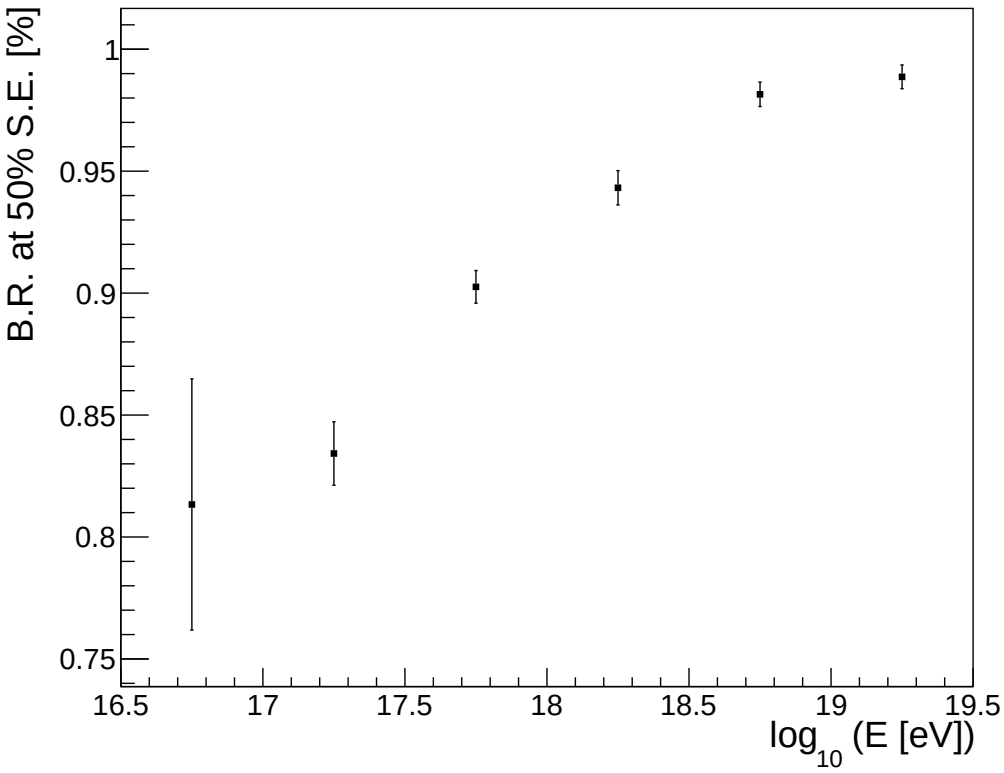

Figure 3.2: Development of the value of the background rejection at 50 % signal efficiency over energy for $X_{\max}$ (see appendix A.2 and A.3). This value has been computed for each energy bin as shown in table 3.1 and plotted over the respective mean value of that energy range. The uncertainties are the standard deviation of the distributions of a bootstrapping method, applied 10000 times in each energy bin. These plots can be seen in appendix A.4.

distribution for each energy bin in table A.1 in the appendix, which are getting larger at higher energies.

The merit factor for the distributions is $\eta = 0.889$ and does not indicate a "good" separation. Looking at the plot for signal efficiency against the background rejection in Fig. 3.1 a background rejection of 88.93 % at 50 % signal efficiency is gained. To estimate an uncertainty on the value a bootstrapping method was applied, where 10000 data sets were randomly put together from the original data set and evaluated in the same way. The standard deviation of this distribution serves as the uncertainty. The value for that is 0.4 % as read out of the distribution in figure A.1a in the appendix. The separation of the $X_{\max}$ observable changes for different energies. To show that, the signal efficiency versus background rejection is plotted for each energy bin. The $X_{\max}$ separation power is rising with energy due to the effects mentioned in chapter 1.4. In the two lowest energy bins from $10^{16.5}$ to $10^{17.5}$ eV it is even under 85 % background rejection at 50 % signal efficiency. The uncertainties in this energy bin are significantly bigger due to the small statistics. In the energy

bin from $10^{17.5}$ to 10^{18} eV it passes the 90 % mark.

3.2.2 S_b

While X_{max} is obtained solely by using the FD, the second observable S_b [69] is corresponding to SD measurements and is calculated by

$$S_b = \sum_{i=1}^{N_{stations}} S_i \times \left(\frac{r_i}{1000\,\mathrm{m}}\right)^b . \tag{3.4}$$

$N_{stations}$ is the number of stations used for calculating S_b and the parameter S_i denotes the signal measured at a station i with a distance r_i to the shower axis and is expressed in VEM. As in the photon paper for energies above 10^{18} eV [36] the value for b will be set to 4, which gives the best separation power like proposed in [70]. To fully max out the potential of the observable the logarithm of all values has been calculated. The S_4-distribution over the whole energy range from $10^{16.5}$ to $10^{19.5}$ eV and the corresponding background rejection plot can be seen in Fig.

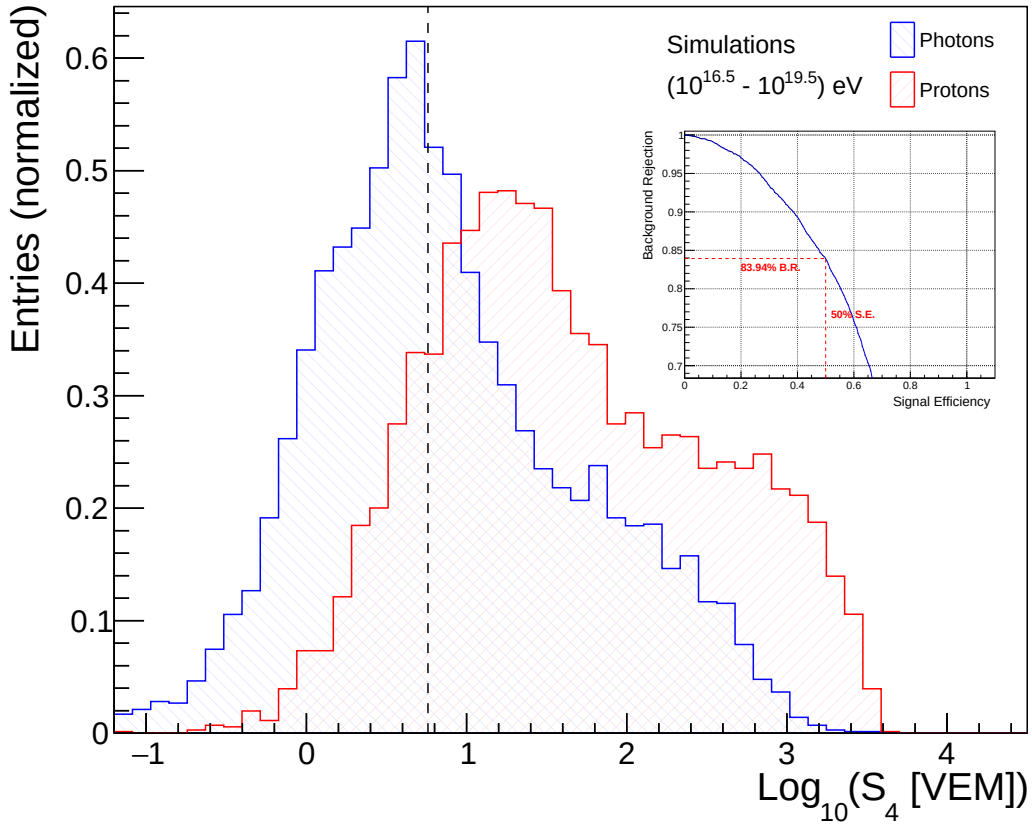

Figure 3.3: Distributions of the S_4 value for simulations of extensive air showers induced by photons (blue) and protons (red) with energies between $10^{16.5}$ and $10^{19.5}$ eV and the corresponding plot for the signal efficiency against the background rejection.

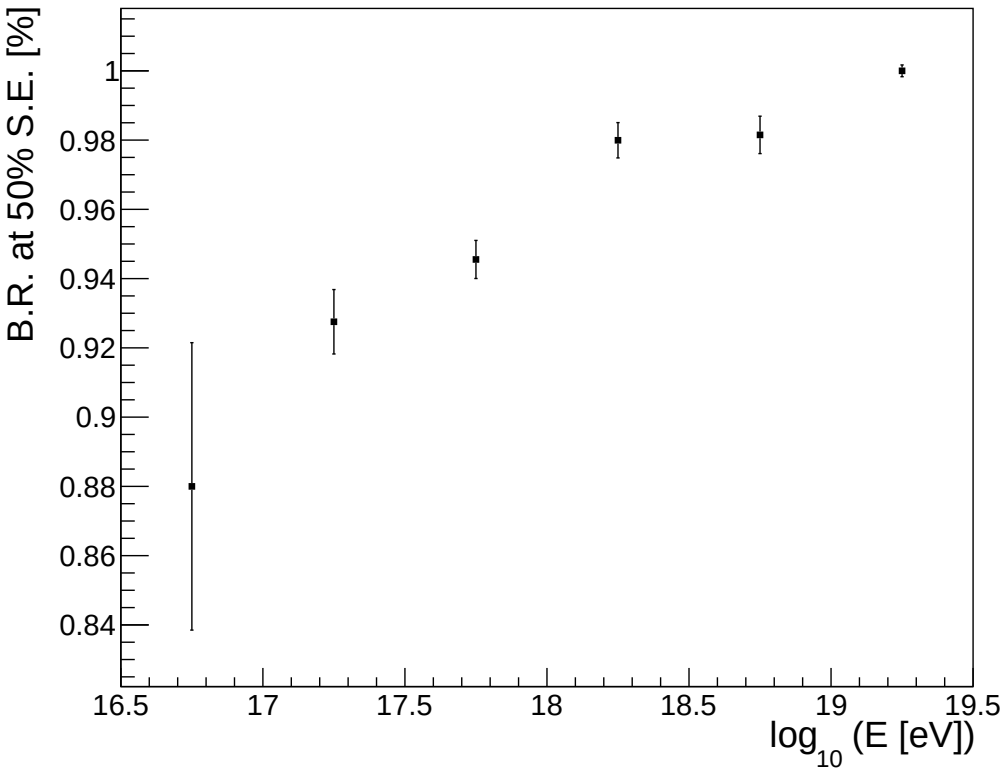

Figure 3.4: Development of the value of the background rejection at 50 % signal efficiency over energy for S_4 (see appendix A.5 and A.6). This value has been computed for each energy bin as shown in table 3.1 and plotted over the respective mean value of that energy range. The uncertainties are the standard deviation of the distributions of a bootstrapping method, applied 10000 times in each energy bin. These plots can be seen in appendix A.7.

3.3. Since, in contrast to the $X_{\max}$ distributions, the proton distribution provides a larger mean value of 1.512 VEM than the photon distribution with 0.759 VEM.
The plot for the signal efficiency against the background rejection has to be calculated with the less-than and greater-than signes in equations 3.1 and 3.2 switched. With ranges from -2 VEM to 3.4 VEM for photons and from -1.5 VEM to 3.6 VEM for protons both distributions have a significant overlap which is noticeable in the merit factor $\eta = 0.617$. The broad profile for both initial particles is due to the strong energy dependence of the observable S_4. While showing a more discrete structure in the single energy bins (see appendix A.5 and A.6) the distribution smears out looking at the whole energy range. The value for the background rejection at 50 % signal efficiency is still over 80 %, but doesn't reach the $X_{\max}$ equivalent. To make a statement about the uncertainty on that, the bootstrapping method was applied again. The resulting plot shows a standard deviation of 0.6 % (A.1b). In the plot in Fig. 3.4 a rise in the separation power of S_4 can be seen. It starts at around 88 % going up to 100 % in the last energy bin. As mentioned before, the observable shows

to be more powerful in smaller energy ranges since the values for the background rejection at 50 % signal efficiency is higher in each bin than for the whole data set.

3.2.3 N_{stations}

The third and last observable used to separate photon and proton events is the number of triggered stations used in S_4 called N_{stations}. What stands out with this variable in contrast to the two mentioned before, is the integer character of N_{stations}. The distribution of the values as well as the plot for the signal efficiency against the background rejection can be seen in Fig. 3.5.

The distribution shows in the mean higher values for protons ($\mu = 9$) than for photons ($\mu = 5$) which is the expected case, since hadronic showers have a broader lateral profile than the photon induced electromagnetic showers. The merit factor turns out to be the lowest of the three observables with $\eta = 0.527$. The background rejection at 50 % signal efficiency is 88.71 % with an uncertainty of 0.3 % (see A.1c) and is comparable to the other observables. Another thing to mention is that the

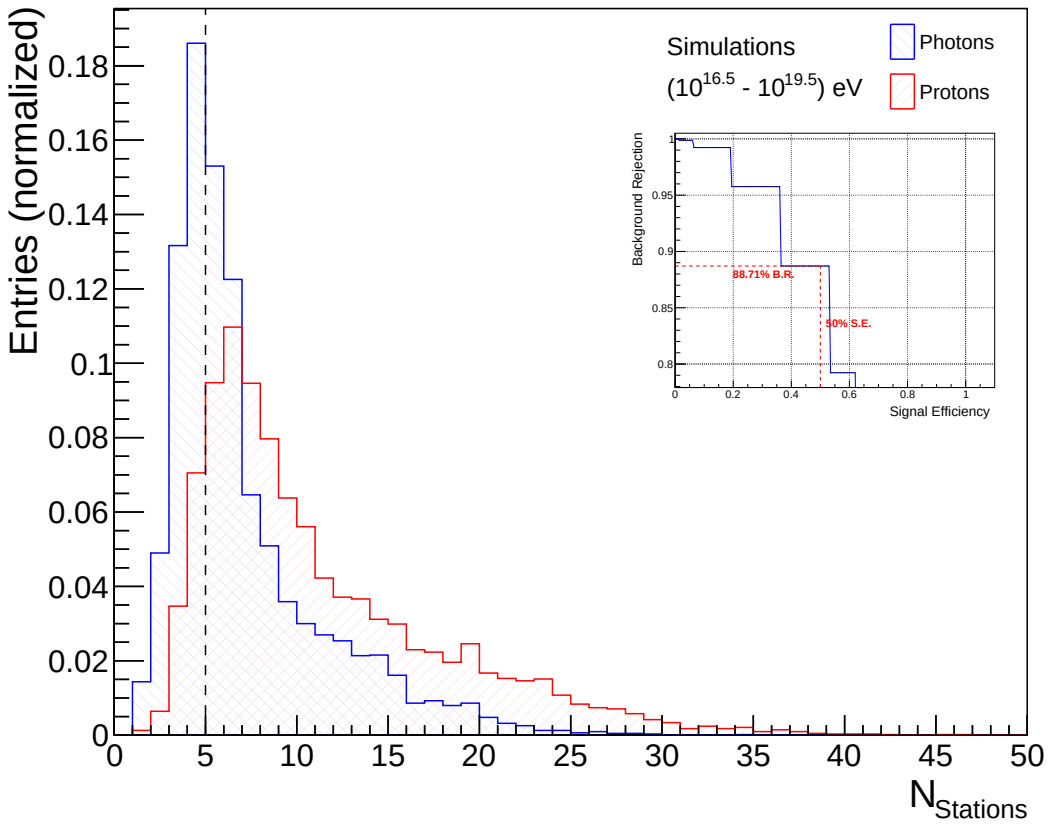

Figure 3.5: Distributions of the N_{stations} value for simulations of extensive air showers induced by photons (blue) and protons (red) with energies between $10^{16.5}$ and $10^{19.5}$ eV and the corresponding plot for the signal efficiency against the background rejection.

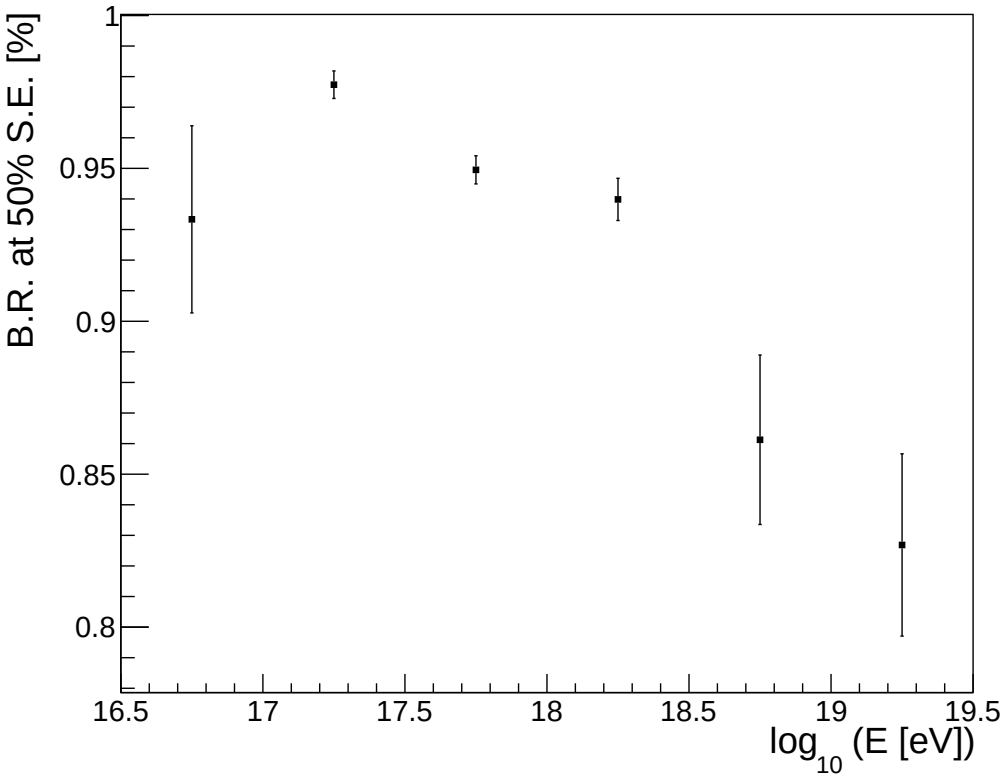

Figure 3.6: Development of the value of the background rejection at 50 % signal efficiency over energy for N_{stations} (see appendix A.8 and A.9). This value has been computed for each energy bin as shown in table 3.1 and plotted over the respective mean value of that energy range. The uncertainties are the standard deviation of the distributions of a bootstrapping method, applied 10000 times in each energy bin. These plots can be seen in appendix A.10.

background rejection plot also shows the discreteness of the observable N_{stations} since it is decreasing stepwise in contrast to the flatter curves in the other two observables. Fig. 3.6 shows the development of the value for the background rejection at 50 % signal efficiency. After a short rise, the separation power decreases under 90 %. Also large uncertainties can be seen in some bins. While for the energy bin with the lowest energies a large uncertainty is expected due to the lack of statistics, in the higher energetic bins such big uncertainties are rather unexpected. The cause for this is the discreteness of the observable. In Fig. 3.7a the result of the bootstrapping can be seen for the showers with energies between $10^{18.5}$ and 10^{19} eV. In contrast to the other bootstrapping distributions (see appendix A.10) this one has two maxima and with that a far bigger standard deviation. The reason for this is the median of the N_{stations} values, which is used for the calculation of the value for the background rejection at 50 % signal efficiency. Figure 3.7b shows an example of a plot for the signal efficiency against the background rejection. Only a small deviation in the values of N_{stations} would change the median and since N_{stations} is a discrete observable a big

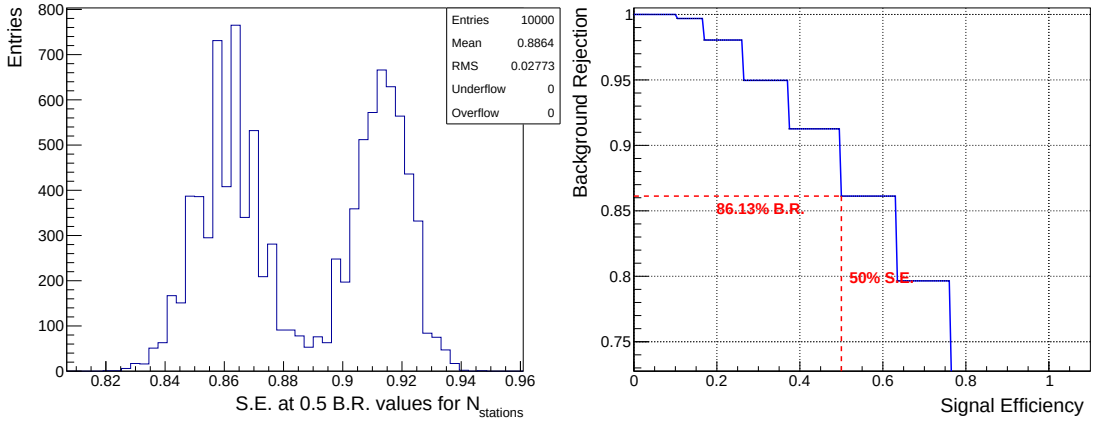

(a) (b)

Figure 3.7: (a) Bootstrapping and (b) the plot for the signal efficiency against the background rejection for the N_{stations} value of extensive air shower simulations with energies of the primary particle between $10^{18.5}$ and 10^{19} eV.

difference in background rejection would be achieved. In this example the median varies between 4 and 5 and so the background rejection has two maxima at around 86 % and 91 %. This is a huge downside of the N_{stations} observable on it's own, but it is still a useful observable when it is used in combination with the other two.

3.2.4 Correlation between the Observables

In the next step the observables X_{max}, S_4 and N_{stations} will be tested on their correlation. In each case two observable distributions have been plotted as scatter plots, which can be seen in Fig. 3.8. The combination of the observables X_{max} and S_4 in Fig.3.8a shows no clear correlation between each other. This is expected since the two observables depend on different properties of the shower. X_{max} depends on the longitudinal profile and S_4 on the lateral profile of the air shower. The distributions are also showing a rather good separation which is increasing with energy. Basically the same is true for the combination of X_{max} and N_{stations} in Fig.3.8b although the separation seems to be not as strong as in the first scatter plot. In contrast to that the distributions in Fig. 3.8c are hardly separated and show a clear correlation since S_4 and N_{stations} are both obtained by SD measurements.

Table 3.3 shows the Pearson correlation factors for the histograms. The values can range from -1 to 1, while values near to 1 show a strong correlation and those near to -1 a strong anti-correlation. If the values are around 0 there is no correlation at all. The correlation factors support the observations made before. While the correlation factor between S_4 and N_{stations} is clearly heading towards 1, the ones for the other two combinations are much below that while still showing some correlation. It is to mention that the correlation factors for the combinations of X_{max} with S_4 as well

as with N_{stations} are having a much larger correlation factor for photons than for protons.

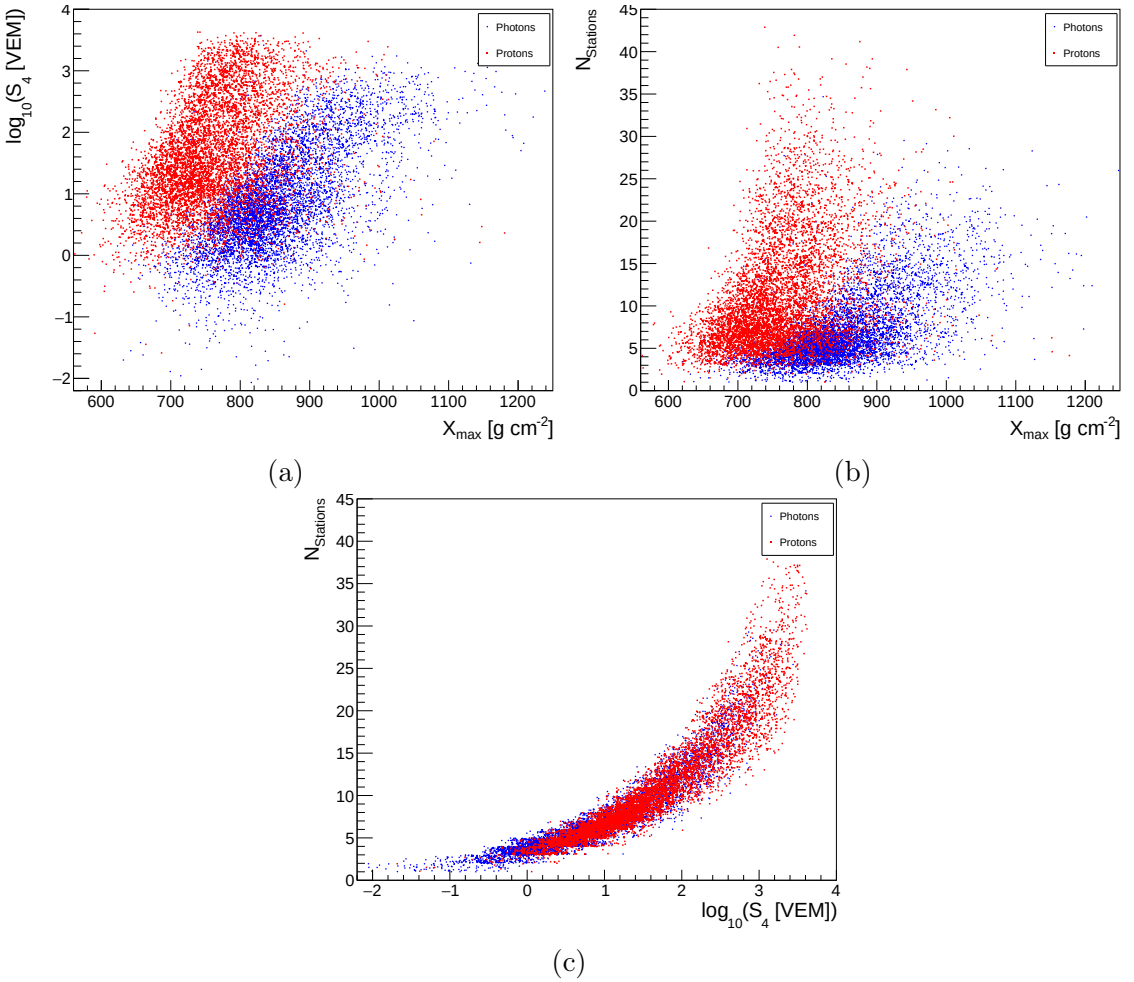

Figure 3.8: Correlation plots for (a) X_{max} vs. S_4, (b) X_{max} vs. N_{stations} and (c) S_4 vs. N_{stations} for air shower simulations with energies of the primary particle of $10^{16.5}$ to $10^{19.5}$ eV. The blue dots are for initial photons, the red ones are for initial protons.

Observables	Correlation coefficients	
	Photons	Protons
X_{max} & S_4	0.641	0.383
X_{max} & N_{stations}	0.631	0.364
S_4 & N_{stations}	0.908	0.913

Table 3.3: Values of the correlation factors of photons and protons for each combination of observables as seen in Figure 3.8.

3.3 Multivariate Analysis

A combination of the observables is a common way to gain more separation power. All three observables will be combined with a multivariate analysis (MVA). In this case the TMVA package [71] is used, which is integrated in the ROOT framework [72]. A MVA has to be trained with a set of known events, such that it knows the properties of a signal and a background-event.

3.3.1 BDT Description

The MVA technique used in this work is the Boosted Decision Trees (BDT) method. It works basically with binary decision trees in a structure as illustrated in Fig. 3.9. A tree is created via a recursive process using the trainings data set with known classification (signal "S" or background "B"). For every step in the tree the attribute x_i with the best separation result for signal or background is chosen and the tree is split respectively with a cut criterion c_i. Now this step is repeated until the data subset has only data of one classification. In this process an attribute x_i can be chosen multiple times or not at all.
To increase the effectivity multiple decision trees are formed by reweighting the sample used for the training. Now the so called "forest" of decision trees is averaged to form a single classifier. This process of boosting is done to increase the stability of the tree with respect to fluctuations in the trainings sample.
This technique is, since it can be visualized by a two-dimensional tree structure, similar to rectangular cuts. But while those are only allowing to split the phase space into one hypercube, the BDT method is able to form many hypercubes to classify the event into either "background-like" or "signal-like". [73]

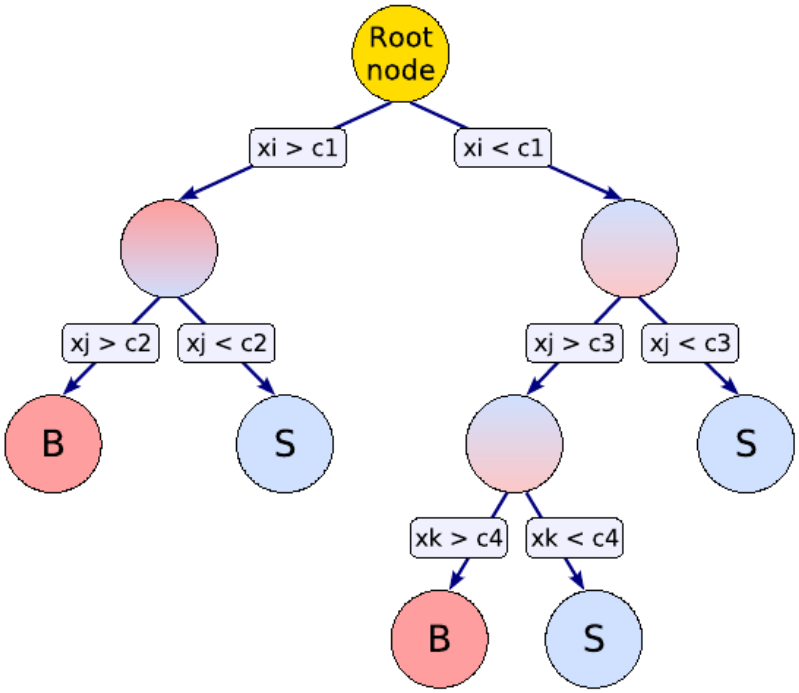

Figure 3.9: An illustration of a decision tree as it is used in the BDT method [73].

3.3.2 Reweighting of Data sets

The amount of simulations used for this analysis is, as seen in table 3.1, not the same in the different energy bins. Also it is created with an E^{-1} energy spectrum, but since the photon energy spectrum is not known it is also necessary to perform the analysis with different power laws. To take account of these two problems a weight is assigned to each shower at a given energy.
The final weights ω_i will be a combination of two weights:

$$\omega_i = \omega_{\text{glob}} \times \omega_{\text{ind}} \,. \tag{3.5}$$

The first one is a global weight ω_{glob} that takes care of the different statistics in each energy bin. As a default value the bin-content of the bin with showers of energies between $10^{17.5}$ and 10^{18} eV is used, since it has an average number of showers and the weights for the others do not need to be too big or small. After assigning a global weight to each energy bin, a weight for each individual energy ω_{ind} is required to achieve a general E^{Γ} energy spectrum. As an anchor point the energy $10^{17.7}$ eV is chosen, which will have an individual weight of 1. Since the data was already produced with an E^{-1} spectrum it is sufficient to multiply each energy again with $E^{(\Gamma+1)}$. The formula for the individual weight for an energy E_i is now

$$\omega_{\text{ind}} = \left(\frac{10^{17.7}\,\text{eV}}{E_i} \right)^{-(\Gamma+1)} . \tag{3.6}$$

A common choice of the power law is an E^{-2} energy spectrum, so the formula for the final weight would be

$$\omega_i = \frac{n_{\text{default}}}{n_{\text{bin}_i}} \times \frac{10^{17.7}\,\text{eV}}{E_i} \tag{3.7}$$

where n_{default} is the bin-content of the chosen default bin and n_{bin_i} is the bin-content of each bin. In Fig. 3.10 the simulated data for photons and protons is shown before and after the reweighting. In section 3.5.2 the effect of other values for Γ will be discussed.

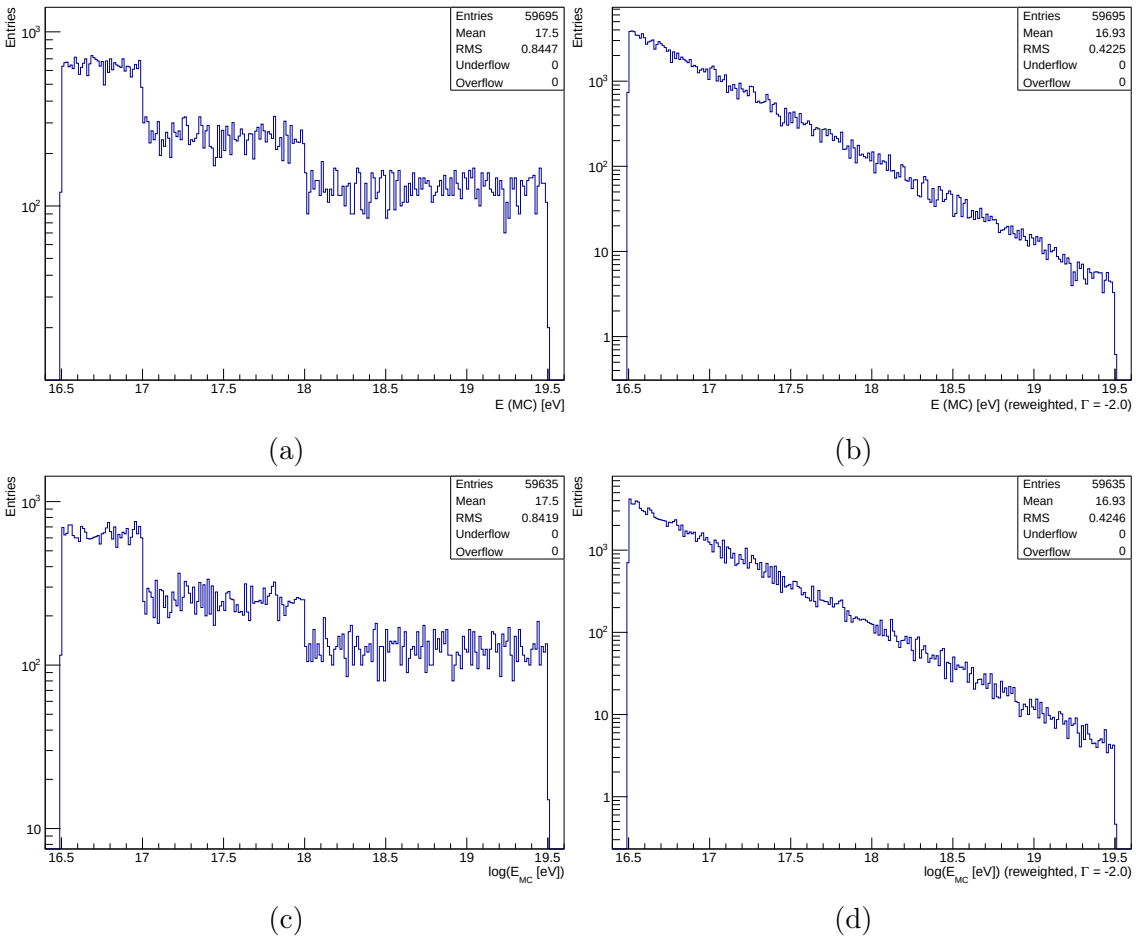

Figure 3.10: The number of simulations for (a) photon and (c) proton induced air showers without reweighting and the number of simulations for (b) photon and (d) proton induced air showers multiplied by weights calculated with equation 3.7.

3.3.3 Performance of the MVA

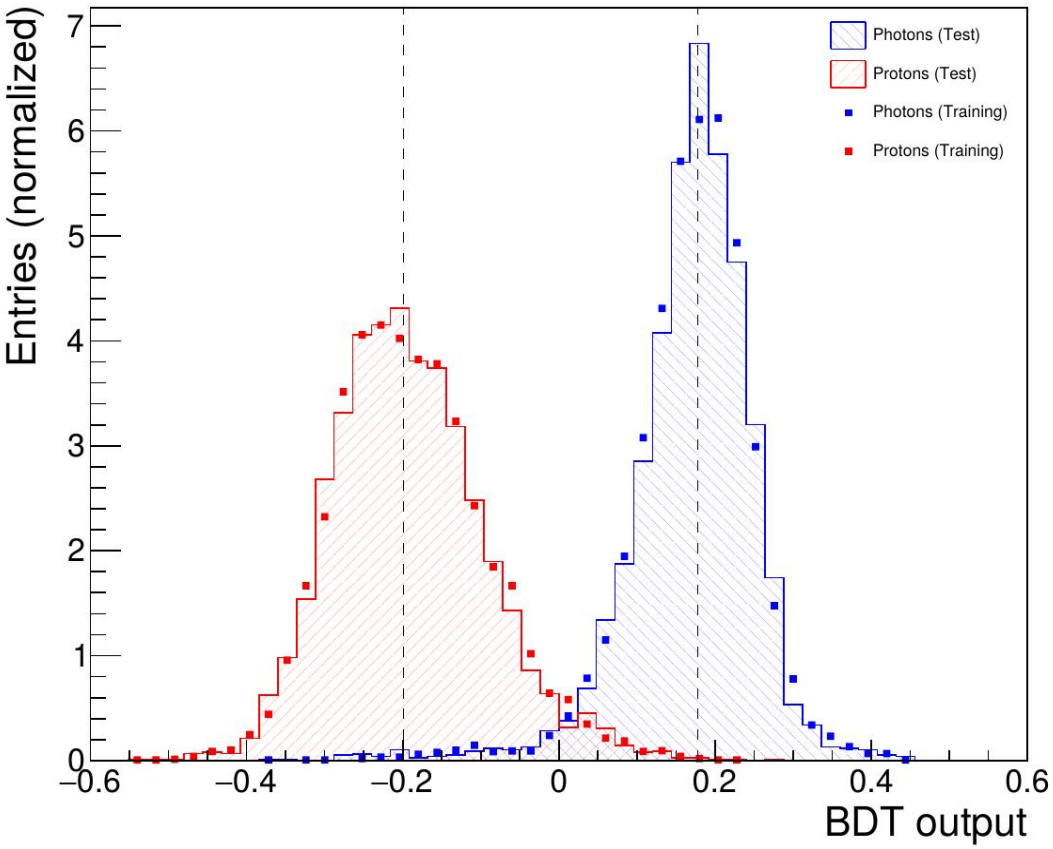

Figure 3.11: The output values of the MVA using a BDT method for the energy range from $10^{16.5}$ to $10^{19.5}$ eV, trained with an independent sample of the same energy range. The blue histograms are for initial photons, the red ones are for initial protons. The points indicate the MVA output for the data set used for training the MVA and the dashed lines refer to the median of each distribution.

The input variables for the multivariate analysis in this work will be the atmospheric depth at the shower maximum $X_{\max}$, the variable S_4 and the corresponding number of triggered SD stations N_{stations}. To be independent of the energy and zenith angle these two observables are also used additionally in the MVA.
As described in section 3.3 it is necessary to train the MVA with simulations. To do so randomly 2/3 of the each simulated data set were taken and used to let TMVA build the Boosted Decision Trees. The remaining 1/3 of the simulations is then used to test the trained MVA. The splitting of the sample is important since it has to be avoided that the MVA gets tested with the same set as it was trained with. While the training was always performed with simulations of the whole energy range, the testing was performed for all energies as well as bin-wise. Figure 3.11 shows the BDT output values for the reweighted data from $10^{16.5}$ to $10^{19.5}$ eV as a histogram. The

proton distribution has a broader profile than the one for photons and has mainly negative values down to −0.55 with a median at −0.199. The distribution of the BDT values for photons is on the other hand much sharper with values around the median of 0.178 although it has a significant tail reaching into the negative range. The overlap is compared to the distributions for the single observables in 3.1, 3.3 and 3.5 smaller, which can be seen in the merit factor $\eta = 2.882$. The background rejection has also been plotted against the signal efficiency and can be seen in figure 3.12.

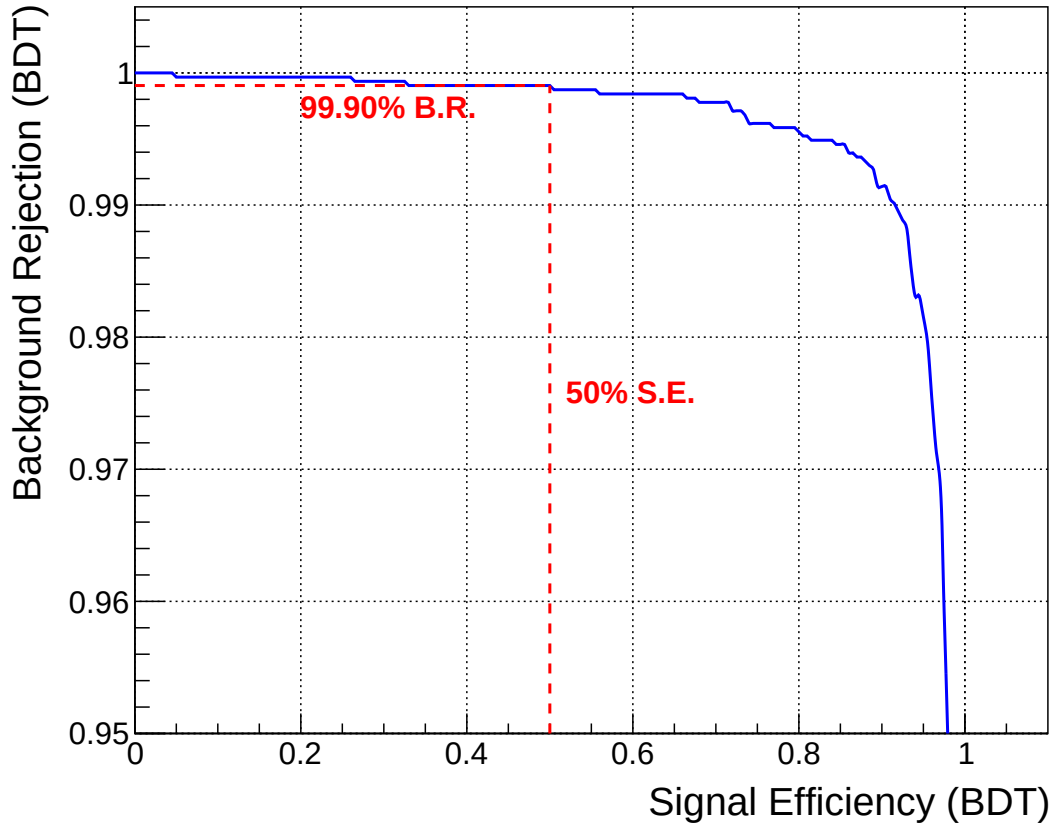

Figure 3.12: Background rejection vs. Signal efficiency of the BDT values for the energy range from $10^{16.5}$ to $10^{19.5}$ eV, trained with an independent sample of the same energy range.

The overall background rejection at 50 % signal efficiency is 99.90 % with an uncertainty of 0.06 %. This is a big improvement to the separation power of the observables on their own as mentioned in section 3.2. The graph in this plot declines stepwise rather than smoothly for small values of the signal efficiency. This is not an effect caused by the binning of the histogram, it is caused by single proton events having a larger BDT value than the photon median. When the analysis is applied to data, the median of the simulated photon BDT sample is taken as an a priori candidate cut, meaning that particles with a higher BDT value than that are considered to be photons. In these proton simulations exactly 3 events would be

reconstructed as photons.
The plots in Fig. 3.13 show the same as above, but separated in energy bins. The training of the MVA was performed with the whole data set since this will be also the case when the analysis is applied to real data. For the same reason the median plotted here is the median of the BDT distribution of the whole energy range. For the distributions of the data in the smaller energy ranges the signal efficiency against background rejection plots can be seen in Fig. 3.14.
As mentioned before there are three proton events which have bigger a BDT value than the photon BDT median. The plots in 3.13 and 3.14 can be used to investigate at which energies these most photon like proton events are produced. As expected two of the events are belonging to the lowest energy bin from $10^{16.5}$ to 10^{17} eV. This is even more significant taking the low number of 26 fully reconstructed proton events into account, which lets the graph drop down to 92.31 % background rejection at 50 % signal efficiency. The other event is in the bin from $10^{17.5}$ to 10^{18} eV.
In the lower energetic bins the detector will not be able to reconstruct enough events properly, which causes a big lack of statistics. For this reason the events with energies in that region will be not taken into account anymore. Image 3.15 shows the distribution of the reconstructed photon energy on a logarithmic scale. The point from where the distribution behaves like the expected power-law and is not influenced by the acceptance of the detector anymore is at around 2×10^{17} eV.
In the following the before mentioned analysis steps will be performed for showers above that energy. The BDT is still trained with all of the events. Fig. 3.16a and 3.16b show the outcome of the MVA applied to the reduced data set with events of energies above 2×10^{17} eV. The value of the background rejection at 50 % signal efficiency has changed to 99.97 %. This is expected since two of the three events which had a BDT value above the photon median were in the lowest energy bin which is now not taken into account anymore. The only event still being bigger than the photon median is the one of the third energy bin from $10^{17.5}$ to 10^{18} eV.

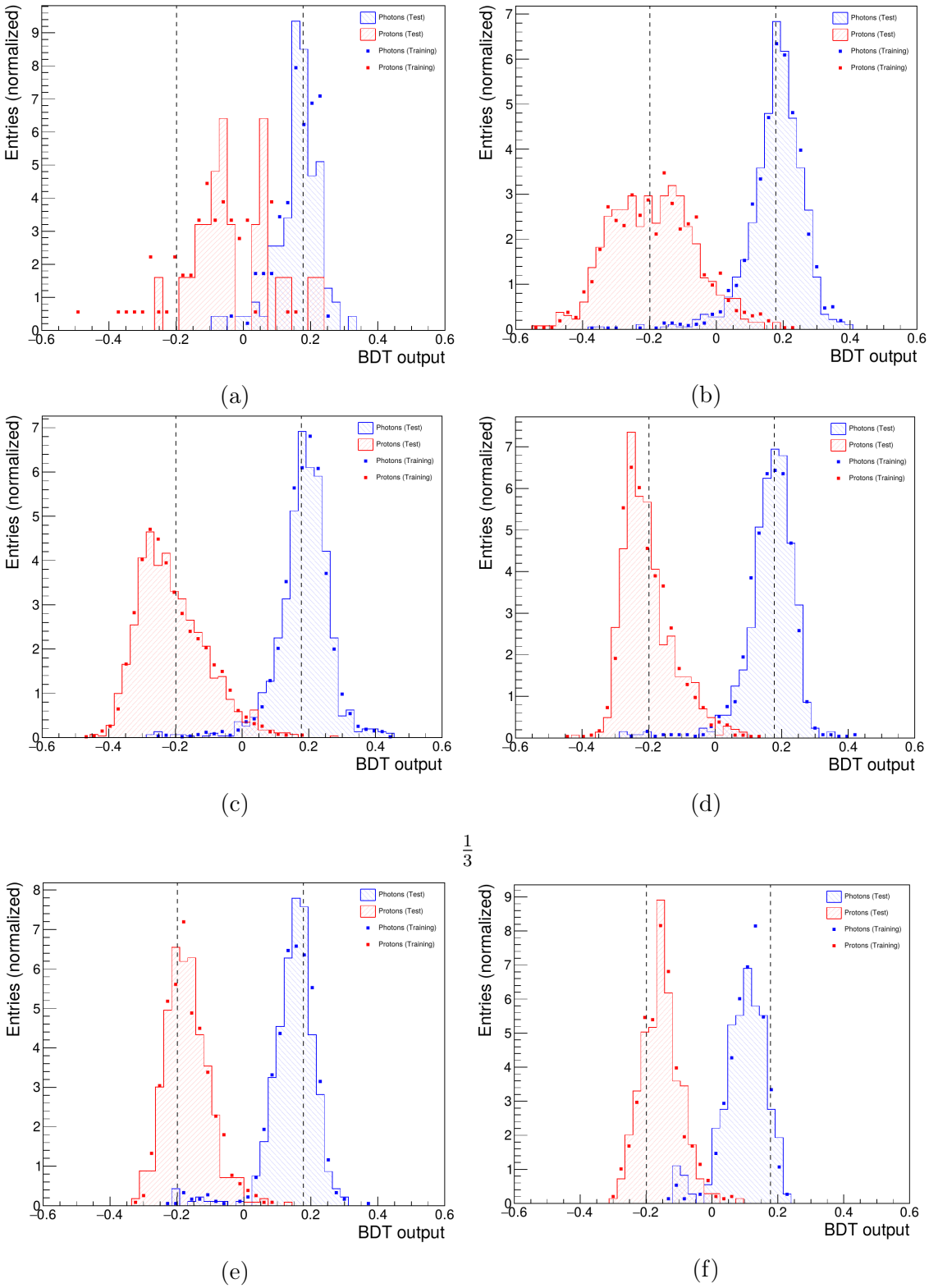

Figure 3.13: The MVA output using a BDT method for primary photons (blue) and protons (red) in the energy range from $10^{16.5}$ to 10^{17} eV (a), 10^{17} to $10^{17.5}$ eV (b), from $10^{17.5}$ to 10^{18} eV N_{stations} (c), from 10^{18} to $10^{18.5}$ eV (d), from $10^{18.5}$ to 10^{19} eV (e) and from 10^{19} to $10^{19.5}$ eV (f). The blue histograms are for initial photons, the red ones are for initial protons. The dashed lines indicate the data set used for training the MVA. The median is the one for the whole data set from $10^{16.5}$ to $10^{19.5}$ eV which was also used for the training.

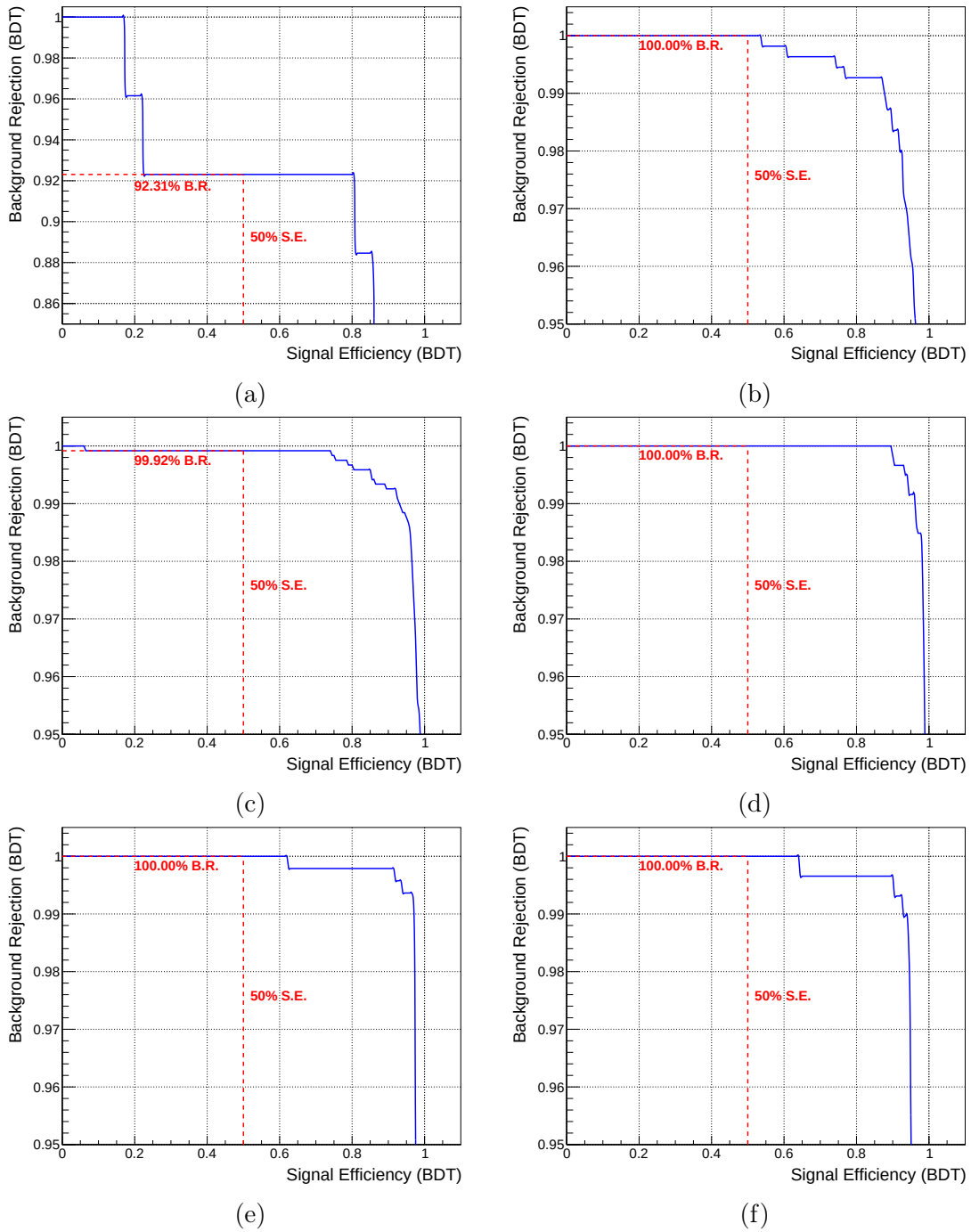

Figure 3.14: Background rejection vs. Signal efficiency of the BDT values for the energy range from $10^{16.5}$ to 10^{17} eV (a), 10^{17} to $10^{17.5}$ eV (b), from $10^{17.5}$ to 10^{18} eV N_{stations} (c), from 10^{18} to $10^{18.5}$ eV (d), from $10^{18.5}$ to 10^{19} eV (e) and from 10^{19} to $10^{19.5}$ eV (f). The MVA has been trained with events of the whole energy range from $10^{16.5}$ to $10^{19.5}$ eV.

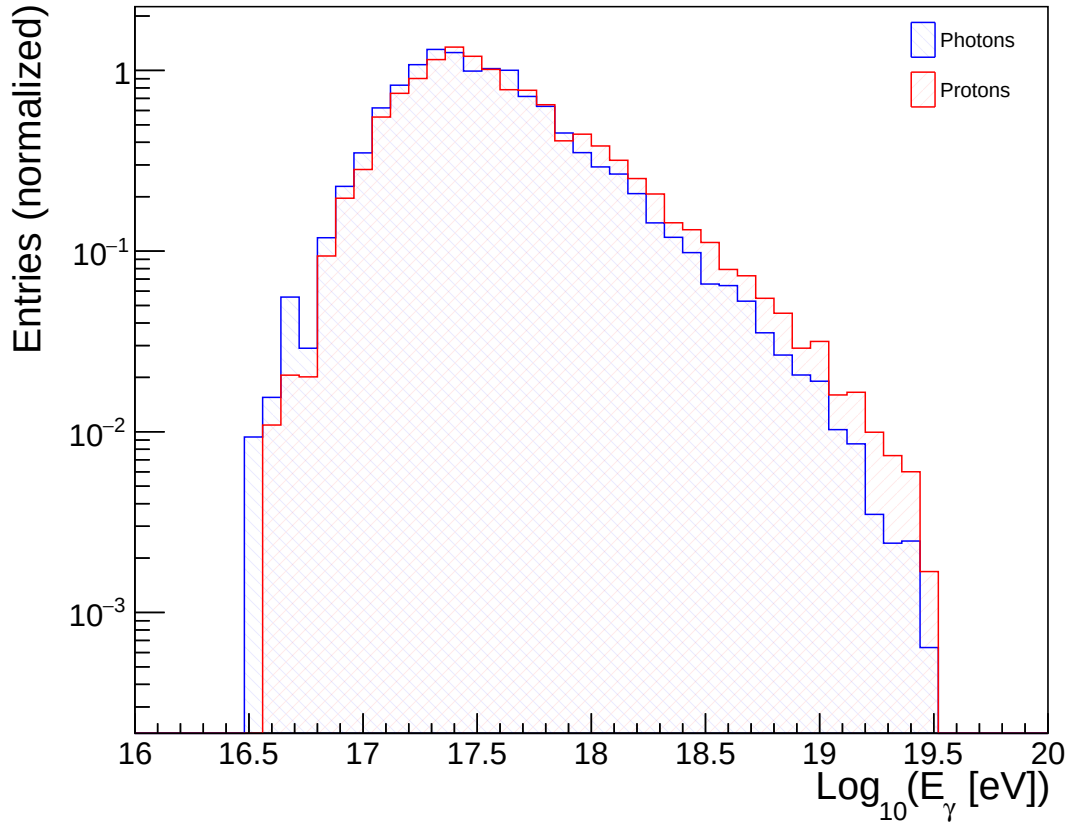

Figure 3.15: Distribution of the reconstructed photon energy for all events in the energy range from $10^{16.5}$ to $10^{19.5}$ eV for photons (blue) and protons (red).

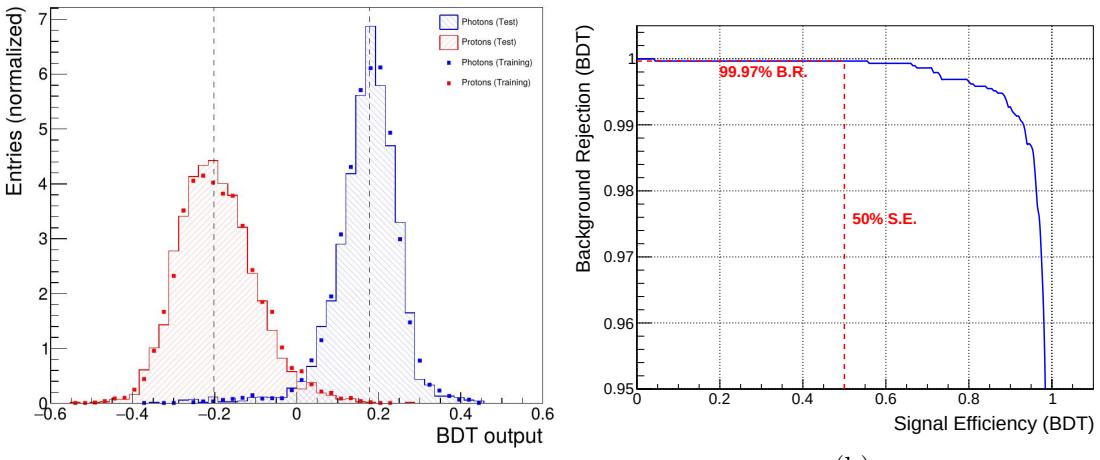

(a) (b)

Figure 3.16: The BDT values (a) and the plot for the signal efficiency against the background rejection (b) for energies of the primary particle from $10^{17.2}$ to $10^{19.5}$ eV, trained with an independent sample of the energy range from $10^{16.5}$ to $10^{19.5}$ eV.

3.4 Estimation of Flux Limits

The current limits on the integrated photon flux were introduced in section 1.4. After applying this analysis to real data, it may be possible to also set flux limits for the energy range between 10^{17} and 10^{18} eV. In the following an estimation of these limits will be calculated with the formula

$$\Phi_{\text{U.L.}}^{95\%\text{ C.L.}}(E > E_0) = \frac{N_{\text{cand.}}^{95\%\text{ C.L.}}}{\mathcal{E}(E > E_0) \,|\, E_\gamma^{-\Gamma})} \tag{3.8}$$

using the integrated hybrid exposure $\mathcal{E}$. The index 95 denotes the Feldmann-Cousins confidence level, which is 95 %. With the assumption of no candidate events, the number of candidates at 95 % confidence level $N^{95\%}$ would be 3.

3.4.1 Exposure Calculation

The formula which is used to calculate the integrated hybrid exposure is given by

$$\mathcal{E}(E > E_0) = \frac{1}{c_E} \int_E \int_T \int_S \int_\Omega E^{-\Gamma} \epsilon(E, t, \Theta, \varphi, x, y) \, \mathrm{d}S \, \mathrm{d}t \, \mathrm{d}E \, \mathrm{d}\Omega \tag{3.9}$$

with the efficiency ϵ, the energy E, the time of data taking T, the surface area S, the overall angle Ω and the normalization factor being

$$c_E = \int E^{-\Gamma} \mathrm{d}E \,. \tag{3.10}$$

As mentioned in section 3.3.2 the exponent of the energy spectrum will be taken as $\Gamma = 2$. Another assumption is the efficiency to be independent of the time t, the zenith angle Θ and the azimuth angle φ as well as the area S. This shortens the equation down to

$$\mathcal{E}(E > E_0) = \frac{1}{c_E} \int_E E^{-2} \epsilon(E) \mathrm{d}E \int_T \mathrm{d}t \int_S \mathrm{d}S \int_\Omega \mathrm{d}\Omega \,. \tag{3.11}$$

The three latter integrations can now easily be calculated:

The time T is the hybrid ontime of 13 % of the whole time of taking data (see section 2.2) with the 750 m array from 01.06.2010 to 31.12.2015, which would be 5.583 years. This gives

$$\int_T \mathrm{d}t = T = 0.13 \times \int_{01.06.2010}^{31.12.2015} \mathrm{d}t = 0.13 \times 5.583\,\mathrm{yr} = 0.726\,\mathrm{yr}. \tag{3.12}$$

The area S is the whole area of the 750 m array. The calculation of the area (as

seen in Fig.2.8) can easily be made by calculating the area of one triangle of stations in the array, which is $0.2436\,\mathrm{km}^2$, and multiplying it with the number of triangles. With 112 triangles the solution to this part of the integration would be

$$\int_S \mathrm{d}S = S = 112 \times 0.2436\,\mathrm{km}^2 = 27.28\,\mathrm{km}^2\,. \tag{3.13}$$

It is to mention that this is an optimistic assumption since not all stations of the 750 m array were continuously in use in the time of measuring. Some stations may have been still under construction in the beginning or had some technical defects. The azimuth coverage is 2π and the zenith angles are below 60°, which gives us the overall angle integration to

$$\int_\Omega = \Omega = 2\pi \times 0.5 = \pi\,\mathrm{sr}\,. \tag{3.14}$$

The efficiency ϵ is calculated for each energy bin as the fraction of the well reconstructed ("good") events and all events. Table 3.4 shows the values.

Energy bin $[\log_{10}(E[\mathrm{eV}])]$	$\langle E_{MC}\rangle$ $\log_{10}(E[\mathrm{eV}])]$	good events	events	ϵ
16.5-17.0	8.128×10^{16}	292	25000	0.0117
17.0-17.5	2.089×10^{17}	2254	10000	0.2254
17.5-18.0	5.495×10^{17}	3737	10000	0.3737
18.0-18.5	1.698×10^{18}	1583	5000	0.3166
18.5-19.0	5.370×10^{18}	1139	5000	0.2278
19.0-19.5	1.514×10^{19}	463	5000	0.0926

Table 3.4: Values to calculate the efficiency ϵ for each energy bin.

To integrate the efficiency over the energy, it has to be linearly interpolated between the mean Monte Carlo energy $\langle E_{\mathrm{MC}}\rangle$ of each energy bin

$$\epsilon_i(E) = a_i \times E_{\mathrm{MC}_i} + b_i\,. \tag{3.15}$$

Image 3.17 shows a sketch of how the interpolation will be performed.

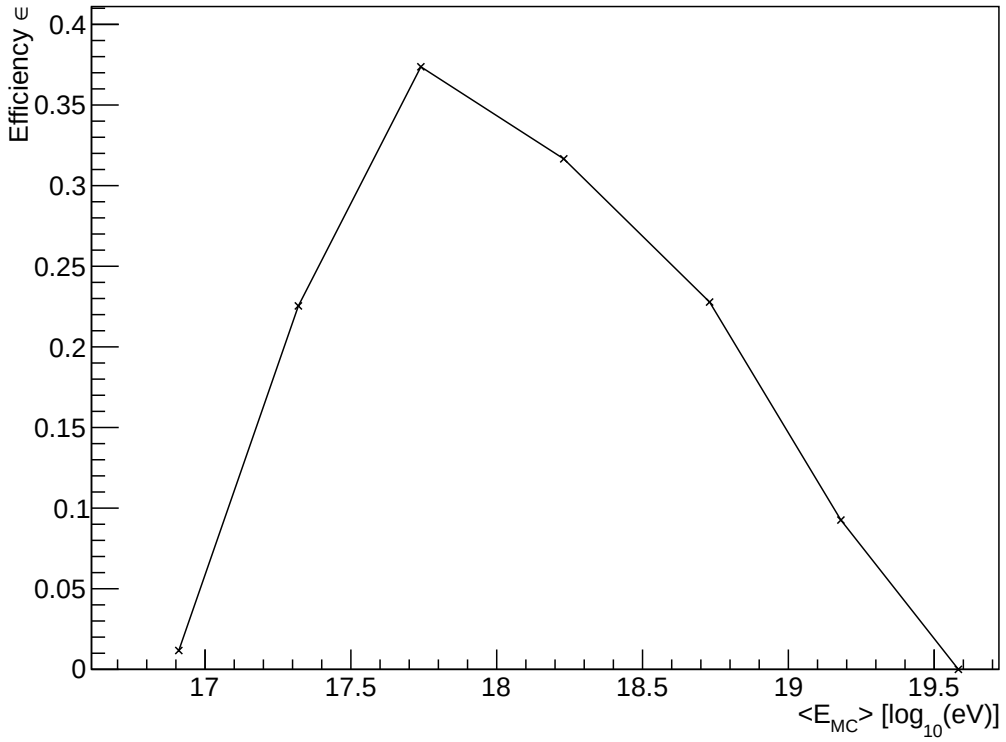

Figure 3.17: Plot of the calculated efficiency over the mean Monte Carlo energy value of each energy bin and the linearly interpolated functions (see 3.15) between the points.

The parameters in 3.15 can now be computed in the standard way with the difference quotient. They are summed up in table 3.5. It is to mention that every value for a is multiplied by a factor of 0.5, which is taking account of the photon candidate cut where half of the photon events are a priori not counted (see section 3.3.3).

Lower limit	Upper limit				
8.128×10^{16}	2.089×10^{17}	$a_1 =$	8.372×10^{19}	$b_1 =$	-0.056
2.089×10^{17}	5.495×10^{17}	$a_2 =$	2.177×10^{19}	$b_2 =$	0.179
5.495×10^{17}	1.698×10^{18}	$a_3 =$	-2.485×10^{20}	$b_3 =$	0.387
1.698×10^{18}	5.370×10^{18}	$a_4 =$	-1.209×10^{20}	$b_4 =$	0.337
5.370×10^{18}	1.514×10^{19}	$a_5 =$	-6.922×10^{21}	$b_5 =$	0.265

Table 3.5: Values of the linear interpolation as described in formula 3.15 to calculate the integrated hybrid exposure $\mathcal{E}$.

Since the integration is always performed from a threshold energy E_0 to infinity a sufficient upper limit is needed. As an estimate serves the root value of the linear extrapolation of the exposure of the last energy bin. This comes out to be $E_{lim} = 3,828 \times 10^{19}$. The chosen threshold energies are 2×10^{17} eV, 3×10^{17} eV, 5×10^{17} eV and 10^{18} eV, since they cover the aimed energy range. The integration of

the calculated exposure functions will be shown for the first threshold energy. For the remaining energies the integration will be performed analogously. The normalization factors derived for the different threshold energies with formula 3.10 can be found in table 3.6.

E_0 [eV]	c_E
2×10^{17}	5×10^{-18}
3×10^{17}	3.3×10^{-18}
5×10^{17}	2×10^{-18}
10^{18}	1×10^{-18}

Table 3.6: Values of the normalization factor for the integrated hybrid exposure for each threshold energy E_0, calculated with formula 3.10.

The integrations will be performed from the threshold energy to the next mean value of the Monte Carlo energy, using the function that was created for that energy range. For the first threshold energy of $2 \times 10^{17}\,\mathrm{eV}$, the upper integration limit is the mean Monte Carlo energy of the second energy bin 2.089×10^{17}, with the integral performed over the linear expression with a_1 and b_1. To this first integral the integrals over all remaining linear interpolations are added with the corresponding Monte Carlo energies as the limits, with the last integral reaching up to E_{lim}. All together the calculation looks like this:

$$\begin{aligned}\mathcal{E}(E > 2 \times 10^{17}\,\mathrm{eV}) =& C \times \left(\int_{2\times10^{17}}^{2.089\times10^{17}} \epsilon_1(E)\,\mathrm{d}E + \int_{2.089\times10^{17}}^{5.495\times10^{17}} \epsilon_2(E)\,\mathrm{d}E \right. \\ &\left. + \int_{5.495\times10^{17}}^{1.698\times10^{18}} \epsilon_3(E)\,\mathrm{d}E + \int_{1.698\times10^{18}}^{5.370\times10^{18}} \epsilon_4(E)\,\mathrm{d}E + \int_{5.370\times10^{18}}^{3,828\times10^{19}} \epsilon_5(E)\,\mathrm{d}E \right).\end{aligned} \tag{3.16}$$

Multiplied with the integrals over constants discussed earlier and the normalization factor (here combined in the constant C), the result for this computation is $\mathcal{E}(E > 2 \times 10^{17}\,\mathrm{eV}) = 130.881\,\mathrm{km^2\,yr\,sr}$. For the other threshold energies the calculation was made analogously. The results for all different values can be seen in table 3.7.

E_0 [eV]	$\mathcal{E}$ [$\mathrm{km^2\,yr\,sr}$]
2×10^{17}	130.881
3×10^{17}	143.991
5×10^{17}	156.020
10^{18}	141.934

Table 3.7: Values of the estimate for the integrated hybrid exposure for each threshold energy E_0, calculated with formula 3.8.

3.4.2 Integrated Photon Flux

The last thing to do is using this value to calculate the integrated photon flux with equation 3.8. Table 3.8 shows the flux for each threshold energy E_0.

E_0 [eV]	Φ [$\mathrm{km^{-2}\,yr^{-1}\,sr^{-1}}$]
2×10^{17}	0.176
3×10^{17}	0.160
5×10^{17}	0.148
10^{18}	0.163

Table 3.8: Values of the estimate for the integrated hybrid exposure and flux of photons for each threshold energy E_0, calculated with formula 3.8.

In Fig. 3.18 the results for the estimation are plotted together with existing integrated photon flux limits. The results are multiplied with a factor of 2 to not overestimate the analysis. Looking at the outcome of the previous photon analysis at the Pierre Auger Observatory for energies above 10^{18} eV, this work may be able to produce results in a similar order of magnitude. The existing limits in that energy range given by KASCADE-Grande [34] may be improved by two orders of magnitude.

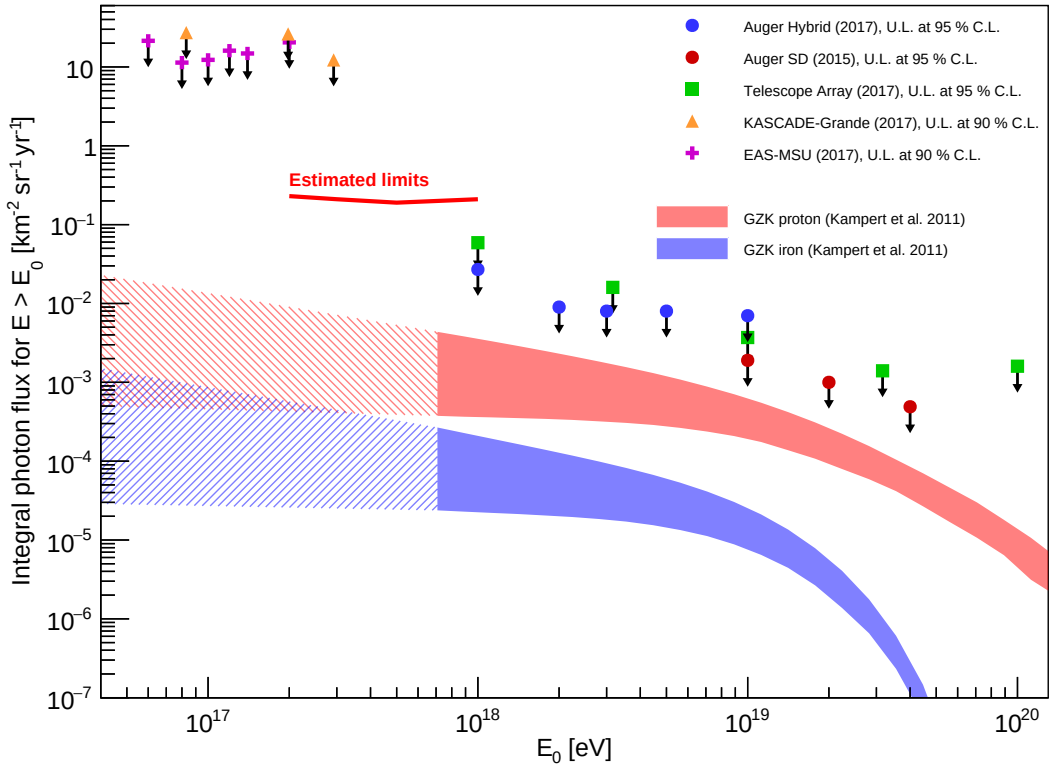

Figure 3.18: Estimated limits for the hybrid photon flux in the energy range from 2×10^{17} eV to 10^{18} eV, plotted together with existing photon flux limits of the Pierre Auger Observatory [36] [37], Telescope Array [38], Kascade-Grande [34] and EAS-MSU [35], as well as theoretical bands for GZK photons initiated by iron nuclei and protons calculated by Kampert [39]. The shaded areas are a linear extrapolation of the theoretical GZK bands.

3.5 Further Checks

It is important to check the analysis on consistency, but also if it performs as it does under slightly different conditions since not all parameters are fixed and the simulations always vary from real data.

3.5.1 Checking for a Bias in the Reconstructed Observables

At first the raw detector data has to be reconstructed in order to get the observables and subsequently to analyse them. In our case it is possible to check whether there is a mistake in the reconstruction chain by comparing the input configurations of the simulated CORSIKA showers with the reconstructed data of the detector simulations and to calculate the difference between them. The distribution should center around 0, with some events being over- and underestimated. In Fig. 3.19 such a bias plot is shown for the observables X_{max}, the energy E, the zenith angle Θ, the azimuth angle ϕ and the position of the shower core.
Especially in the X_{max} and the core position distribution have a shift to higher values. The mean value of the X_{max} histogram is around $5\,\mathrm{g\,cm^{-2}}$, but with a standard of deviation of around $20\,\mathrm{g\,cm^{-2}}$ this deviation is in an acceptable range. The same for the core position deviation, which has a mean value of about 20 m but a standard deviation of around a 100 m.

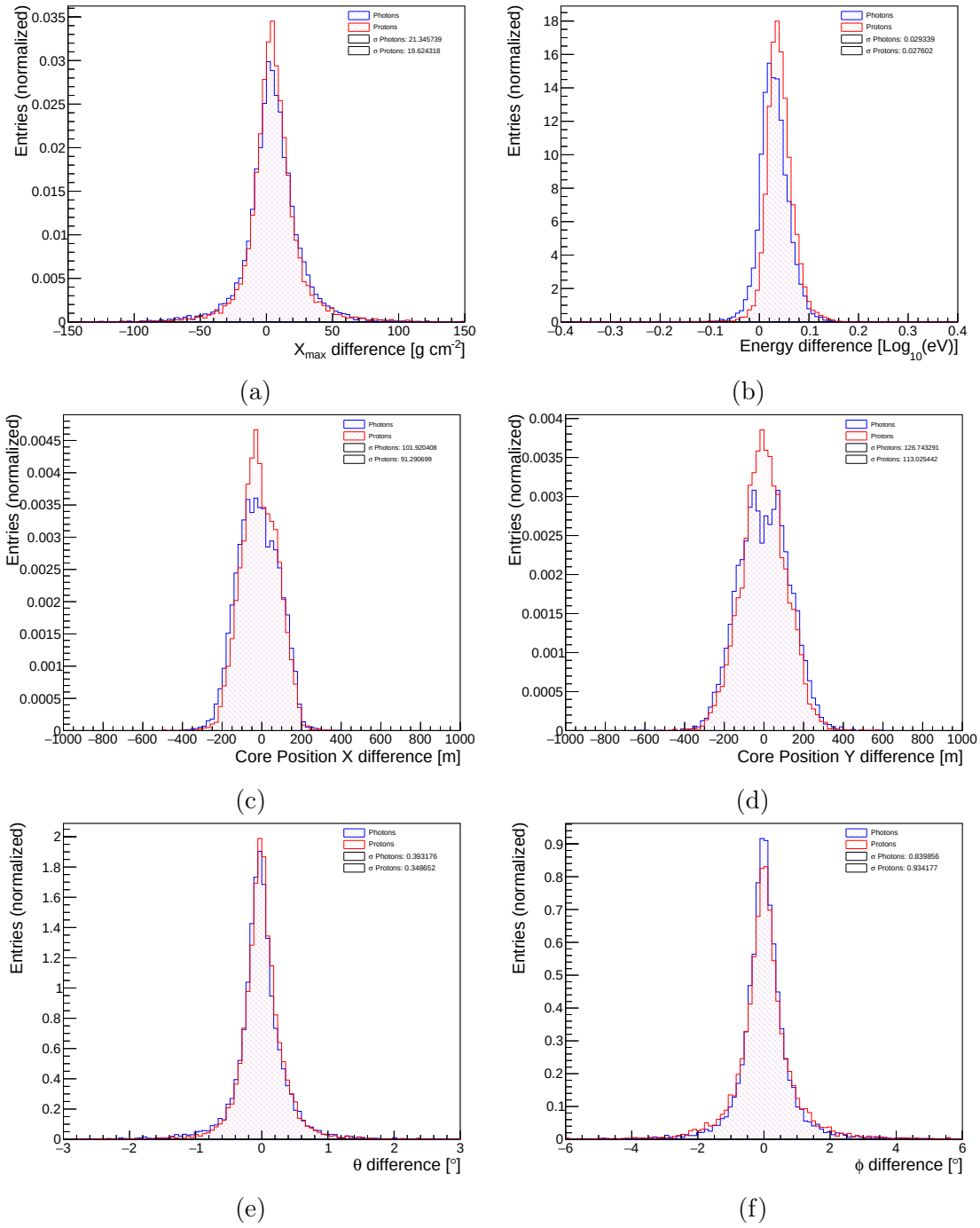

Figure 3.19: Distributions for the deviation of the reconstructed value from the initial Monte Carlo input. These histograms were made for $X_{\max}$ (a), the Energy (b), the shower core position (c), the zenith (d) and the azimuth angle (e).

3.5.2 Choosing a Different Γ

In section 3.3.2 the data has been reweighted to follow a power-law with an exponent of $\Gamma = -2$. This value is a common agreement, but other spectral indices should also be taken into account. To do so the data set has also been reweighted to get a spectrum with $\Gamma = -1$, $\Gamma = -1.5$, $\Gamma = -2.5$ and $\Gamma = -3$. After that, the analysis was performed in the same manner as before, giving us a value for the background rejection at 50 % signal efficiency. These values are plotted in figure 3.20.

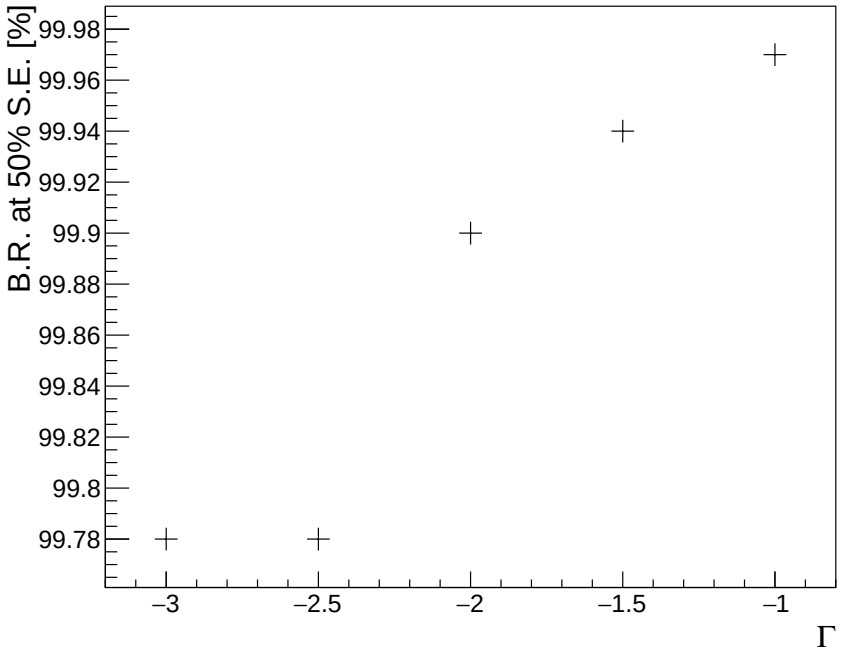

Figure 3.20: Results of the values for the background rejection at 50 % signal efficiency for different energy spectra of the photon simulations.

It shows an increase in separation power going to higher values of Γ. This is the expected case, since the separation power rises with energy (see figure 3.14) and with lower values of Γ these higher bins are more suppressed in their contribution to the separation. With the steepest energy spectrum of $\Gamma = -3$, the separation power gets to its minimal value of 99.78 % background rejection at 50 % signal efficiency.

4 Conclusion

4.1 Summary

In this work the results of an analysis to restrict the photon flux in the energy range between 10^{17} eV and 10^{18} eV were presented based on simulations. For this purpose 12000 photon and proton induced air showers were simulated with primary energies from $10^{16.5}$ eV to $10^{19.5}$ eV using CORSIKA. Each of these air showers was then processed five times in the $\overline{\text{Off}}\underline{\text{line}}$ framework to simulate the detector response of the 750 m array and the HEAT/HeCo telescopes which adds up to 60000 signal (photon) events and background (proton) events respectively. After a set of selection criteria was applied to the simulations roughly 15 % of the whole data set was usable. As observables to distinguish between photon and proton induced air showers the observables X_{max}, N_{stations} and S_4 were used. In a first step the separation power of each observable was tested. The distributions have been plotted for the whole energy range and the Merit factor and the background rejection at 50 % signal efficiency were calculated. The values are shown in table 4.1.

	Merit factor η	B.R. at 50 % S.E.
X_{max}	0.889	88.93
S_4	0.617	83.94
N_{stations}	0.527	88.71
BDT output	2.882	99.90

Table 4.1: Table of the results for the Merit factor and the background rejection at 50 % signal efficiency for the X_{max}, S_4 and N_{stations} distributions of air shower simulations with primary photons and protons with energies between $10^{16.5}$ eV and $10^{19.5}$ eV following an E^{-2} spectrum.

The observables were then combined in a multivariate analysis using the BDT method which was trained with 2/3 of the simulated events and tested with the remaining 1/3. The BDT output has also been plotted and evaluated like the single observables. It turns out that the BDT method gains a significant amount of separation power in comparison with the individual observables visible in the Merit factor and the background rejection at 50 % signal efficiency in table 4.1. These values can be again improved by taking only the energies above 2×10^{17} eV into account, which

is the threshold of the low energy enhancements of the Pierre Auger Observatory to measure the air showers sufficiently. This improves the background rejection at 50 % signal efficiency to 99.97 %.
In a last step the estimated integrated photon flux limits were calculated with 95 % confidence level under the assumption that no candidate events were measured which would yield the strongest limits. The results are around 0.1 - 0.2 particles per km^2, yr and sr which is similar to the results of the search for photons above 10^{18} eV, also published by the Pierre Auger collaboration. Existing flux limits published by KASCADE-Grande may be improved by up to two orders of magnitude.

4.2 Outlook

While the first test of the analysis strategy provided promising results, it has to be tested in subsequent steps with a much larger set of simulated air showers to reduce statistical uncertainties. Also systematic studies have to be made. Instead of EPOS-LHC as the hadronic interaction model also SIBYLL 2.3c and QGSJET-II-04 should be used to train the MVA. Additionally the composition of the trainings sample should be varied. In contrast to the pure proton approach of this analysis also iron nuclei could be taken into account.
The variation of the energy and of the observables X_{max} and S_4 as well as the exposure should be derived. These are linked to systematic uncertainties of the detector and are necessary to quantify the uncertainty of the results.
In the final step the analysis will be applied to data measured by the low energy enhancements of the Pierre Auger Observatory. To not just use the whole data set with the risk of something going wrong and making the whole data set unusable for this analysis, first a smaller sample of 5 % of the data will be analysed. If this check is done and everything is working properly, the analysis will be applied to the rest of the data.

A Appendix

An input file for CORSIKA simulations used in this thesis is given. The example is for a photon induced air shower with an energy between $10^{17.5}$ and 10^{18} eV.

```
# Config file for generate_clusterjobs_corsika

Path = /data/auger6/LowEnergyPhotonSearch/AirShowerSimulations

Model = EPOS-LHC

Particle = Photon

EnergyLimitLowNumber = 1
EnergyLimitUpNumber = 1

EnergyLimitLowExponential = 17.5
EnergyLimitUpExponential = 18.0

ZenithLimitLow = 0.0
ZenithLimitUp = 65.0

StartJob = 1
EndJob = 2000

Queue = xl
TimeLimit = 1-00:00:00
Constraint = computeserver
MemLimit = 4000
```

A bootstrap file of an Offline simulation. This file controls the simulation process.

```
<?xml version="1.0" encoding="iso-8859-1"?>

<!DOCTYPE bootstrap [
  <!ENTITY standardSdRealDetConfig SYSTEM '/products/auger/
     OfflineSoftwareFramework/v3r3p4_sqlite/gnu-4.9/share/auger-
     offline/config/standardSdRealDetConfig.xml'>
  <!ENTITY standardSdSimModuleConfig SYSTEM '/products/auger/
     OfflineSoftwareFramework/v3r3p4_sqlite/gnu-4.9/share/auger-
     offline/config/standardSdSimModuleConfig.xml'>
  <!ENTITY standardFdRealDetConfig SYSTEM '/products/auger/
     OfflineSoftwareFramework/v3r3p4_sqlite/gnu-4.9/share/auger-
     offline/config/standardFdRealDetConfig.xml'>
  <!ENTITY standardFdSimModuleConfig SYSTEM '/products/auger/
     OfflineSoftwareFramework/v3r3p4_sqlite/gnu-4.9/share/auger-
     offline/config/standardFdSimModuleConfig.xml'>
  <!ENTITY standardSdRecModuleConfig SYSTEM '/products/auger/
     OfflineSoftwareFramework/v3r3p4_sqlite/gnu-4.9/share/auger-
     offline/config/standardSdRecModuleConfig.xml'>
```

```
  <!ENTITY standardFdRecModuleConfig SYSTEM '/products/auger/
     OfflineSoftwareFramework/v3r3p4_sqlite/gnu-4.9/share/auger-
     offline/config/standardFdRecModuleConfig.xml'>
  <!ENTITY standardHdRecModuleConfig SYSTEM '/products/auger/
     OfflineSoftwareFramework/v3r3p4_sqlite/gnu-4.9/share/auger-
     offline/config/standardHdRecModuleConfig.xml'>
] >

<bootstrap xmlns:xsi="http://www.w3.org/2001/XMLSchema-instance"
           xsi:noNamespaceSchemaLocation='/products/auger/
              OfflineSoftwareFramework/v3r3p4_sqlite/gnu-4.9/share/
              auger-offline/config/bootstrap.xsd'
           xmlns:xlink="http://www.auger.org/schema/types">

  &standardSdRealDetConfig;
  &standardSdSimModuleConfig;
  &standardFdRealDetConfig;
  &standardFdSimModuleConfig;
  &standardSdRecModuleConfig;
  &standardFdRecModuleConfig;
  &standardHdRecModuleConfig;

  <centralConfig>

    <configLink
      id          = "ModuleSequence"
      type        = "XML"
      xlink:href  = "./ModuleSequence.xml"/>

    <configLink
      id          = "EventFileReader"
      type        = "XML"
      xlink:href  = "./EventFileReader.xml"/>

    <configLink
      id          = "EventGenerator"
      type        = "XML"
      xlink:href  = "./EventGenerator.xml"/>

    <configLink
      id          = "LDFFinder"
      type        = "XML"
      xlink:href  = "/products/auger/OfflineSoftwareFramework/
         v3r3p4_sqlite/gnu-4.9/share/auger-offline/config/
         LDFFinderKG_Infill.xml"/>

    <configLink
      id          = "SdEventSelector"
      type        = "XML"
      xlink:href  = "/products/auger/OfflineSoftwareFramework/
         v3r3p4_sqlite/gnu-4.9/share/auger-offline/config/
         SdEventSelector_Infill.xml"/>

    <configLink
      id          = "RecDataWriter"
      type        = "XML"
      xlink:href  = "./RecDataWriterNG.xml"/>

    <configLink
       id          = "FManagerRegister"
       type        = "XML"
       xlink:href  = "FManagerRegisterConfig.xml" />

    <configLink
       id          = "FdUpTimeFileManager"
       type        = "XML"
       xlink:href  = "FdUpTimeFileManagerConfig.xml" />
```

```
  <configLink
     id          = "SManagerRegister"
     type        = "XML"
      xlink:href = "SManagerRegisterConfig.xml" />

  <configLink
     id          = "T2LifeROOTFileManager"
     type        = "XML"
     xlink:href = "T2LifeROOTFileManagerConfig.xml" />

</centralConfig>

<parameterOverrides>

  <configLink id="EventFileReader">
    <EventFileReader>
      <InputFilenames>
        PATHTOCORSIKAFILE
      </InputFilenames>
    </EventFileReader>
  </configLink>

  <configLink id="RecDataWriter">
    <RecDataWriter>
      <rootOutput>
        <outputFileName> PATHTOADSTFILE </outputFileName>
      </rootOutput>
    </RecDataWriter>
  </configLink>

 <configLink id="AAerosolSQLManager">
     <detectorDatabaseConfig>
         <databaseName> /nfs/moroni_8/data/auger/SQLite/
            Atm_Aerosol_1_A.sqlite </databaseName>
     </detectorDatabaseConfig>
  </configLink>

  <configLink id="ACloudSQLManager">
     <detectorDatabaseConfig>
         <databaseName> /nfs/moroni_8/data/auger/SQLite/
            Atm_Cloud_1_A.sqlite </databaseName>
     </detectorDatabaseConfig>
  </configLink>

  <configLink id="AGOESSQLManager">
     <detectorDatabaseConfig>
         <databaseName> /nfs/moroni_8/data/auger/SQLite/
            Atm_GOES_0_A.sqlite </databaseName>
     </detectorDatabaseConfig>
  </configLink>

  <configLink id="ALidarSQLManager">
     <detectorDatabaseConfig>
         <databaseName> /nfs/moroni_8/data/auger/SQLite/
            Atm_Lidar_1_A.sqlite </databaseName>
     </detectorDatabaseConfig>
  </configLink>

  <configLink id="AMolecularSQLManager">
     <detectorDatabaseConfig>
         <databaseName> /nfs/moroni_8/data/auger/SQLite/
            Atm_Molecular_1_A.sqlite </databaseName>
     </detectorDatabaseConfig>
  </configLink>

  <configLink id="AOverallQualitySQLManager">
```

```
      <detectorDatabaseConfig>
          <databaseName> /nfs/moroni_8/data/auger/SQLite/
             Atm_Quality_0_A.sqlite </databaseName>
      </detectorDatabaseConfig>
    </configLink>

    <configLink id="FCalibSQLManager">
      <detectorDatabaseConfig>
          <databaseName> /nfs/moroni_8/data/auger/SQLite/
             FD_Calib_1_A.sqlite </databaseName>
      </detectorDatabaseConfig>
    </configLink>

    <configLink id="FdBackgroundSimulator">
      <FdBackgroundSimulator>
        <bgMode> bgLoop </bgMode>
      </FdBackgroundSimulator>
    </configLink>

    <configLink id="FdElectronicsSimulator">
      <FdElectronicsSimulator>
        <useMonitoringInfo> 1 </useMonitoringInfo>
      </FdElectronicsSimulator>
    </configLink>

    <configLink id="FdProfileReconstructor">
      <FdProfileReconstructorKG>
      <profileCalculation>
        <multipleScatteringLDF> eNone </multipleScatteringLDF>
        <opticalHalo> eNone </opticalHalo>
      </profileCalculation>
      </FdProfileReconstructorKG>
    </configLink>

    <configLink id="FdCalibrator">
      <FdCalibrator>
        <calibrationCorrection>
      1 1 1 1 1
          </calibrationCorrection>
      </FdCalibrator>
    </configLink>

  </parameterOverrides>

</bootstrap>
```

A modul sequence file of an Offline simulation. In this file the sequence of modules is specified which are used in the run time.

```
<!-- A sequence for golden hybrid simulation and reconstruction -->

<sequenceFile xmlns:xsi="http://www.w3.org/2001/XMLSchema-instance"
              xsi:noNamespaceSchemaLocation='/products/auger/
                 OfflineSoftwareFramework/v3r3p4_sqlite/gnu-4.9/
                 share/auger-offline/config/ModuleSequence.xsd'>

  <enableTiming/>

  <moduleControl>

    <loop numTimes="1" pushEventToStack="yes">

      <module> EventFileReaderOG </module>
      <module> MCShowerCheckerOG </module>

      <loop numTimes="1" pushEventToStack="yes">

        <module> EventGeneratorOG </module>

        <!-- SD simulation part -->
        <loop numTimes="unbounded" pushEventToStack="no">
          <module> CachedShowerRegeneratorOG </module>
          <module> G4TankSimulatorOG </module>
        </loop>

        <try>  <!-- catch triggerless events for RecData* -->

          <module> SdSimulationCalibrationFillerOG </module>
          <module> SdPMTSimulatorOG </module>
          <module> SdFilterFADCSimulatorMTU </module>
          <module> SdBaselineSimulatorOG </module>
          <module> TankTriggerSimulatorOG </module>
          <module> TankGPSSimulatorOG </module>

          <!-- FD simulation part -->
          <module> FdSimEventCheckerOG </module>
          <module> ShowerLightSimulatorKG </module>
          <module> LightAtDiaphragmSimulatorKG </module>
          <module> ShowerPhotonGeneratorOG </module>
          <module> TelescopeSimulatorKG </module>
          <module> FdBackgroundSimulatorOG </module>
          <module> FdElectronicsSimulatorOG </module>
          <module> FdTriggerSimulatorOG </module>

          <!-- Trigger and Event builder -->
          <module> CentralTriggerSimulatorXb </module>
          <module> CentralTriggerEventBuilderOG </module>
          <module> EventBuilderOG </module>

          <!-- Reconstruction -->
          <module> EventCheckerOG </module>

          <try> <!-- run RecData*, even if checker, calibrator send
              Continue -->

            <module> SdCalibratorOG </module>

            <!-- Hybrid reconstruction -->
            <try>  <!-- limit how far a Continue goes -->
              <module> FdCalibratorOG </module>
              <module> FdEyeMergerKG </module>
              <module> FdPulseFinderOG </module>
              <module> FdSDPFinderOG </module>
```

```
            <module> FdAxisFinderOG </module>
            <module> HybridGeometryFinderOG </module>
            <module> HybridGeometryFinderWG </module>
            <module> FdApertureLightKG </module>
            <module> FdEnergyDepositFinderKG </module>
          </try>

          <!-- SD reconstruction -->
          <try>   <!-- limit how far a Continue goes -->
            <module> SdEventSelectorOG </module>
            <module> SdMonteCarloEventSelectorOG </module>
            <module> SdPlaneFitOG </module>
            <module> LDFFinderKG </module>
            <module> Risetime1000LLL </module>
            <module> SdEventPosteriorSelectorOG </module>
          </try>

        </try> <!-- catch calibrator Continues -->
      </try> <!-- catch trigger Continues -->

      <!-- export the ADST -->
      <module> RecDataWriterNG </module>

    </loop>
  </loop>

 </moduleControl>

</sequenceFile>
```

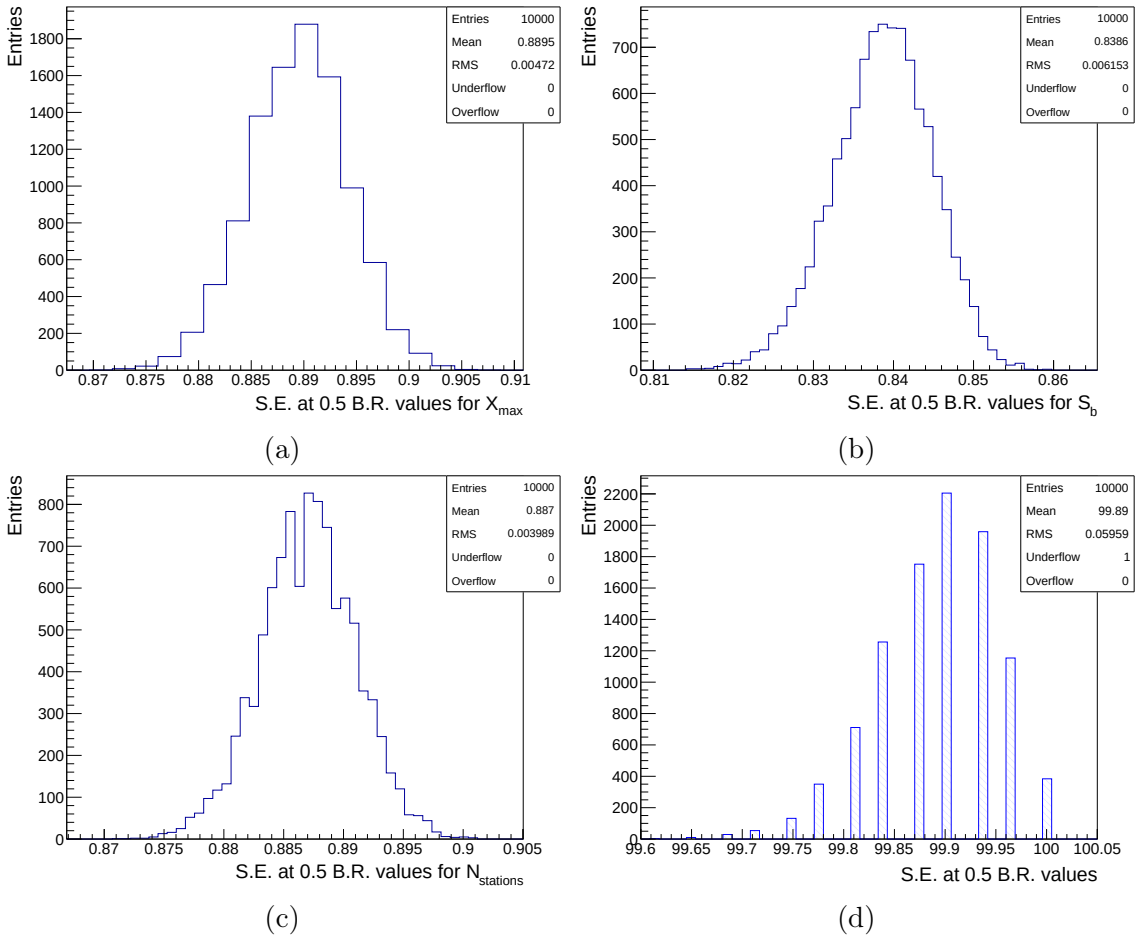

Figure A.1: Result of the bootstrapping method for the value for the background rejection vs. signal efficiency of the (a) X_{max} values, (b) S_4 values, (c) N_{stations} values and the (d) BDT values for the energy range from $10^{16.5}$ to $10^{19.5}$ eV, trained with an independent sample of the same energy range. The method has been applied 10000 times.

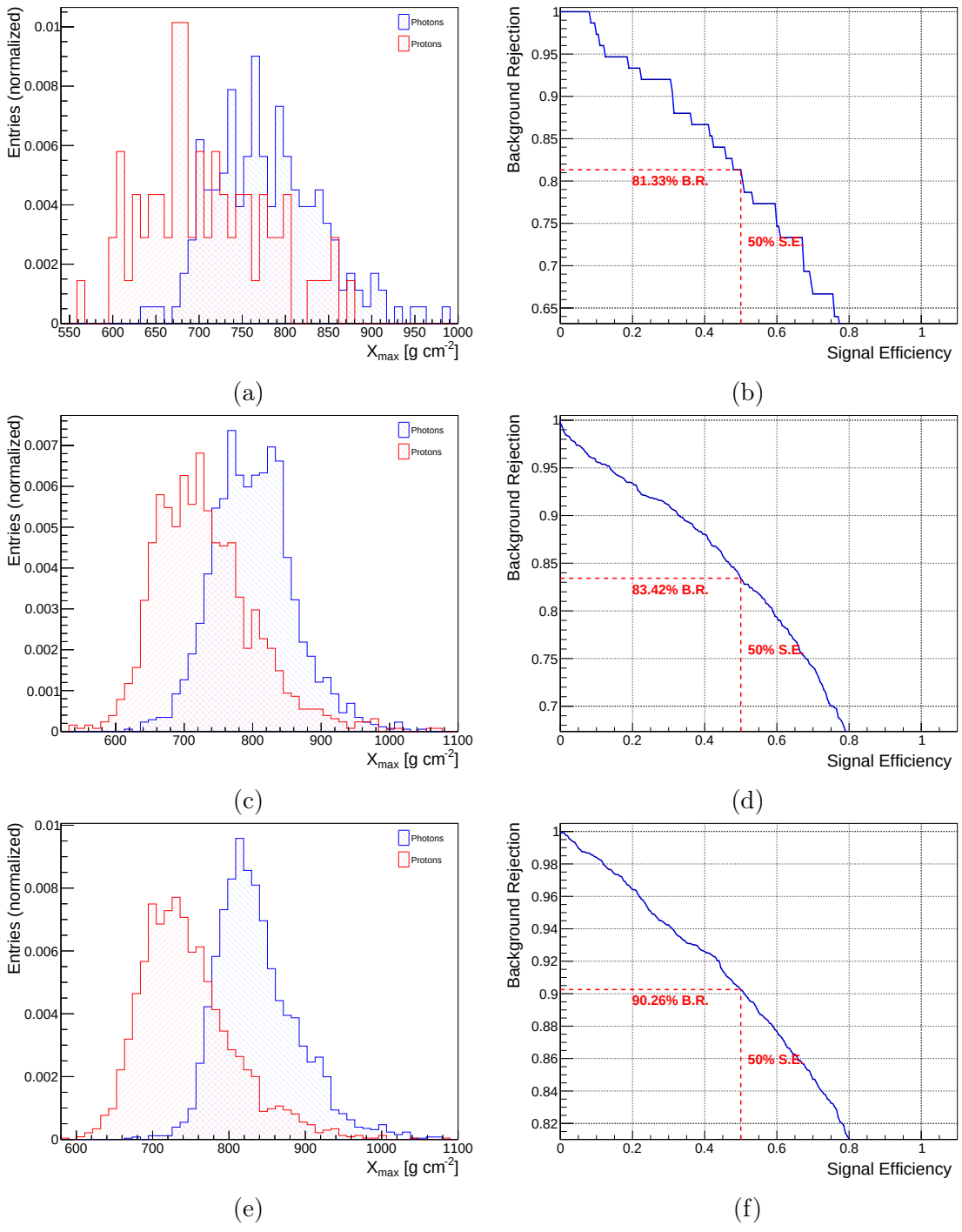

Figure A.2: Distributions of the observable $X_{\max}$ and the corresponding plot for the signal efficiency for simulated air showers and detector response with energies of the primary particle between (a)(b) $10^{16.5}\,\mathrm{eV} < E < 10^{17}\,\mathrm{eV}$, (c)(d) $10^{17}\,\mathrm{eV} < E < 10^{17.5}\,\mathrm{eV}$,(e)(f) $10^{17.5}\,\mathrm{eV} < E < 10^{18}\,\mathrm{eV}$.

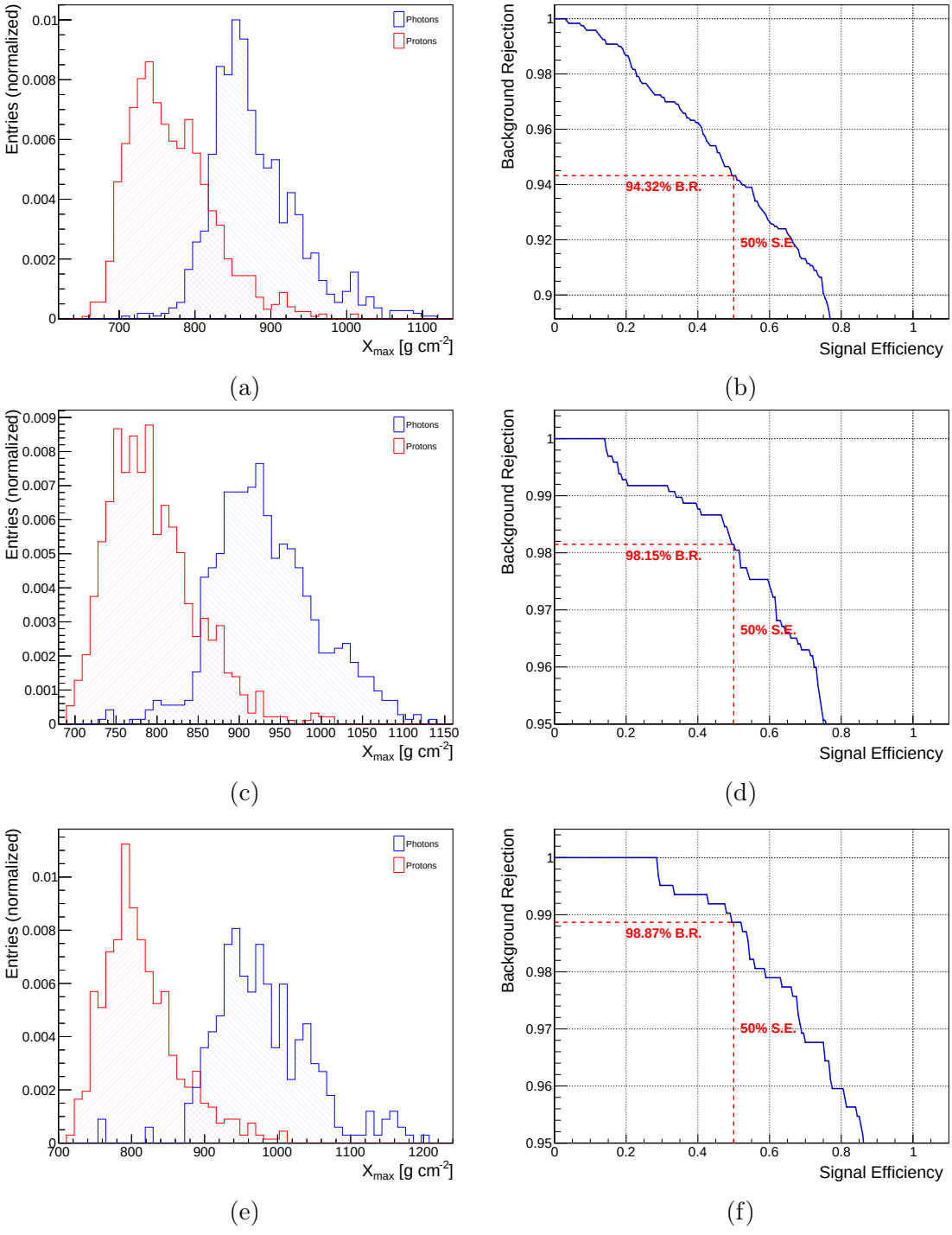

Figure A.3: Distributions of the observable $X_{\max}$ and the corresponding plot for the signal efficiency for simulated air showers and detector response with energies of the primary particle between (a)(b) $10^{18}\,\mathrm{eV} < E < 10^{18.5}\,\mathrm{eV}$, (c)(d) $10^{18.5}\,\mathrm{eV} < E < 10^{19}\,\mathrm{eV}$, (e)(f) $10^{19}\,\mathrm{eV} < E < 10^{19.5}\,\mathrm{eV}$.

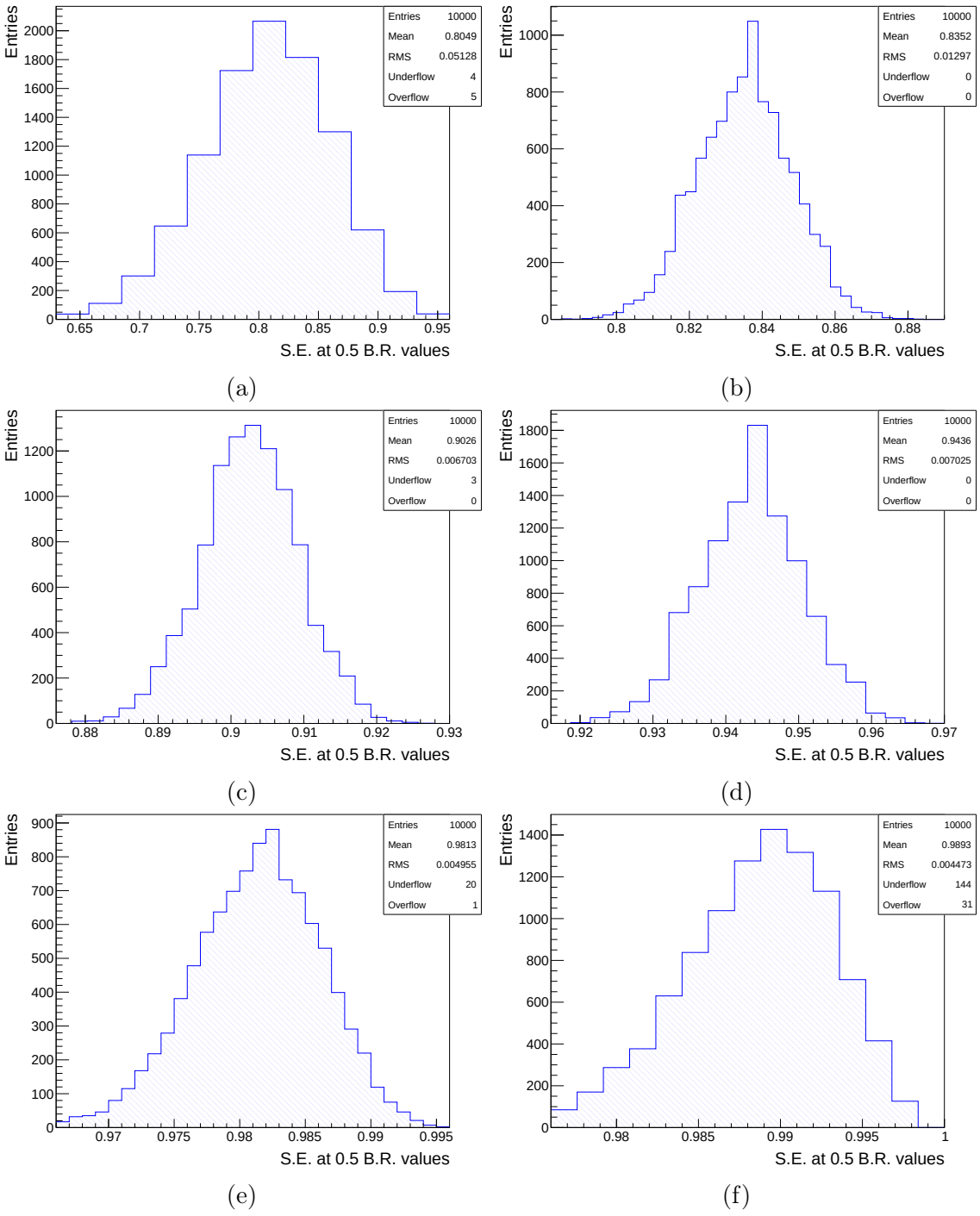

Figure A.4: Bootstrap distributions of the signal efficiency vs. background rejecdtion of the observable $X_{\max}$ with energies of the primary particle between (a) $10^{16.5}\,\mathrm{eV} < E < 10^{17}\,\mathrm{eV}$,(b) $10^{17}\,\mathrm{eV} < E < 10^{17.5}\,\mathrm{eV}$,(c) $10^{17.5}\,\mathrm{eV} < E < 10^{18}\,\mathrm{eV}$, (d) $10^{18}\,\mathrm{eV} < E < 10^{18.5}\,\mathrm{eV}$,(e) $10^{18.5}\,\mathrm{eV} < E < 10^{19}\,\mathrm{eV}$,(f) $10^{19}\,\mathrm{eV} < E < 10^{19.5}\,\mathrm{eV}$. The method has been applied 10000 times.

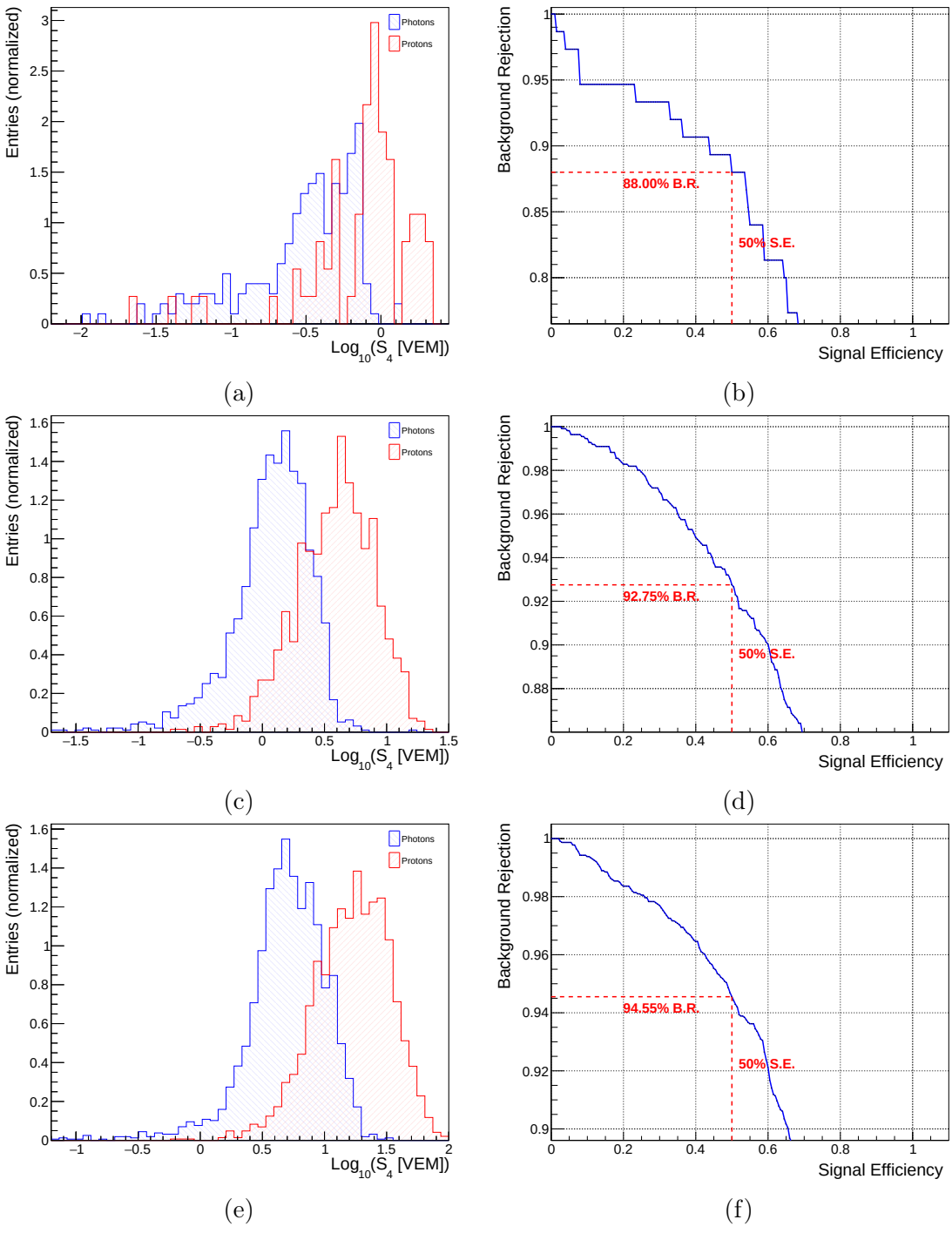

Figure A.5: Distributions of the observable S_4 and the corresponding plot for the signal efficiency for simulated air showers and detector response with energies of the primary particle between (a)(b) $10^{16.5}\,\mathrm{eV} < E < 10^{17}\,\mathrm{eV}$, (c)(d) $10^{17}\,\mathrm{eV} < E < 10^{17.5}\,\mathrm{eV}$,(e)(f) $10^{17.5}\,\mathrm{eV} < E < 10^{18}\,\mathrm{eV}$.

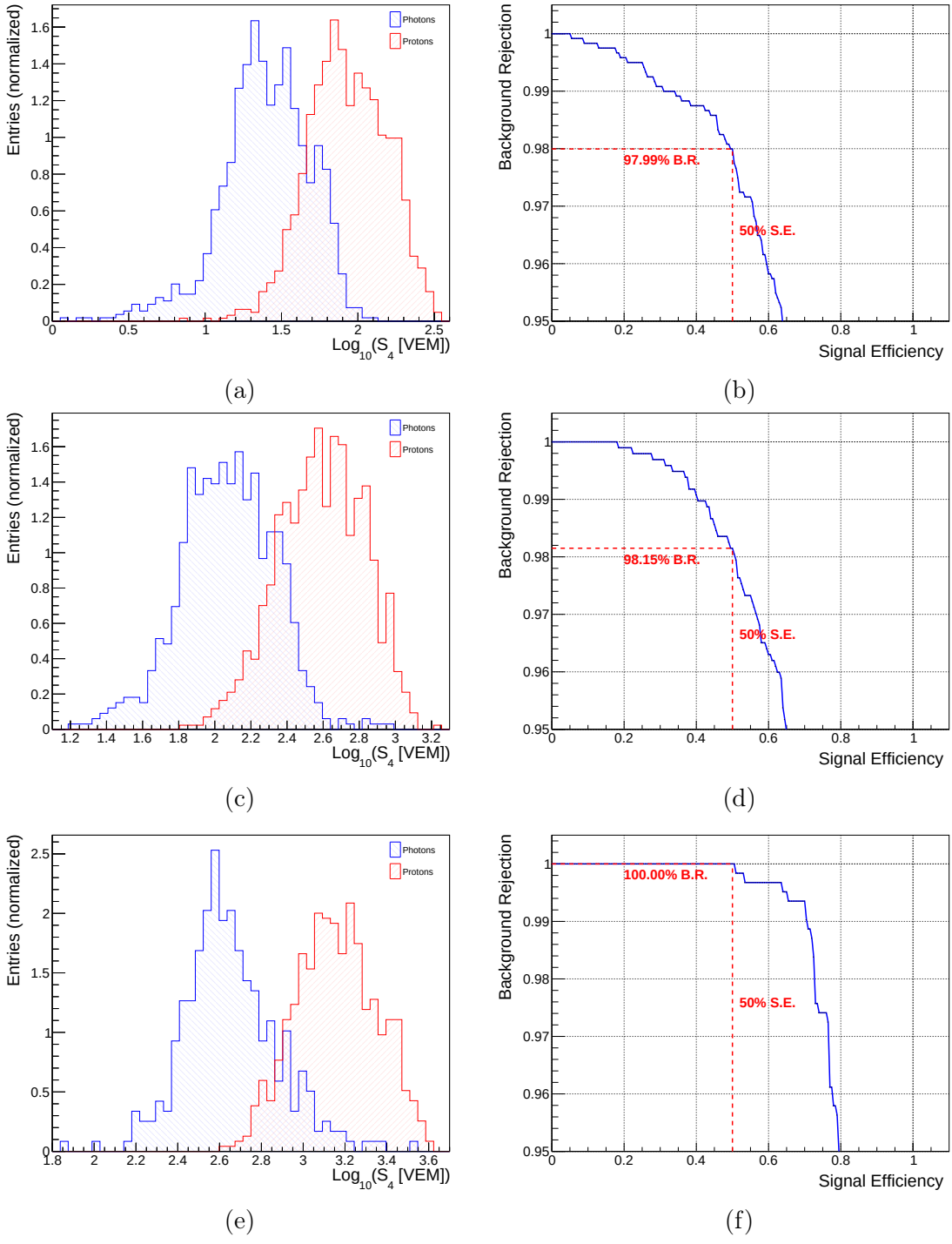

Figure A.6: Distributions of the observable S_4 and the corresponding plot for the signal efficiency for simulated air showers and detector response with energies of the primary particle between (a)(b) $10^{18}\,\mathrm{eV} < E < 10^{18.5}\,\mathrm{eV}$, (c)(d) $10^{18.5}\,\mathrm{eV} < E < 10^{19}\,\mathrm{eV}$, (e)(f) $10^{19}\,\mathrm{eV} < E < 10^{19.5}\,\mathrm{eV}$.

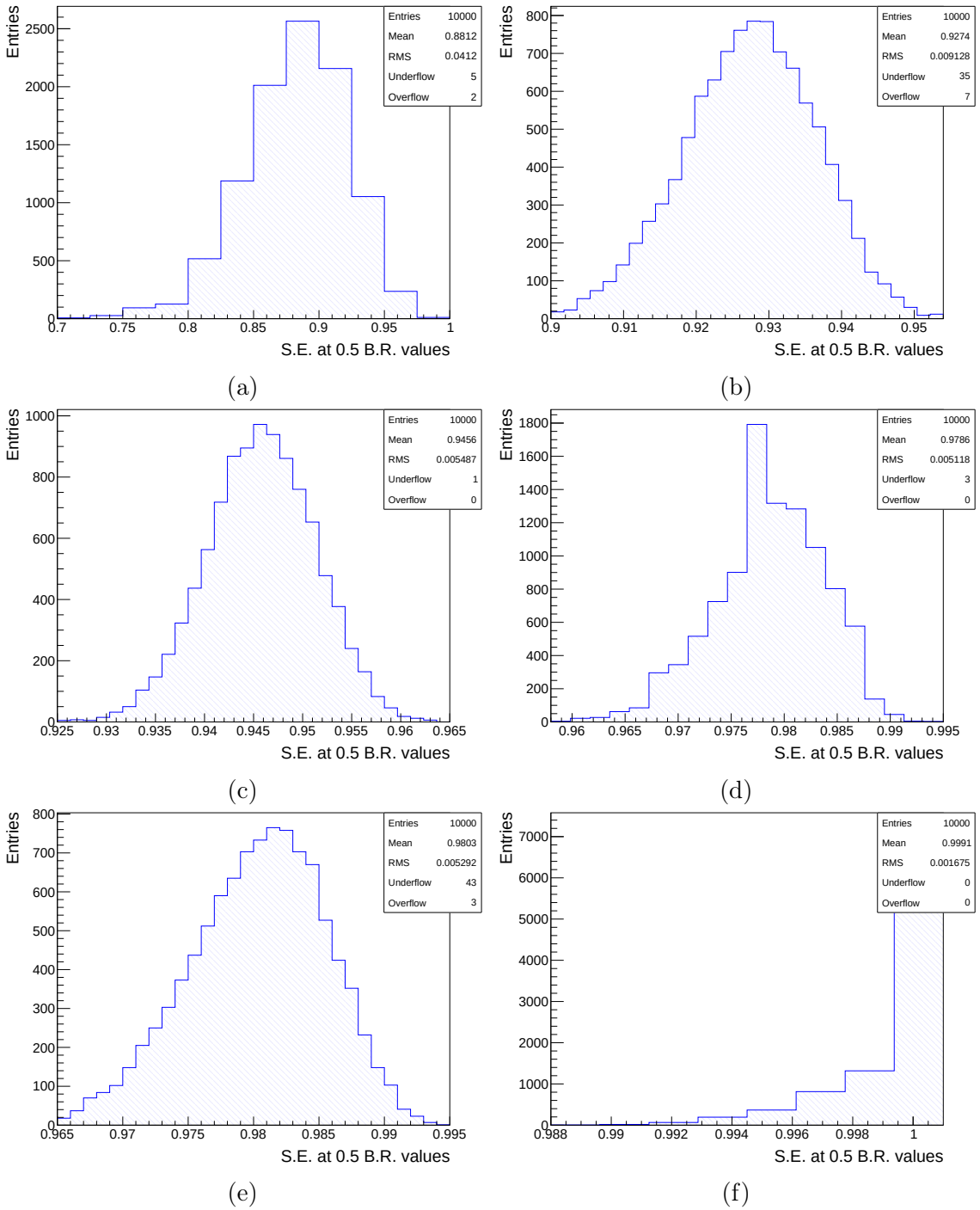

Figure A.7: Bootstrap distributions of the signal efficiency vs. background rejecdtion of the observable S_4 with energies of the primary particle between (a) $10^{16.5}\,\mathrm{eV} < E < 10^{17}\,\mathrm{eV}$,(b) $10^{17}\,\mathrm{eV} < E < 10^{17.5}\,\mathrm{eV}$,(c) $10^{17.5}\,\mathrm{eV} < E < 10^{18}\,\mathrm{eV}$, (d) $10^{18}\,\mathrm{eV} < E < 10^{18.5}\,\mathrm{eV}$,(e) $10^{18.5}\,\mathrm{eV} < E < 10^{19}\,\mathrm{eV}$,(f) $10^{19}\,\mathrm{eV} < E < 10^{19.5}\,\mathrm{eV}$. The method has been applied 10000 times.

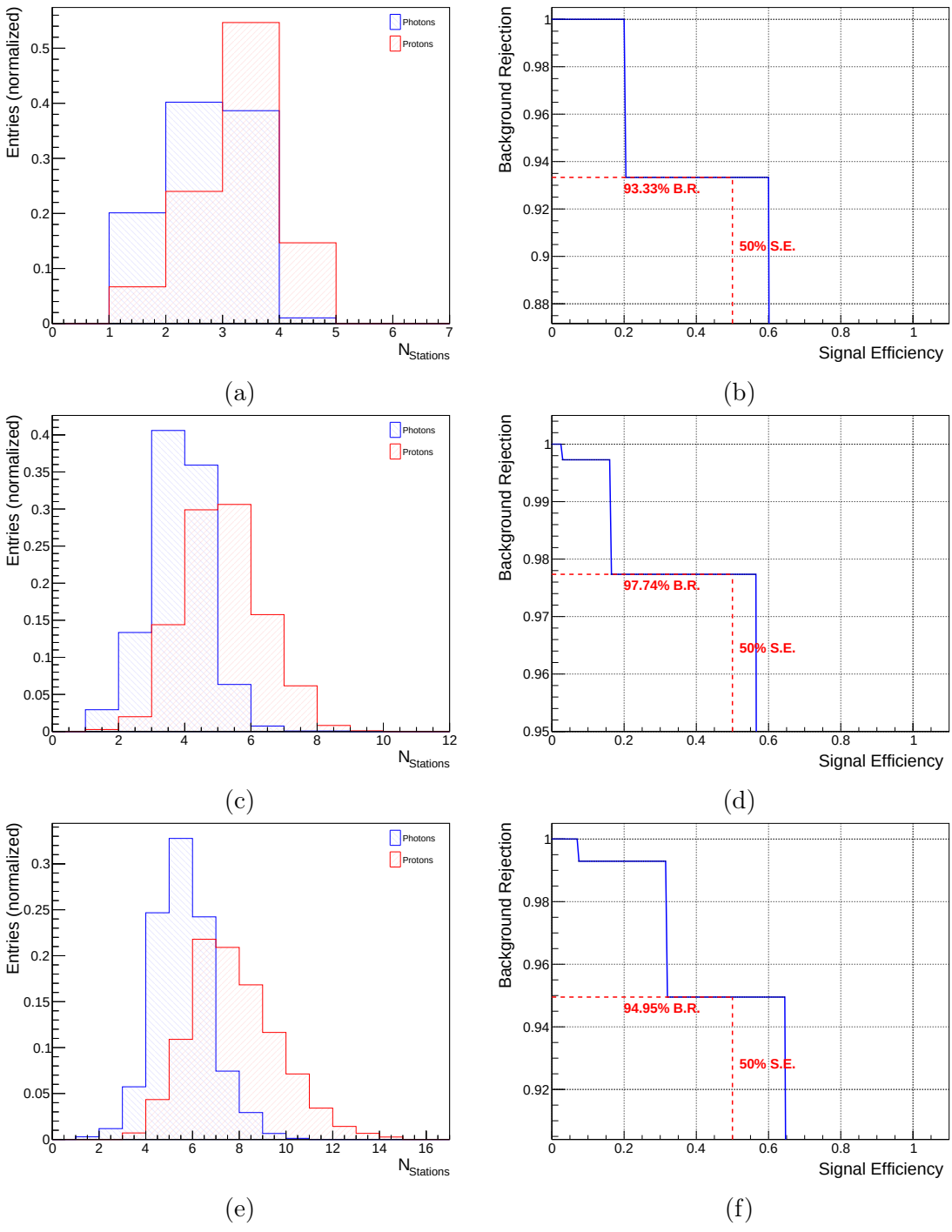

Figure A.8: Distributions of the observable N_{stations} and the corresponding plot for the signal efficiency for simulated air showers and detector response with energies of the primary particle between (a)(b) $10^{16.5}\,\text{eV} < E < 10^{17}\,\text{eV}$, (c)(d) $10^{17}\,\text{eV} < E < 10^{17.5}\,\text{eV}$,(e)(f) $10^{17.5}\,\text{eV} < E < 10^{18}\,\text{eV}$.

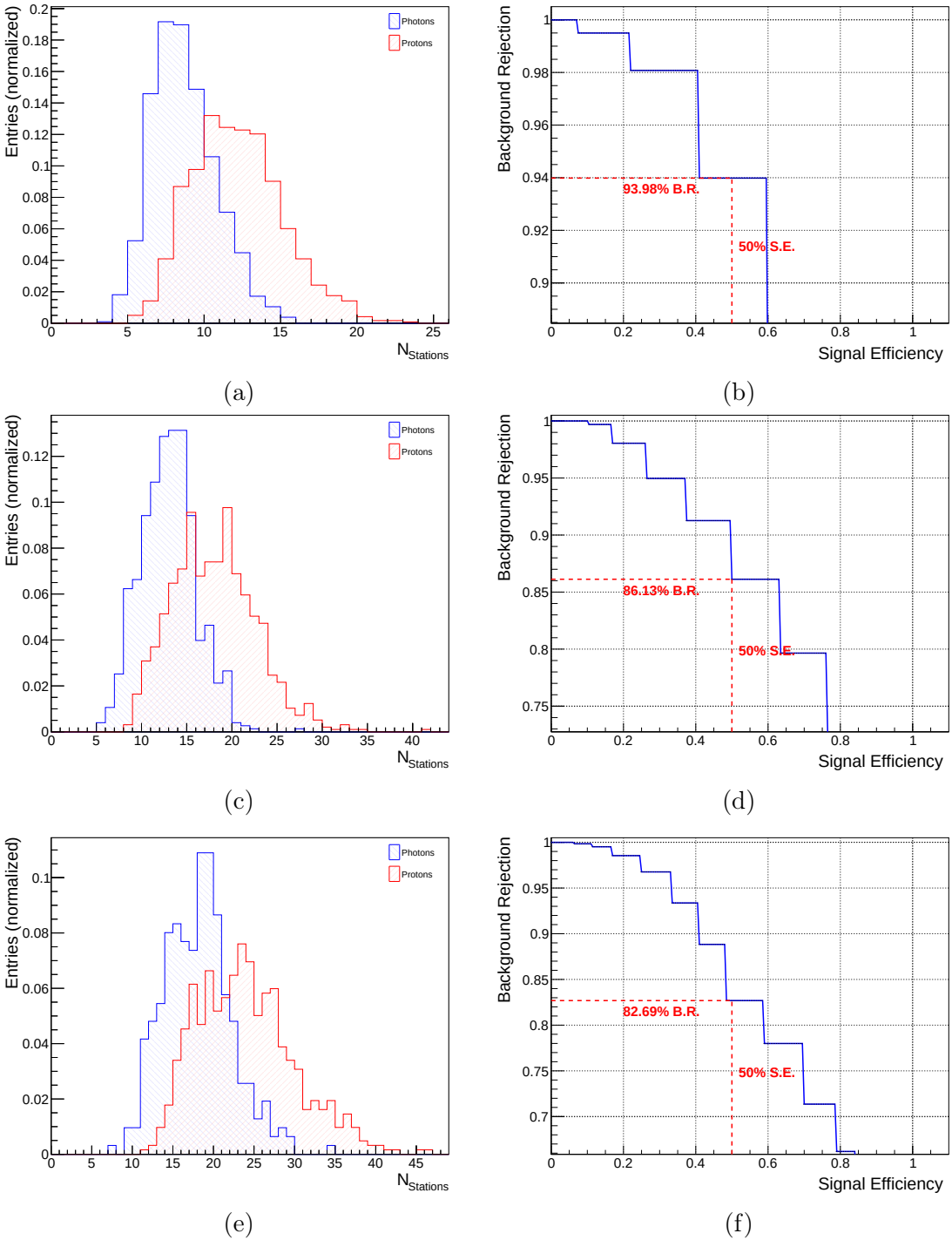

Figure A.9: Distributions of the observable N_{stations} and the corresponding plot for the signal efficiency for simulated air showers and detector response with energies of the primary particle between (a)(b) $10^{18}\,\text{eV} < E < 10^{18.5}\,\text{eV}$, (c)(d) $10^{18.5}\,\text{eV} < E < 10^{19}\,\text{eV}$, (e)(f) $10^{19}\,\text{eV} < E < 10^{19.5}\,\text{eV}$.

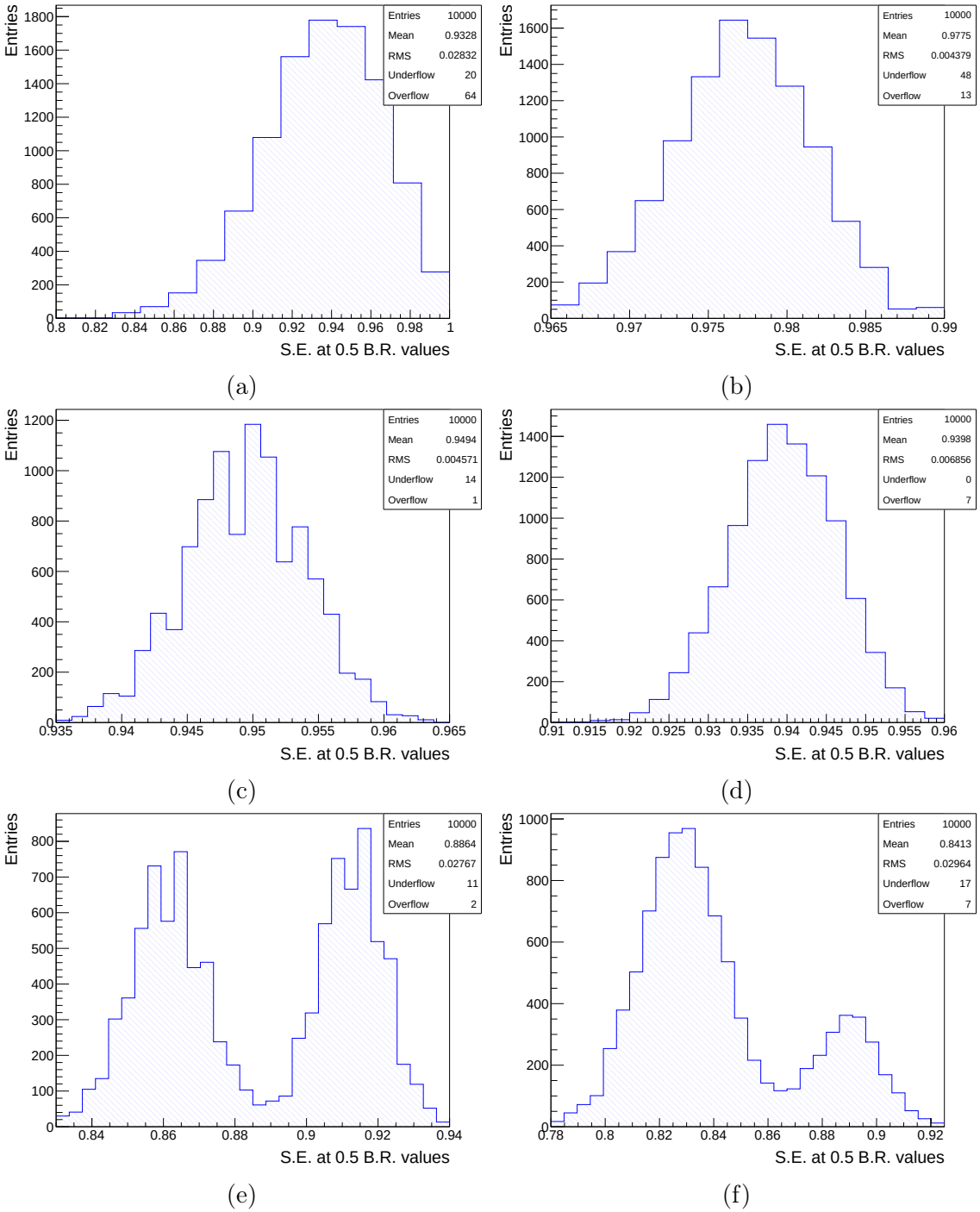

Figure A.10: Bootstrap distributions of the signal efficiency vs. background rejecdtion of the observable N_{stations} with energies of the primary particle between (a) $10^{16.5}\,\text{eV} < E < 10^{17}\,\text{eV}$,(b) $10^{17}\,\text{eV} < E < 10^{17.5}\,\text{eV}$,(c) $10^{17.5}\,\text{eV} < E < 10^{18}\,\text{eV}$, (d) $10^{18}\,\text{eV} < E < 10^{18.5}\,\text{eV}$,(e) $10^{18.5}\,\text{eV} < E < 10^{19}\,\text{eV}$,(f) $10^{19}\,\text{eV} < E < 10^{19.5}\,\text{eV}$. The method has been applied 10000 times.

Energy bin [$\log_{10}(E[\text{eV}])$]	Photons	Protons
16.5-17.0	778.42	708.21
17.0-17.5	801.37	730.21
17.5-18.0	837.92	746.26
18.0-18.5	879.12	769.54
18.5-19.0	933.94	793.98
19.0-19.5	979.79	813.84

Table A.1: Mean values of the X_{max} distributions in Fig. A.2 and Fig. A.3 divided in energy bins for air shower simulations made with CORSIKA.

Energy bin [$\log_{10}(E[\text{eV}])$]	Photons	Protons
16.5-17.0	-0.532433	-0.142632
17.0-17.5	0.0684638	0.581687
17.5-18.0	0.694376	1.22121
18.0-18.5	1.39497	1.92856
18.5-19.0	2.06923	2.58685
19.0-19.5	2.65313	3.15742

Table A.2: Mean values of the S_4 distributions in Fig. A.5 and Fig. A.6 divided in energy bins for air shower simulations made with CORSIKA.

Energy bin [$\log_{10}(E[\text{eV}])$]	Photons	Protons
16.5-17.0	2.20619	2.77333
17.0-17.5	3.32176	4.65127
17.5-18.0	5.10285	7.28654
18.0-18.5	8.20877	11.6909
18.5-19.0	12.5066	17.52
19.0-19.5	17.5994	23.5275

Table A.3: Mean values of the N_{stations} distributions in Fig. A.8 and Fig. A.9 divided in energy bins for air shower simulations made with CORSIKA.

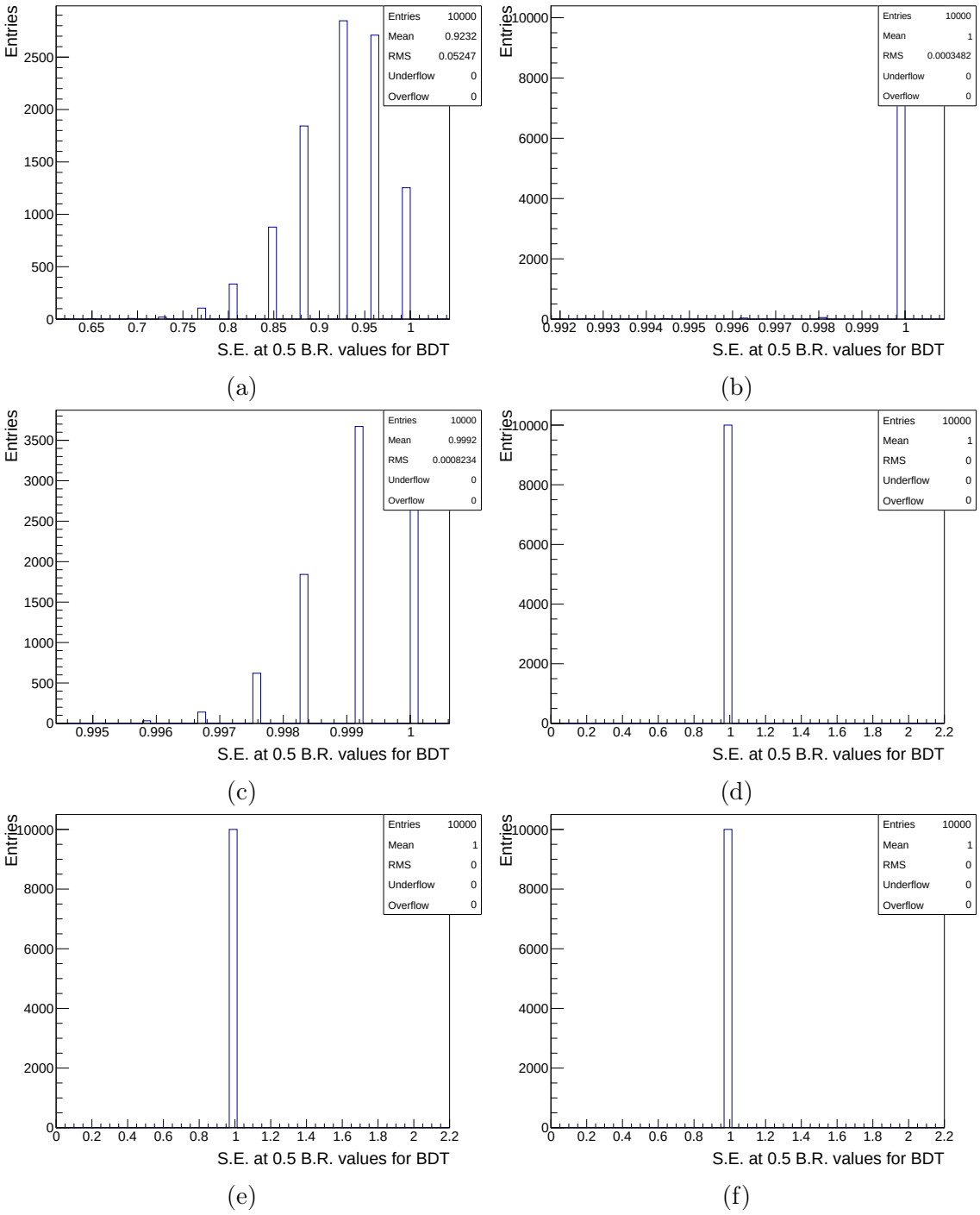

Figure A.11: Bootstrap distributions of the signal efficiency vs. background rejecdtion of the BDT values with energies of the primary particle between (a) $10^{16.5}\,\mathrm{eV} < E < 10^{17}\,\mathrm{eV}$,(b) $10^{17}\,\mathrm{eV} < E < 10^{17.5}\,\mathrm{eV}$,(c) $10^{17.5}\,\mathrm{eV} < E < 10^{18}\,\mathrm{eV}$, (d) $10^{18.0}\,\mathrm{eV} < E < 10^{18.5}\,\mathrm{eV}$,(e) $10^{18.5}\,\mathrm{eV} < E < 10^{19}\,\mathrm{eV}$,(f) $10^{19}\,\mathrm{eV} < E < 10^{19.5}\,\mathrm{eV}$. The BDT was traines with an independet sample of the whole energy range. The method has been applied 10000 times.

B Bibliography

[1] Y. Sekido and H. Elliot, "Early history of cosmic ray studies". D. Reidel Publishing Company, 1985.

[2] T. Wulf, "Über den Ursprung der in der Atmosphäre vorhandenen gamma-Strahlung," vol. 10, pp. 997–1003, 1909.

[3] D. Pacini, "La radiation pénétrante sur la mer," Le Radium (Paris), vol. 8, no. 8, pp. 307–312, 1911.

[4] V. F. Hess, "Über Beobachtungen der durchdringenden Strahlung bei sieben Freiballon- fahrten," Physikalische Zeitschrift, vol. 13, pp. 1084–1091, 1912.

[5] The Nobel Foundation, "Nobel Lectures, Physics 1922-1941". Elsevier Publishing Company, 1965.

[6] W. Kolhörster, "Messungen der durchdringenden Strahlung bis in Höhen von 9300 m," Verhandlungen der Deutschen Physikalischen Gesellschaft, vol. 16, pp. 719–721, 1914.

[7] J. Kraus, "A strange radiation from above," Cosmic Search: Issue 5, vol. 2, 1980.

[8] H. J. Bhabha and W. Heitler, "The Passage of Fast Electrons and the Theory of Cosmic Showers," in Proceedings of the Royal Society of London, vol. 159, pp. 432–458, 1937.

[9] P. Auger, R. Maze, P. Ehrenfest Jr., and A. Freon, "Les grandes gerbes de rayons cosmiques," Journal de Physique et Le Radium, vol. 10, pp. 39–48, 1939.

[10] C. D. Anderson, "The positive electron," The Physical Review, vol. 43, pp. 491–494, 1933.

[11] S. H. Neddermeyer and C. D. Anderson, "Note on the nature of cosmic-ray particles," The Physical Review, vol. 51, pp. 884–886, 1937.

[12] G. D. Rochester and C. C. Butler, "Evidence for the existence of new unstable elementary particles," Nature, vol. 160, pp. 855–857, 1947.

[13] K. Abe et al., "The results from BESS-Polar experiment," Advances in Space Research, vol. 60, no. 4, pp. 806–814, 2017.

[14] A. Galper et al., "The PAMELA experiment: a decade of Cosmic Ray Physics in space," Journal of Physics: Conference Series, vol. 798, no. 1, p. 012033, 2017.

[15] J. Casaus, "The AMS-02 experiment on the ISS," Journal of Physics: Conference Series, vol. 171, no. 1, p. 012045, 2009.

[16] W. Hofmann, "Largest ever Cherenkov telescope sees first light," Press Release, 2012.

[17] D. Perkins, "Particle Astrophysics, Second Edition". Oxford Master Series in Physics, OUP Oxford, 2008.

[18] R. D. Blandford and J. P. Ostriker, "Particle acceleration by astrophysical shocks," vol. 221, pp. L29–L32, Apr. 1978.

[19] D. Kazanas and A. Nicolaidis, "Cosmic ray 'knee': A Herald of new physics?," Proceedings of the 27th International Cosmic Ray Conference (ICRC 2001) Hamburg, Germany, August 7-15, 2001, pp. 1760–1763, 2001.

[20] C. Patrignani et al., "Review of Particle Physics," Chin. Phys., vol. C40, no. 10, p. 100001, 2016.

[21] A. Haungs, "Cosmic Rays from the Knee to the Ankle," Phys. Procedia, vol. 61, pp. 425–434, 2015.

[22] B. P. Abbott et al., "Observation of Gravitational Waves from a Binary Black Hole Merger," Phys. Rev. Lett., vol. 116, no. 6, 2016.

[23] K. Greisen, "End to the cosmic ray spectrum?," Phys. Rev. Lett., vol. 16, pp. 748–750, 1966.

[24] G. T. Zatsepin and V. A. Kuzmin, "Upper limit of the spectrum of cosmic rays," Journal of Experimental and Theoretical Physics Letters, vol. 4, pp. 78–80, 1966.

[25] M. Kachelriess, E. Parizot, and D. V. Semikoz, "The GZK horizon and constraints on the cosmic ray source spectrum from observations in the GZK regime," Journal of Experimental and Theoretical Physics Letters, vol. 88, pp. 553–557, 2009.

[26] A. Chantelauze, S. Staffi, and L. Bret, “Mysterious high-energy cosmic rays fire from outside the galaxy,” 2017.

[27] C. Grupen, "Astroparticle Physics". Springer-Verlag Berlin Heidelberg, 2005.

[28] M. Niechciol, “A New Window to the Universe? : Searching for Ultra-High-Energy Photons at the Pierre Auger Observatory,” 2015. PhD Thesis at the University of Siegen (unpublished).

[29] T. K. Gaisser and A. M. Hillas, “Reliability of the method of constant intensity cuts for reconstructing the average development of vertical showers,” Proceedings of the 15th International Cosmic Ray Conference (ICRC 1977), Plovdiv, Bulgaria, 1977.

[30] K. Greisen, “The extensive air showers,” in : John G. Wilsdon (ed.), Progress in Cosmic Ray Physics, vol. 3, 1956.

[31] K. Kamata and J. Nishimura, “The Lateral and the Angular Structure Functions of Electron Showers,” Progress of Theoretical Physics Supplement, vol. 6, pp. 93–155, 01 1958.

[32] C. Grupen, A. Böhrer, and L. Smolik, "Particle Detectors". Cambridge monographs on particle physics, nuclear physics, and cosmology, Cambridge Univ. Press, 1996.

[33] F. Halzen, “Lectures on neutrino astronomy: Theory and experiment,” in Proceedings, Conference, TASI’98, Boulder, USA, June 1-26, pp. 524–569, 1998.

[34] W. D. Apel et al., “KASCADE-Grande Limits on the Isotropic Diffuse Gamma-Ray Flux between 100 TeV and 1 EeV,” Astrophys. J., vol. 848, no. 1, p. 1, 2017.

[35] Y. A. Fomin, N. N. Kalmykov, I. S. Karpikov, G. V. Kulikov, M. Yu. Kuznetsov, G. I. Rubtsov, V. Sulakov, and S. V. Troitsky, “Constraints on the flux of $\sim (10^{16} - 10^{17.5})$ eV cosmic photons from the EAS-MSU muon data,” vol. 95, 02 2017.

[36] The Pierre Auger Collaboration, “Search for photons with energies above 10^{18} eV using the hybrid detector of the Pierre Auger Observatory,” 2017.

[37] A. Aab et al. on behalf of the Pierre Auger Collaboration, “The Pierre Auger Observatory: Contributions to the 34th International Cosmic Ray Conference (ICRC 2015),” 2015. https://arxiv.org/abs/1509.03732.

[38] G. Rubtsov et al. on behalf of the Telescope Array collaboration, "Telescope Array search for EeV photons and neutrinos (ICRC 2017)," 2017. https://pos.sissa.it/301/551.

[39] B. Sarkar, K.-H. Kampert, and J. Kulbartz, "Ultra-High Energy Photon and Neutrino Fluxes in Realistic Astrophysical Scenarios," Proceedings, 32nd International Cosmic Ray Conference (ICRC 2011): Beijing, China, August 11-18, 2011, vol. 2, p. 198.

[40] G. Gelmini, O. E. Kalashev, and D. V. Semikoz, "GZK photons as ultra high energy cosmic rays," Journal of Experimental and Theoretical Physics Letters, vol. 106, pp. 1061–1082, 2008.

[41] P. Bhattacharjee and G. Sigl, "Origin and propagation of extremely high-energy cosmic rays," Physics Reports, vol. 327, no. 3, pp. 109–247, 2000.

[42] M. Settimo, "Search for ultra-High Energy Photons with the Pierre Auger Observatory," PoS, p. 062, 2013.

[43] A. B. Migdal, "Bremsstrahlung and pair production in condensed media at high-energies," Phys. Rev., vol. 103, pp. 1811–1820, 1956.

[44] S. Klein, "Suppression of Bremsstrahlung and pair production due to environmental factors," Rev. Mod. Phys., vol. 71, pp. 1501–1538, 1999.

[45] T. Erber, "High-Energy Electromagnetic Conversion Processes in Intense Magnetic Fields," Rev. Mod. Phys., vol. 38, pp. 626–659, Oct 1966.

[46] B. McBreen and C. Lambert, "Interactions of high-energy ($E > 5{\times}10^{19}$ eV) photons in the Earth's magnetic field," Physical Review D, vol. 24, no. 9, pp. 2536–2538, 1981.

[47] R. Engel, "Indirect Detection of Cosmic Rays", pp. 593–632. Berlin, Heidelberg: Springer Berlin Heidelberg, 2012.

[48] The Pierre Auger Collaboration, "Pierre Auger Observatory official website," https://www.auger.org.

[49] The Pierre Auger Collaboration, "The Pierre Auger Project Design Report," 1996. https://inspirehep.net/record/416403.

[50] A. Etchegoyen, "AMIGA, Auger Muons and Infill for the Ground Array," Proceedings, 30th International Cosmic Ray Conference (ICRC 2007): Merida, Yucatan, Mexico, July 3-11, 2007, pp. 1191–1194.

[51] H.-J. Mathes for the Pierre Auger Collaboration, "The HEAT Telescopes of the Pierre Auger Observatory - Status and First Data," Proceedings, 32nd International Cosmic Ray Conference (ICRC 2011): Beijing, China, 2011.

[52] D. Veberic, "Maps of the Pierre Auger Observatory," 2013. https://web.ikp.kit.edu/darko/auger/auger-array/.

[53] T. Suomijarvi and Pierre Auger Observatory Collaboration, "Surface Detector Electronics for the Auger Observatory," International Cosmic Ray Conference, vol. 2, p. 756, 2001.

[54] J. Abraham et al., "Trigger and aperture of the surface detector array of the Pierre Auger Observatory," Nuclear Instruments and Methods in Physics Research Section A: Accelerators, Spectrometers, Detectors and Associated Equipment, vol. 613, no. 1, pp. 29–39, 2010.

[55] J. Abraham et al., "Properties and performance of the prototype instrument for the Pierre Auger Observatory," Nucl. Instrum. Meth., vol. A523, pp. 50–95, 2004.

[56] J. Abraham et al., "The Fluorescence Detector of the Pierre Auger Observatory," Nucl. Instrum. Meth., vol. A620, pp. 227–251, 2010.

[57] V. Fedotov and E. Fedotova, "The Chain Reaction of Atmospheric Nitrogen Oxidation, Initiated by an Electric Discharge in Air," Journal of Physical Chemistry and Biophysics, vol. 5, no. 6, pp. 1–7, 2015.

[58] H. S. Friedman, "Method of Computing Correction Plate for Schmidt System for Near Projection, with Special Reference to System for Television Projection," J. Opt. Soc. Am., vol. 37, pp. 480–484, Jun 1947.

[59] B. Fick, M. Malek, J. A J Matthews, R. Meyhandan, M. Mostafa, M. Roberts, P. Sommers, and L. Wiencke, "The Central Laser Facility at the Pierre Auger Observatory," vol. 1, p. P11003, 11 2006.

[60] B. Daniel, "The AMIGA enhancement of the Pierre Auger Observatory," J. Phys. Conf. Ser., vol. 632, no. 1, p. 012088, 2015.

[61] C. Meurer and N. Scharf on behalf of the Pierre Auger Collaboration, "HEAT - a low energy enhancement of the Pierre Auger Observatory," Astrophysics and Space Sciences Transactions, vol. 7, no. 2, pp. 183–186, 2011.

[62] H.-J. Mathes, "The HEAT telescopes of the Pierre Auger Observatory: Status and first data," Proceedings, 32nd International Cosmic Ray Conference (ICRC 2011): Beijing, China, August 11-18, 2011, p. 153.

[63] D. Heck, J. Knapp, J. Capdevielle, G. Schatz, and T. Thouw, "CORSIKA – an Air Shower Simulation Program," 1998. https://www.ikp.kit.edu/corsika/.

[64] K. Werner, "The hadronic interaction model EPOS," Nuclear Physics B - Proceedings Supplements, vol. 175-176, pp. 81–87, 2008. Proceedings of the XIV International Symposium on Very High Energy Cosmic Ray Interactions.

[65] A. Ferrari, P. R. Sala, A. Fasso, and J. Ranft, "FLUKA: a multi-particle transport code," 2005. CERN-2005-10.

[66] D. Heck and T. Pierog, "Extensive Air Shower Simulations with CORSIKA: A User's Guide (Version 7.5600 from August 17, 2016)," p. 165, 2016.

[67] S. Argirò, S. Barroso, J. Gonzalez, L. Nellen, T. Paul, T. Porter, L. P. Jr., M. Roth, R. Ulrich, and D. Veberič, "The offline software framework of the Pierre Auger Observatory," Nuclear Instruments and Methods in Physics Research Section A: Accelerators, Spectrometers, Detectors and Associated Equipment, vol. 580, no. 3, pp. 1485–1496, 2007.

[68] A. Aab et al. on behalf of the Pierre Auger Collaboration, "The Pierre Auger Observatory: Contributions to the 35th International Cosmic Ray Conference (ICRC 2017)," 2017. https://arxiv.org/abs/1708.06592.

[69] G. Ros, A. Supanitsky, G. Medina-Tanco, L. del Peral, J. D'Olivo, and M. R. Frías, "A new composition-sensitive parameter for ultra-high energy cosmic rays," Astroparticle Physics, vol. 35, no. 3, pp. 140–151, 2011.

[70] G. Ros et al., "S_b for photon-hadron discrimination," 2010. internal note GAP-2010-052.

[71] A. Hoecker, P. Speckmayer, J. Stelzer, J. Therhaag, E. von Toerne, and H. Voss, "TMVA: Toolkit for Multivariate Data Analysis," PoS, vol. ACAT, p. 040, 2007.

[72] R. Brun and F. Rademakers, "ROOT — An object oriented data analysis framework," Nuclear Instruments and Methods in Physics Research Section A: Accelerators, Spectrometers, Detectors and Associated Equipment, vol. 389, no. 1, pp. 81–86, 1997. New Computing Techniques in Physics Research V.

[73] A. Hoecker, P. Speckmayer, J. Stelzer, J. Therhaag, E. von Toerne, and H. Voss, "TMVA 4 - Toolkit for Multivariate Data Analysis with ROOT - Users Guide," p. 147, 2013.

Erklärung

Hiermit erkläre ich, dass ich die vorliegende Masterarbeit selbstständig verfasst und keine anderen als die angegebenen Quellen und Hilfsmittel benutzt sowie Zitate und Ergebnisse Anderer kenntlich gemacht habe.

(Ort) (Datum)	(Unterschrift)